

**Study of Branching Fractions and CP-Violating Asymmetries
in B Meson Decays to Rho And Pion Final State
with the BABAR Detector**

Jinwei Wu

Stanford Linear Accelerator Center
Stanford University
Stanford, CA 94309

SLAC-Report-811

Prepared for the Department of Energy
under contract number DE-AC02-76SF00515

Printed in the United States of America. Available from the National Technical Information Service, U.S. Department of Commerce, 5285 Port Royal Road, Springfield, VA 22161.

This document, and the material and data contained therein, was developed under sponsorship of the United States Government. Neither the United States nor the Department of Energy, nor the Leland Stanford Junior University, nor their employees, nor their respective contractors, subcontractors, or their employees, makes an warranty, express or implied, or assumes any liability of responsibility for accuracy, completeness or usefulness of any information, apparatus, product or process disclosed, or represents that its use will not infringe privately owned rights. Mention of any product, its manufacturer, or suppliers shall not, nor is it intended to, imply approval, disapproval, or fitness of any particular use. A royalty-free, nonexclusive right to use and disseminate same of whatsoever, is expressly reserved to the United States and the University.

STUDY OF BRANCHING FRACTIONS AND
CP-VIOLATING ASYMMETRIES IN B MESON DECAYS
TO RHO AND PION FINAL STATES WITH THE BABAR
DETECTOR

by

JINWEI WU

A dissertation submitted in partial fulfillment of the
requirements for the degree of

DOCTOR OF PHILOSOPHY
(PHYSICS)

at the

UNIVERSITY OF WISCONSIN — MADISON

2005

© Copyright by JINWEI WU 2005

All Rights Reserved

Abstract

We present measurements of branching fractions and CP -violating asymmetries in B -meson decays to $\rho^+\pi^0$, $\rho^0\pi^+$ and $\rho^0\pi^0$. The data sample comprises 89×10^6 $\Upsilon(4S) \rightarrow B\bar{B}$ decays collected with the *BABAR* detector at the PEP-II asymmetric-energy B Factory at SLAC. We find the charge-averaged branching fractions $\mathcal{B}(B^+ \rightarrow \rho^+\pi^0) = (10.9 \pm 1.9(\text{stat}) \pm 1.9(\text{syst})) \times 10^{-6}$ and $\mathcal{B}(B^+ \rightarrow \rho^0\pi^+) = (9.5 \pm 1.1 \pm 0.9) \times 10^{-6}$, and we set a 90% confidence-level upper limit $\mathcal{B}(B^0 \rightarrow \rho^0\pi^0) < 2.9 \times 10^{-6}$. We measure the charge asymmetries $A_{CP}^{\rho^+\pi^0} = 0.24 \pm 0.16 \pm 0.06$ and $A_{CP}^{\rho^0\pi^+} = -0.19 \pm 0.11 \pm 0.02$.

We also present the preliminary measurement of CP -violating asymmetries in $B^0 \rightarrow (\rho\pi)^0 \rightarrow \pi^+\pi^-\pi^0$ decays using a time-dependent Dalitz plot analysis. The results are obtained from a data sample of 213 million $\Upsilon(4S) \rightarrow B\bar{B}$ decays, collected by the *BABAR* detector at the PEP-II asymmetric-energy B Factory at SLAC. This analysis extends the narrow- ρ quasi-two-body approximation used in the previous analysis, by taking into account the interference between the ρ resonances of the three charges. We measure 16 coefficients of the bilinear form factor terms occurring in the time-dependent decay rate of the B^0 meson with the use of a maximum-likelihood fit. We derive the physically relevant quantities from these coefficients. We measure the direct CP -violation parameters $\mathcal{A}_{\rho\pi} = -0.088 \pm 0.049 \pm 0.013$ and $C = 0.34 \pm 0.11 \pm 0.05$, where the first errors are statistical and the second systematic. For the mixing-induced

CP -violation parameter we find $S = -0.10 \pm 0.14 \pm 0.04$, and for the dilution and strong phase shift parameters respectively, we obtain $\Delta C = 0.15 \pm 0.11 \pm 0.03$ and $\Delta S = 0.22 \pm 0.15 \pm 0.03$. For the angle α of the Unitarity Triangle we measure $(113^{+27}_{-17} \pm 6)^\circ$; only a weak constraint is achieved at the significance level of more than two standard deviations. Finally, for the relative strong phase δ_{+-} between the $B^0 \rightarrow \rho^- \pi^+$ and $B^0 \rightarrow \rho^+ \pi^-$ transitions we find $(-67^{+28}_{-31} \pm 7)^\circ$, with a similarly weak constraint at two standard deviations and beyond.

Acknowledgements

I am grateful to my thesis advisor, Professor Sau Lan Wu. She introduced me into the field of experimental particle physics. Without her close guidance, this thesis work would not have been possible. She is also willing to help me not only with physics issues but with anything she can. She has provided me constant support during the past six and a half years.

The measurements presented in this dissertation are the results of the close collaboration of many people, including Nicolas Arnaud, Mathem Graham, Andreas Hoecker, Paul Kutter, Haibo Li, Ran Liu, Sandrine Laplace, Attila Mihalyi, Yibin Pan, Sau Lan Wu and Zhitang Yu. It is my great pleasure to work with them and many other colleagues of the *BABAR* experiments. Among them, Andreas Hoecker is extremely worth mentioning due to his superb talent, knowledge and passion for physics. He plays the leading role in most of the measurements presented in this dissertation. He is always optimistic, even in times of difficulties. I have learned enormously from him.

Contents

Abstract	i
Acknowledgements	iii
1 Theory	1
1.1 Introduction	1
1.2 CP violation	4
1.2.1 Mixing and time evolution of neutral mesons	6
1.2.2 Heavy neutral-meson systems	9
1.2.3 Three types of CP violation	11
1.2.4 Unitarity Triangle	13
1.3 $b \rightarrow u\bar{u}d$ Decays	15
1.4 $B \rightarrow \rho\pi$ Decays	18
1.4.1 Isospin Analysis of $B \rightarrow \rho\pi$	20
1.4.2 Dalitz Plot Analysis of $B^0 \rightarrow \pi^+\pi^-\pi^0$	22
2 PEP-II B Factory and <i>BABAR</i> Detector	30

2.1	PEP-II Asymmetric B Factory	31
2.2	Silicon Vertex Tracker	33
2.3	Drift Chamber	35
2.4	Detector of Internally Reflected Cherenkov Light	38
2.5	Electromagnetic Calorimeter	41
2.6	Instrumental Flux Return	43
2.7	Trigger	45
3	Analysis Overview	47
3.1	Signature of the Charmless Three-body B Decay	47
3.1.1	Decay Kinametics	47
3.1.2	Decay Topology	48
3.1.3	Suppression of B Related Background	51
3.2	Vertexing and Δt Determination	55
3.3	B -Flavour Tagging	56
3.4	Data Sample and Event Processing	58
3.5	Misreconstruction and Multiple Candidates	60
3.6	Maximum Likelihood Fit	61
3.7	Correlations	63
4	Study of $B^\pm \rightarrow \rho^\pm \pi^0$ Decays	65
4.1	Introduction	65
4.2	Candidate Selection	65

4.3	Backgrounds from B Decay	67
4.4	Systematic Uncertainties due to B -background	71
4.5	The Maximum Likelihood Fit	73
4.6	Fit Results	73
4.7	Study of the Systematic Uncertainties	75
4.8	Summary	79
5	Study of $B^\pm \rightarrow \rho^0 \pi^\pm$ Decay	82
5.1	Introduction	82
5.2	Candidate Selection	83
5.3	Validation of ΔE and m_{ES}	86
5.4	Backgrounds from B Decays	87
5.5	Systematic Uncertainty due to B -background	89
5.6	Maximum Likelihood Fit	89
5.7	Fit Results	91
5.8	Study of the Systematic Uncertainties	92
5.9	Summary	96
6	Study of $B^0 \rightarrow \rho^0 \pi^0$ Decay	98
6.1	Introduction	98
6.2	Selection	100
6.3	Backgrounds from B Decays	102
6.4	Maximum Likelihood Fit	102

6.5	Fit Results	103
6.6	Systematic Uncertainties on the Signal Yield	104
6.7	Setting the Upper Limit on the Branching Fraction	108
6.8	Summary	111
7	$B^0 \rightarrow \pi^+\pi^-\pi^0$ Dalitz Plot Analysis	112
7.1	Event Selection	112
7.2	Backgrounds from B Decay	117
7.3	Building the Likelihood	121
7.4	Fit Results	137
7.5	Study of the Systematic Uncertainties	142
7.6	Conclusions	148
A	The theory of Standard Model	149
A.1	The Standard Model	149
A.2	Discrete symmetry transformation	154
B	Isospin analysis of $B \rightarrow \pi\pi$	161
C	Dalitz plot	164
C.1	Introduction	164
C.2	The Square Dalitz Plot	170
C.3	The Signal Model for $B^0 \rightarrow \pi^+\pi^-\pi^0$	173
C.3.1	Vector Form Factor	173

C.3.2	Scalar Form Factor	175
C.3.3	Higher Resonances	177
C.3.4	Killer modes	178

List of Figures

1.1	<i>Leading order $B^0\bar{B}^0$ mixing diagrams</i>	7
1.2	<i>The rescaled Unitarity Triangle</i>	13
1.3	<i>Tree (left) and penguin (right) diagrams for the $b \rightarrow u\bar{u}d$ decay.</i>	15
1.4	<i>Color suppressed tree (left) and annihilation (right) diagrams for the $b \rightarrow u\bar{u}d$ decay.</i>	16
1.5	<i>A representation of interference terms in $B^0 \rightarrow \rho^\pm \pi^\mp$</i>	26
2.1	<i>BABAR detector longitudinal cross section.</i>	31
2.2	<i>Schematic view of SVT: longitudinal section. The roman numerals label the six different types of sensors.</i>	33
2.3	<i>Schematic view of SVT: transverse section.</i>	34
2.4	<i>Longitudinal section of the DCH with principal dimensions; the chamber center is offset by 370 mm from the interaction point.</i>	36
2.5	<i>Schematic layout of drift cells for the four innermost superlayers</i>	37
2.6	<i>Schematics of the DIRC fused silica radiator bar and imaging region.</i>	39
2.7	<i>Exploded view of the DIRC mechanical support structure.</i>	40

2.8	<i>A longitudinal cross section of the EMC</i>	42
2.9	<i>Overview of the IFR: Barrel sectors and forward and backward end doors; the shape of the PRC modules and their dimensions are indi- cated.</i>	44
3.1	<i>Distributions of m_{ES} and ΔE for various processes</i>	49
3.2	<i>Drawings of the decay topology of a generic signal event.</i>	50
3.3	<i>Distributions of the MVA output for signal and continuum events . . .</i>	51
3.4	<i>Performance curves for different MVA output</i>	52
3.5	<i>ΔE distributions for various processes in the enlarged ΔE band</i>	53
3.6	<i>Schematics of the determination of the decay time difference.</i>	56
3.7	<i>Number of candidates per event passing the full selection</i>	60
3.8	<i>Correlation profiles between different discriminating variables</i>	63
4.1	<i>CM energy difference, ΔE, versus the energy-substituted-mass, m_{ES} . .</i>	66
4.2	<i>Distributions of m_{ES}, ΔE for samples enhanced in $\rho^\pm\pi^0$ signal using likelihood ratio cuts</i>	75
4.3	<i>Distribution of m_ρ for samples enhanced in $\rho^\pm\pi^0$ signal using likelihood ratio cut</i>	76
5.1	<i>ΔE and $\pi^+\pi^-$ invariant mass distributions in the $B^\pm \rightarrow \rho^0\pi^\pm$ analysis for the various processes</i>	83

5.2	<i>Distributions of m_{ES}, ΔE for samples enhanced in $\rho^0\pi^\pm$ signal using likelihood ratio cuts</i>	93
5.3	<i>Distribution of NN output for sample enhanced in $\rho^0\pi^\pm$ signal using likelihood ratio cut.</i>	94
5.4	<i>Distributions of $m(\rho)$ and $\cos\theta_H(\rho)$ for samples enhanced in $\rho^0\pi^\pm$ signal using likelihood ratio cuts.</i>	95
6.1	<i>Distributions of m_{ES} and ΔE for samples enhanced in $\rho^0\pi^0$ signal content using cuts on the signal-to-continuum likelihood ratio</i>	105
7.1	<i>Optimization of the m_{+-} cut for Dalitz Plot analysis</i>	113
7.2	<i>Signal ΔE distributions on various regions of the Dalitz plot</i>	114
7.3	<i>Δt fits for various charged B-background modes</i>	120
7.4	<i>Δt distributions for various neutral B-backgrounds.</i>	122
7.5	<i>Selection efficiency and rate of signal misreconstruction on the Dalitz plot</i>	125
7.6	<i>Resolution of Dalitz plot variables for reconstructed signal events</i>	127
7.7	<i>Two dimensional resolution for selected points on the Dalitz plot</i>	129
7.8	<i>Square DPs for the decay $B^\pm \rightarrow \rho^\pm\pi^0$</i>	132
7.9	<i>Dalitz plot distributions for off-resonance events</i>	135
7.10	<i>Distribution of Δt for 22,145 GSB off-resonance events</i>	136
7.11	<i>Distributions of the fit variables for samples enhanced in $\rho\pi$ signal using likelihood ratio cuts</i>	139

7.12	α and δ_{+-} scan obtained from fit results, including both statistics and systematics covariance matrices	141
C.1	Convention adopted for the helicity angles.	166
C.2	Nominal and square $B^0 \rightarrow \pi^+\pi^-\pi^0$ Dalitz plots obtained from toy Monte Carlo without detector simulation	171
C.3	Jacobian determinant of the transformation from DP to SDP	172
C.4	Pion form factor from $e^+e^- \rightarrow \pi^+\pi^-$ annihilation and $\tau^+ \rightarrow \bar{\nu}_\tau \pi^+ \pi^0$ decays	177

List of Tables

1.1	Result of the charged and neutral Gounaris-Sakurai model	27
2.1	<i>PEP-II beam parameters</i>	32
4.1	$\rho^\pm\pi^0$ analysis: selection efficiencies for various processes	68
4.2	$\rho^\pm\pi^0$ analysis: signal efficiencies after final selection	69
4.3	Summary of fraction of misreconstructed signal events for $B^\pm \rightarrow \rho^0\pi^\pm$ events in different tagging categories	69
4.4	$\rho^\pm\pi^0$ analysis: Classification of background from charged and neutral B s	70
4.5	$\rho^\pm\pi^0$ analysis: B -background systematic errors	71
4.6	Summary of the final $\rho^\pm\pi^0$ fit prior to signal yield bias correction. . . .	74
4.7	The breakdown of systematic uncertainty for $B^\pm \rightarrow \rho^\pm\pi^0$ branching fraction measurement.	80
4.8	The breakdown of systematic uncertainty for $B^\pm \rightarrow \rho^\pm\pi^0$ charge asym- metry measurement.	81
5.1	$\rho^0\pi^\pm$ analysis: Summary of cut efficiencies for various processes	85

5.2	$\rho^0\pi^\pm$ analysis: signal efficiency, fraction of misreconstructed signal events (SCF) and mischarge rate of the candidate selection.	86
5.3	Summary of the results extracted from the $\bar{D}^0\pi^+$ fit.	87
5.4	Summary of the validation on the kinematic variables extracted from $\bar{D}^0\pi^+$ fit.	87
5.5	$\rho^0\pi^\pm$ analysis: classification of background from charged and neutral B s	90
5.6	Systematic errors due to the uncertainties of B -background branching fractions and possible charge asymmetries in $B^\pm \rightarrow \rho^0\pi^\pm$ analysis. . . .	91
5.7	Summary of the final $B^\pm \rightarrow \rho^0\pi^\pm$ fit result.	92
5.8	Summary of the systematic errors on the fitted signal yield in $B^\pm \rightarrow \rho^0\pi^\pm$.	97
5.9	Summary of the systematic errors on the fitted charge asymmetry in $B^\pm \rightarrow \rho^0\pi^\pm$ analysis.	97
6.1	$\rho^0\pi^0$ analysis: cut efficiencies for various processes	101
6.2	Summary of the selection efficiency of $B^0 \rightarrow \rho^0\pi^0$	102
6.3	Classifications of major B -background modes. A “*” indicates that the branching fraction is estimated.	103
6.4	The full $B^0 \rightarrow \rho^0\pi^0$ fit result on data.	104
6.5	B -background systematic on $\rho^0\pi^0$ yield	106
6.6	Contributions to the $B^0 \rightarrow \rho^0\pi^0$ signal yield uncertainty from sources other than B -background branching fractions.	107

6.7	<i>The breakdown of systematics for measurements of $B^0 \rightarrow \rho^0 \pi^0$ Branching Ratio.</i>	109
7.1	<i>Cut efficiencies for the Dalitz plot analysis</i>	116
7.2	<i>Misreconstructed event fractions in each tagging category.</i>	117
7.3	<i>Classification of B-background for the Dalitz plot analysis</i>	119
7.4	<i>Result after convergence of Run1-4 data fit. The arbitrary parameter U_+^+ is fixed to 1.</i>	138
7.5	<i>Q2B parameters extracted from Us and Is coefficients from Run1-4 data fit.</i>	140
7.6	<i>Summary of systematic uncertainties on the Us and Is coefficients.</i>	143
7.7	<i>Correlation matrix of systematic uncertainties for the Us and Is. Note that all elements above the diagonal are omitted for readability.</i>	147

Chapter 1

Theory

1.1 Introduction

According to the Standard Model of particle physics, matter is made up of six leptons and six quarks. These particles interact by exchanging bosons associated with the three fundamental forces: the strong force, the electromagnetic force, and the weak force. We believe that these interactions can be beautifully understood as consequences of gauge symmetries. Some relevant concepts are explained in Appendix A.

The Standard Model has been tremendously successful in describing experiments, apart from the Higgs boson still to be discovered. However, there are strong indications that we should not be satisfied with the theory. The main reasons are that there are conceptual indications for physics beyond the Standard Model. Unification of the strong and electroweak interactions has been achieved in the Standard Model. However, the gravitational interaction is not included in the Standard Model. Attempts to unify four interactions have proven unsuccessful. It is considered highly

implausible that the origin of the eletro-weak symmetry breaking can be explained by the standard Higgs mechanism without accompanying new phenomena. New physics should be manifested at energies in the TeV domain. This conclusion follows from the consideration of the validity of the Standard Model at very high energies. The structure of the Standard Model can not naturally explain the relative smallness of the weak scale of the mass, set by the Higgs mechanism. This so-called *hierarchy problem* is related to the presence of fundamental scalar fields in the theory with quadratic mass divergences and no protective extra symmetry.

In addition to theoretical consideration, there are many indication of physics beyond the Standard Model from experiments as well. Recent experiments have provided solid evidence for neutrino oscillations. Neutrino oscillations imply that neutrinos have mass. The smallness of any neutrino mass in comparison to quark and charged lepton masses indicates a different nature of neutrino masses. It is generally believed that neutrino masses provide a window into physics at the very large energy scale.

Interestingly, much of the evidence which show that new physics must exist comes not from studying the smallest composites of matter in the accelerators, but from studying the largest structures of the universe. Our visible universe itself contains a wealth of information. For example, most of the radiation in the universe that we observe today is in the form of an almost isotropic blackbody spectrum with a temperature of approximately 2.7K, and known as the *cosmic microwave background radiation* or CMB. It is believed to be a relic from the era of *recombination* when

protons and electrons combined into atoms and the universe became transparent to photons. The small angular fluctuations in the temperature of the CMB reveal a great deal about the constituents of the universe. Recent results from WMAP [7] show our universe to be made of approximately 73% dark energy and 23% dark matter by measuring the *anisotropy* in the CMB spectrum. Only less than 5% of the mass of the universe is made of our familiar luminous baryons. Unfortunately, the Standard Model does not provide viable candidate particles for either dark energy or dark matter.

Another unexplained mystery is *baryogenesis*, the formation of baryons. It could occur at the weak scale but not in the Standard Model. For baryogenesis one needs the three Sakharov conditions [1]: Baryon number violation, CP violation and no thermal equilibrium. The first requirement is based on a rather theoretical point of view. We believe that our universe is made of large number of baryons but few or no anti-baryons. Without introducing baryon number violation processes outside of the Standard Model, we would be forced to believe that the baryon number was established when the universe was created, and nothing in the present framework of physics gives us a clue about how to understand such a number. Without the second requirement of CP violation, equal numbers of baryons and antibaryons would be created or destroyed in any baryon number violation process if we started with equal numbers of baryons and antibaryons. The third requirement of baryogenesis is based on the fact that the particle density is a time-independent quantity once the equilibrium is established. Quantitative analysis shows that baryogenesis is not possible in the Standard Model

because there is not enough CP violation.

1.2 CP violation

CP violation was first discovered in the neutral kaon system in 1964 [4]. From appendix A, we see that CP violation can be accommodated in the framework of renormalizable theory of weak interaction. However, even forty years after the first discovery of CP violation, its origin remains unclear. On the one hand, an increasing number of experimental results from accelerators are consistent with the picture that CP violation is a result of the irreducible phase in the CKM matrix. On the other hand, the weak scale of CP violations in the Standard Model is difficult to explain the large matter and antimatter asymmetry in the universe. It is crucial to fully understand the origin of CP violation and to find other sources of CP violation beyond the Standard Model. In this process, the study of matrix elements involving the third generation of quarks provides a source of key information for understanding not only CP violation but the physics of flavor, and possibly new physics beyond the Standard Model as well.

In the many years following the discovery of CP violation, CP violation measurements are mostly performed in the kaon system. The asymmetric B -factories at SLAC and KEK opened a brand new chapter in the study of CP violation in the B meson decay. One of the great achievements of the B -factories at SLAC and KEK was the measurement of $\sin 2\beta$ to great precision where β is one angle of the Unitarity Triangle. The latest measurement by *BABAR* collaboration yields

$\sin 2\beta = 0.722 \pm 0.040(\text{stat}) \pm 0.023(\text{syst})$ [16], obtained using a sample of reconstructed charmonium and neutral kaons from the neutral B decay. The other two angles in the Unitarity Triangle need to be measured independently in order to test the Standard Model prediction. As the B -factories continue to run above their designed luminosities, an increasing number of different B -decay modes become accessible for investigation. Many of these modes carry interesting information on CP -violating interactions. One such example is the Cabbibo suppressed charmless modes with a contribution from $b \rightarrow u\bar{u}d$ which would be the subject of this dissertation.

The current knowledge at 90% confidence level of the magnitude of the quark mixing matrix, the CKM matrix ¹, is summarized here [12]

$$\begin{pmatrix} 0.9741 - 0.9756 & 0.219 - 0.226 & 0.00025 - 0.0048 \\ 0.219 - 0.226 & 0.9732 - 0.9748 & 0.038 - 0.044 \\ 0.004 - 0.014 & 0.037 - 0.044 & 0.9990 - 0.9993 \end{pmatrix} \quad (1.1)$$

The salient features are that the diagonal terms are much bigger than the rest. The weak transitions in the heavier quark sector are much more suppressed than those in the lighter quark section and the transition between the first generation and third generation is the weakest of all. The original parameterization of the CKM matrix in equation A.16 reduces to the Glashow-Iliopoulos-Miani model in the limit $\theta_1 = \theta_C$, $\sin \theta_2, \sin \theta_3 \rightarrow 0$, and $\delta \rightarrow 0$. But the matrix elements can have large imaginary parts.

¹Introduced in Appendix A.

These large imaginary parts do not give appreciable CP -nonconservation effects since a redefinition of top and bottom quark fields can make all the matrix elements real up to order of $O(10^{-3})$ if one considers the hierarchy of the matrix elements above. One commonly used parametrization, written as an expansion of V_{us} , is given by Wolfenstein [8]

$$\begin{pmatrix} 1 - \lambda^2/2 & \lambda & A\lambda^3(\rho + i\eta) \\ -\lambda & 1 - \lambda^2/2 & A\lambda \\ A\lambda^3(1 - \rho - i\eta) & -A\lambda^2 & 1 \end{pmatrix} + \mathcal{O}(\lambda^4) \quad (1.2)$$

where the A , ρ and η are all of order one. The Wolfenstein parametrization has proven to be very useful in the study of heavy flavor physics.

1.2.1 Mixing and time evolution of neutral mesons

A feature that is crucial to our study of the heavy meson system is the mixing phenomenon. That is to say there are flavor changing neutral currents induced by the box diagrams shown in figure 1.1. The evolution of a neutral heavy meson state can be described by a hermitian mass matrix M and a hermitian damping matrix Γ , which are the hermitian and anti-hermitian parts of the energy matrix, $\Lambda = M - i/2\Gamma$. CPT invariance guarantees that $\Lambda_{11} = \Lambda_{22}$. Using B meson as an example, we write the time-dependent amplitudes ψ as linear combinations of B^0 and \bar{B}^0 fields. They are determined by the Schrödinger equation. In the simple case where we ignore the mixing, Λ is diagonal. We restore the free propagation of the decaying fields. In reality,

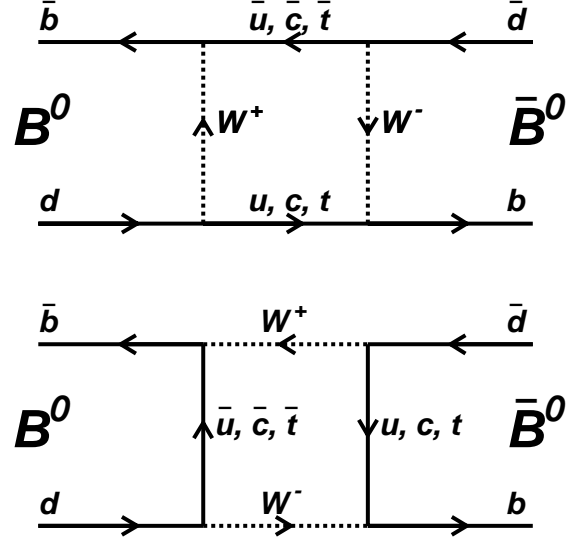


Figure 1.1: *Leading order $B^0 \bar{B}^0$ mixing diagrams*

the off diagonal terms in Λ are non-zero due to the mixing diagrams. In particular, they contain complex numbers from the CKM matrix. The general solution is given by the mixture of flavor eigenstates. To analyze the problem more easily, one can go to a basis that diagonalize the matrix Λ . Its eigenstates, defined by

$$(M - i\Gamma) \psi_{\pm} = \lambda_{\pm} \psi_{\pm} \quad (1.3)$$

are

$$\psi_{\pm} = \frac{1}{\sqrt{|p|^2 + |q|^2}} \begin{pmatrix} p \\ \pm q \end{pmatrix} \quad (1.4)$$

Note that the new eigenstates need not to be orthogonal to each other. In the new basis, the state function can be expressed in terms of these two eigenstates ψ_{\pm} as

$$\psi(t) = \frac{1}{\sqrt{a'^2 + b'^2}} [a' \psi_+ e^{-i\lambda_+ t} + b' \psi_- e^{-i\lambda_- t}] \quad (1.5)$$

where a' and b' provide the initial state of the system. Let's calculate the probability that a pure B^0 produced at time zero is found to be a \bar{B}^0 at time t . From equation 1.4, a pure B^0 is made of $(\psi_+ + \psi_-)$ and pure \bar{B}^0 is made of $(\psi_+ - \psi_-)$. Based on equation 1.5, we have

$$\begin{aligned} \psi(t)_{K^0} &= \frac{1}{\sqrt{2}} [\psi_+ e^{-i\lambda_+ t} + \psi_- e^{-i\lambda_- t}] \\ &= \frac{1}{\sqrt{2}} \frac{p}{\sqrt{p^2 + q^2}} \left[g_+(t) \psi_{K^0} + \frac{q}{p} g_-(t) \psi_{\bar{K}^0} \right] \end{aligned} \quad (1.6)$$

where

$$g_{\pm}(t) = \frac{1}{2} (e^{-i\lambda_+ t} \pm e^{-i\lambda_- t}) \quad (1.7)$$

And immediately, we have the probability

$$|\langle \psi_{\bar{B}^0} | \psi(t)_{B^0} \rangle|^2 = \frac{|q|^2}{2(p^2 + q^2)} (e^{-i\lambda_+ t} - e^{-i\lambda_- t})^2 \quad (1.8)$$

Similarly, we can write down the probability for the CP conjugate process. If CP were a perfect symmetry, one would expect that the two probabilities to be identical which would imply that $|p| = |q|$ or that the mass eigenstates ψ_{\pm} coincide with the

CP eigenstates. If $|p| \neq |q|$, CP is violated and we call this type of CP violation *CP violation in mixing*. Note that if the mass matrix and the damping matrix are real, $p = \pm q$. Thus, no CP violation could occur in the mixing process.

1.2.2 Heavy neutral-meson systems

After understanding how a neutral meson can evolve with time, we can consider the production and decay of a pair of heavy mesons such as $D^0 \bar{D}^0$, $B_d^0 \bar{B}_d^0$. The production of the mesons is dominated either by the strong interaction, as in $p\bar{p}$ collisions, or by the electromagnetic interaction, as in the process $e^+e^- \rightarrow \Upsilon(4S) \rightarrow B^0 \bar{B}^0$. Throughout this section, we use $B^0 \bar{B}^0$ as an example. $\Upsilon(4S)$ is a $b\bar{b}$ bound state with spin 1 and C-parity $\eta_c = -1$. The initial pair of $B^0 \bar{B}^0$ produced from $\Upsilon(4S)$ is in a p wave state

$$|\Phi\rangle = \frac{1}{\sqrt{2}} \left[|B^0(\vec{k})\rangle \otimes |\bar{B}^0(-\vec{k})\rangle - |\bar{B}^0(\vec{k})\rangle \otimes |B^0(-\vec{k})\rangle \right] \quad (1.9)$$

If the meson with momentum \vec{k} decays at time t_1 into final state f , and the meson with momentum $-\vec{k}$ decays at time t_2 into final state g . Using equation 1.6, the amplitude for this process would be

$$\begin{aligned} A(t_1, t_2) = & C e^{-(\Gamma/2 + iM)(t_1 + t_2)} \zeta(t_1, t_2) \\ & \left\{ \cos\left(\frac{\Delta m_d}{2}(t_1 - t_2)\right) (A_1 \bar{A}_2 - \bar{A}_1 A_2) - \right. \\ & \left. i \sin\left(\frac{\Delta m_d}{2}(t_1 - t_2)\right) \left(\frac{p}{q} A_1 A_2 - \frac{q}{p} \bar{A}_1 \bar{A}_2\right) \right\} \end{aligned} \quad (1.10)$$

where A_i is the amplitude for a B^0 to decay to the state f_i , \bar{A}_i is the amplitude for a \bar{B}^0 to decay to the same state f_i . The ζ function returns ± 1 depending on which B decay first. Here an integral over all directions for either B has been performed, so the angular dependence has dropped out of the expressions, and an overall normalization factor C appeared.

To study of CP violation in such a system, one often needs to determine the flavour of a decaying neutral meson and this process is usually called *tagging*. When the initial \bar{B}^0 meson evolves in time, it oscillates back and forth into and from B^0 . The same occurs with the initial B^0 . But the anti-symmetry of the correlated wave function under the change $\vec{k} \rightarrow -\vec{k}$ is preserved by the linearity of the evolution. Hence, if at some instant t_2 the right-moving meson is found to be B^0 from its flavour-tagging decay g , then the left-moving meson *at that instant* must be a \bar{B}^0 . And decay rate is proportional to

$$\begin{aligned}
 R(t_{\text{tag}}, t_{f_{CP}}) &= C e^{-\Gamma(t_{\text{tag}}, t_{f_{CP}})} |\bar{A}_{\text{tag}}|^2 |A_{CP}|^2 \\
 &\quad \{1 + |\lambda|^2 + \cos[\Delta m_d(t_{f_{CP}} - t_{\text{tag}})] (1 - |\lambda|^2) - \\
 &\quad 2 \sin[\Delta m_d(t_{f_{CP}} - t_{\text{tag}})] \text{Im}(\lambda)\}
 \end{aligned} \tag{1.11}$$

where

$$\lambda = \frac{q}{p} \frac{\bar{A}_{f_{CP}}}{A_{f_{CP}}} \tag{1.12}$$

1.2.3 Three types of CP violation

We have seen that CP violation can occur during the mixing processes of neutral mesons. In fact, CP violation can manifest itself in two other ways as well.

CP violation in decay

Complex parameters in any Lagrangian term that contributes to the amplitude will appear in a complex conjugate form in the CP conjugate amplitude. In the Standard Model these phases occur only in the CKM matrix which is the electroweak sector of the theory. Hence these are often called *weak phases*. A second type of phase can appear in scattering or decay amplitudes even when the Lagrangian is real. Such phases do not violate CP , since they appear in CP conjugate states with the same sign. Their origin is the possible contribution from intermediate on-shell states in the decay process, that is an absorptive part of an amplitude that has contributions from coupled channels. The dominant rescattering is usually due to strong interactions, so the designation *strong phases* for the phase shifts so induced.

It is convenient to write each contribution to a decay process A in three parts: its magnitude A_i , its weak-phase $e^{i\phi_i}$ and its strong phase term $e^{i\delta}$. Writing the amplitude of B^0 decay final state f A_f and the amplitude for its CP conjugate process explicitly, we have

$$A_f = \sum_i A_i e^{i(\delta_i + \phi_i)}, \quad \bar{A}_{\bar{f}} = e^{2i\epsilon} \sum_i A_i e^{i(\delta_i - \phi_i)} \quad (1.13)$$

where the additional phase ϵ accounts for the phase differences between $|\bar{B}^0\rangle$ and $CP|B^0\rangle$ and between \bar{f} and $CP|f\rangle$. If CP is conserved, all the weak phases ϕ_i should

be equal. Thus the sufficient condition of CP violation in this case is $|\bar{A}_{\bar{f}}/A_f| \neq 1$.

The CP violating asymmetry is defined as

$$A_{CP} \equiv \frac{|A_f|^2 - |\bar{A}_{\bar{f}}|^2}{|A_f|^2 + |\bar{A}_{\bar{f}}|^2} = -\frac{\sum_{i,j} \sin(\phi_i - \phi_j) \sin(\delta_i - \delta_j)}{\sum_{i,j} \cos(\phi_i - \phi_j) \cos(\delta_i - \delta_j)} \quad (1.14)$$

Clearly, we need at least two amplitudes with both different weak phases and different strong phases in order to have non-zero CP violation in decay. It is worthwhile noting that this asymmetry is the largest when both amplitudes are the same and both the weak-phase and strong-phase differences are 90° . In reality, none of the above conditions are easily satisfied in certain decay modes. In order to find above criteria to be satisfied, one sometimes looks at rare decay modes, which by themselves are challenging to measure. In particular, due to the presence of a strong phase differences, it is hard to predict the amount of CP violation in decay for any mode.

CP violation in the interference between mixing and decay

Consider neutral meson decays into final CP eigenstates, f_{CP} . Let us consider the B decay as an example. We have a model-independent estimation that $\Delta\Gamma_B \ll \Delta m_B$. This implies that $\lambda_{\pm} \approx m_{11} - \frac{i}{2}\Gamma_{11} \mp m_{12}$. When CP is conserved, $|q/p| = 1$, $|\bar{A}_{\bar{f}}/A_f| = 1$ and furthermore, the relative phase between them vanishes. Therefore,

$$\lambda \neq \pm 1 \implies CP \text{ violation} \quad (1.15)$$

It is possible that, to a good approximation, $|q/p| = 1$ and $|\bar{A}_{\bar{f}}/A_f| = 1$, yet

there is CP violation. In this case the phase of λ does not equal to zero. This type of CP violation is called CP violation in the interference between mixing and decay. For the neutral B system, CP violation in the interference between decays with and without mixing can be observed by comparing decays into final CP eigenstates of a time-evolving neutral B state that begins at time zero as B^0 to those of the state that begins as \bar{B}^0 :

$$a_{f_{CP}} = \frac{\Gamma(B^0(t) \rightarrow f_{CP}) - \Gamma(\bar{B}^0(t) \rightarrow f_{CP})}{\Gamma(B^0(t) \rightarrow f_{CP}) + \Gamma(\bar{B}^0(t) \rightarrow f_{CP})} \quad (1.16)$$

Using equation 1.11, the above asymmetry is given by:

$$a_{f_{CP}} = \frac{1 - |\lambda|^2}{1 + |\lambda|^2} \cos(\Delta m_d t) - \frac{2 \text{Im} \lambda}{1 + |\lambda|^2} \sin(\Delta m_d t) \quad (1.17)$$

1.2.4 Unitarity Triangle

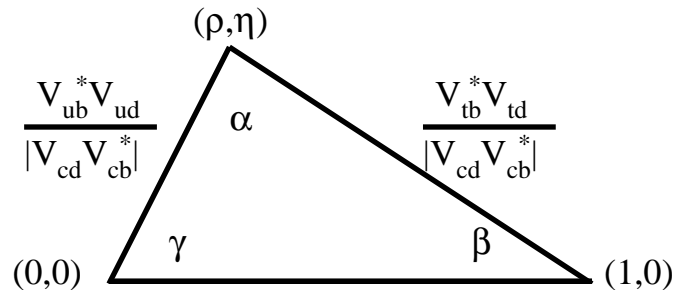


Figure 1.2: *The rescaled Unitarity Triangle*

The unitarity of the CKM matrix implies various relations among its elements. Three of them are extremely useful for understanding the Standard Model predictions

of CP violation

$$V_{ud}V_{us}^* + V_{cd}V_{cs}^* + V_{td}V_{ts}^* = 0 \quad (1.18)$$

$$V_{us}V_{ub}^* + V_{cs}V_{cb}^* + V_{ts}V_{tb}^* = 0 \quad (1.19)$$

$$V_{ud}V_{ub}^* + V_{cd}V_{cb}^* + V_{td}V_{tb}^* = 0 \quad (1.20)$$

Each of these three relations requires the sum of three complex quantities to vanish and so they can be geometrically represented in the complex plane as triangles. These are “the unitarity triangles”. And the term “Unitarity Triangle” is reserved for the last of the three relations. A drawing of the Unitarity Triangle is shown in Figure 1.2. All three unitarity triangles have the same area $J/2$ where J is the Jarlskog parameter [9] defined in the following equation

$$Im [V_{ij}V_{kl}V_{il}^*V_{kj}^*] = J \sum_{m,n=1}^3 \epsilon_{ikm}\epsilon_{jln} \quad (1.21)$$

The zero area of J will immediately imply CP conservation in the Standard Model.

The three angles of the Unitarity Triangle as defined in Figure 1.2 are denoted α , β and γ :

$$\alpha \equiv \arg \left[-\frac{V_{td}V_{tb}^*}{V_{ud}V_{ub}^*} \right], \quad \beta \equiv \arg \left[-\frac{V_{cd}V_{cb}^*}{V_{td}V_{tb}^*} \right], \quad \gamma \equiv \arg \left[-\frac{V_{ud}V_{ub}^*}{V_{cd}V_{cb}^*} \right] \quad (1.22)$$

1.3 $b \rightarrow u\bar{u}d$ Decays

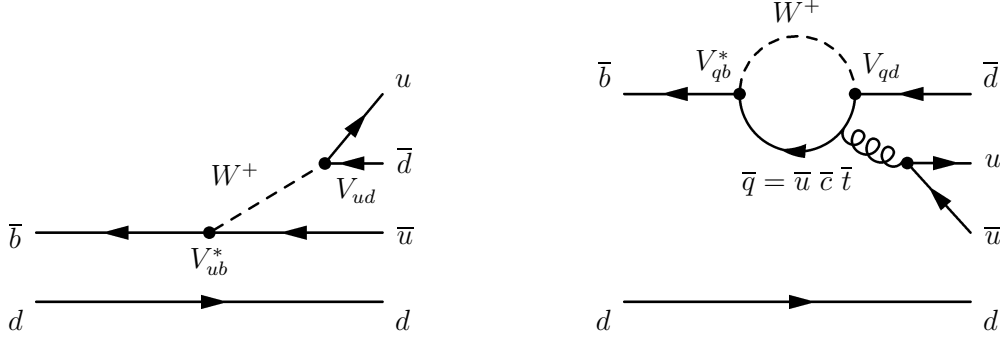


Figure 1.3: *Tree (left) and penguin (right) diagrams for the $b \rightarrow u\bar{u}d$ decay.*

In principle, any $b \rightarrow u\bar{u}d$ decay is a possible source for measuring the angle α of the Unitarity Triangle. Candidates include $B^0 \rightarrow \pi^+\pi^-$, $B^0 \rightarrow \rho^\pm\pi^\mp$, and $B^0 \rightarrow \rho^+\rho^-$. All of them share the same Feynman diagrams at the quark level. Figure 1.3 shows the dominant diagrams that contribute to the final states containing charged particles. Their differences come in the final state interaction where different mesons are formed. In the case where the B^0 decays into two neutral particles, the tree diagrams are color suppressed, as shown in Figure 1.4. In this case, the electroweak penguin and annihilation diagrams could play an important role. Contrary to the clean determination of β , the determination of α is complicated by the presence of penguin contributions in such decays. Appendix B shows how the weak phase α is entangled with the strong phase and penguin amplitude in the simple case of $B^0 \rightarrow \pi^+\pi^-$.

The quantitative analysis of B decays is currently based on “effective” theory calculations. In this approach, heavy degrees of freedom in EW and QCD Hamiltonians are integrated out. That allows separation of the short and long-range interactions

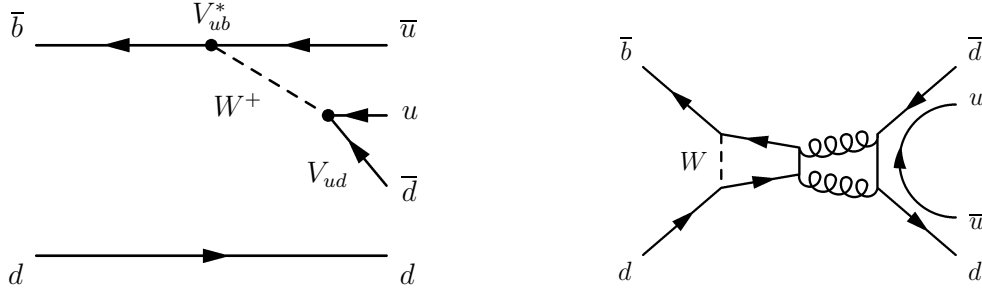


Figure 1.4: *Color suppressed tree (left) and annihilation (right) diagrams for the $b \rightarrow u\bar{u}d$ decay.*

in the effective Hamiltonian. Non-leptonic, two-body B -meson decays, although simple as far as the underlying weak decay of the b quark is concerned, are complicated on account of strong interaction effects. Weak decay of heavy mesons involve three fundamental scales, the weak interaction scale M_W , the b -quark mass m_b and the QCD scale Λ_{QCD} , which are strongly ordered: $M_W \gg m_b \gg \Lambda_{\text{QCD}}$. The underlying weak decay being computable, all theoretical work concerns strong interaction corrections. The amplitude for the two-body decay $B \rightarrow M_1 M_2$ is given by:

$$A(B \rightarrow M_1 M_2) = \frac{G_F}{\sqrt{2}} \sum_i \lambda_i C_i(\mu) \langle M_1 M_2 | \mathcal{O}_i | B \rangle(\mu), \quad (1.23)$$

where G_F is the Fermi constant. Each term in the sum is the product of a CKM factor λ_i , a coefficient function $C_i(\mu)$, which incorporates strong-interaction effects above the scale $\mu \sim m_b$, and a matrix element of an operator \mathcal{O}_i in the weak effective Hamiltonian. For a long time, the matrix elements have been estimated in the “naive” factorization approach, which replaces the matrix elements of a four-fermion operator in a heavy-quark decay by the product of the matrix elements of two currents, for

example,

$$\langle \pi^+ \pi^- | (\bar{u}b)(\bar{d}u) | \bar{B}^0 \rangle \longrightarrow \langle \pi^- | (\bar{d}u) | 0 \rangle \langle \pi^+ | (\bar{u}b) | \bar{B}^0 \rangle \quad (1.24)$$

This assumes that the exchange of “non-factorizable” gluons between the π^- and the $(\bar{B}^0 \pi^+)$ system can be neglected, if the virtuality of the gluons is below $\mu \sim m_b$. The non-leptonic decay amplitude reduces to the product of a form factor and a decay constant. In many cases this approach provides the correct order of magnitude of branching fractions, but it cannot predict direct CP violation due to the assumption of no strong rescattering. It is therefore no longer adequate for a detailed phenomenological analysis of B -factory data. Naive factorization has now been superseded by *QCD factorization* (QCD FA) [18]. The QCD FA predicts that in the limit $m_b \gg \Lambda_{\text{QCD}}$, the same matrix elements can be represented in the form

$$\begin{aligned} \langle \pi^+ \pi^- | (\bar{u}b)(\bar{d}u) | \bar{B}^0 \rangle &= \langle \pi^- | (\bar{d}u) | 0 \rangle \langle \pi^+ | (\bar{u}b) | \bar{B}^0 \rangle \\ &\times \left[1 + \sum_n r_n \alpha_s^n + \mathcal{O}(\Lambda_{\text{QCD}}/m_b) \right] \end{aligned} \quad (1.25)$$

Neglecting power corrections in Λ_{QCD} and radiative corrections in α_s , the original matrix elements return to the conventional factorization. At higher order in α_s this simple factorization breaks down, but the corrections can be calculated systematically in terms of short-distance coefficients. If this limit works well, QCD FA allows us to calculate strong phases systematically; CP violating weak phases can then be disentangled. It is important to measure all possible decay final states in order to test the

validity of the QCD FA scheme.

1.4 $B \rightarrow \rho\pi$ Decays

As in the case of $B \rightarrow \pi\pi$ modes, the $B \rightarrow \rho\pi$ channels provide an independent means of extracting the CKM phase α and another test ground for phenomenological models such as QCD FA. The penguin operator is expected to be suppressed for decays into vector mesons, like ρ . $B \rightarrow \rho\pi$ also has a larger branching fraction than $B \rightarrow \pi\pi$. However, unlike the case of $B^0 \rightarrow \pi^+\pi^-$, the $\rho^\pm\pi^\mp$ final states are not CP eigenstates. This further complicates the extraction of α . *BABAR* recently reported the measurement of the branching fraction as well as the time-dependent CP violating asymmetries in $B^0 \rightarrow \rho^\pm\pi^\mp$ [37]. Although $B^\pm \rightarrow \rho^0\pi^\pm$ have been measured by both CLEO [38] and Belle [39], $B^\pm \rightarrow \rho^\pm\pi^0$ and $B^0 \rightarrow \rho^0\pi^0$ have not been observed before.

To understand in particular the CP properties of such decays, it is convenient to represent the complex Standard Model amplitudes of the relevant processes as the sum of tree (T) and penguin (P) amplitudes with different weak and strong phases. The transition amplitudes are given by²

$$\begin{aligned} A^{+-} &= T^{+-}e^{+i\gamma} - P^{+-}e^{-i\beta}, & \bar{A}^{+-} &= T^{-+}e^{-i\gamma} - P^{-+}e^{+i\beta}, \\ A^{-+} &= T^{-+}e^{+i\gamma} - P^{-+}e^{-i\beta}, & \bar{A}^{-+} &= T^{+-}e^{-i\gamma} - P^{+-}e^{+i\beta}, \\ A^{00} &= T^{00}e^{+i\gamma} - P^{00}e^{-i\beta}, & \bar{A}^{00} &= T^{00}e^{-i\gamma} - P^{00}e^{+i\beta}, \end{aligned} \quad (1.26)$$

²The first superscript stands for the charge of the ρ and the second superscript stands for the charge of the π . And the bar stands for the flavor of the B , *e.g.* $\bar{A}^{+-} \equiv A(\bar{B}^0 \rightarrow \rho^+\pi^-)$. The same convention apply to B^+ decay as well.

where we have absorbed the modules of the CKM elements $|V_{ud}V_{ub}^*| \simeq A\lambda^3\sqrt{\bar{\rho}^2 + \bar{\eta}^2}$ and $|V_{td}V_{tb}^*| \simeq A\lambda^3\sqrt{(1 - \bar{\rho})^2 + \bar{\eta}^2}$ in the effective tree ($T^{\kappa\sigma}$) and penguin ($P^{\kappa\sigma}$) amplitudes, respectively. The $T^{\kappa\sigma}$ and $P^{\kappa\sigma}$ are unknown complex numbers which must be determined from data. We have used the $\mathcal{O}(\lambda^5)$ unitarity relation $R_u e^{i\gamma} + R_c e^{i\pi} + R_t e^{-i\beta} = 0$ to remove the c quark loops in the penguin amplitudes. The effective tree and penguin amplitudes used in Eqs. (1.26) are then given by $T \equiv T_u + P_u - P_c$ and $P \equiv P_t - P_c$, where the indices denote the quark flavor involved.

Using $\pi - \alpha = \beta + \gamma$, multiplying by a global phase $e^{i(\pi+\beta)}$, including the $B^0\bar{B}^0$ mixing phase $\arg[q/p] \simeq e^{-2i\beta}$ in the \bar{A} amplitudes, and factorizing the tree amplitude, one arrives at³

$$\begin{aligned}
A^{+-} &= |T^{+-}|e^{i\delta_T^{+-}} \left(e^{-i\alpha} + r^{+-}e^{i\delta_r^{+-}} \right), & \bar{A}^{+-} &= |T^{-+}|e^{i\delta_T^{-+}} \left(e^{+i\alpha} + r^{-+}e^{i\delta_r^{-+}} \right), \\
A^{-+} &= |T^{-+}|e^{i\delta_T^{-+}} \left(e^{-i\alpha} + r^{-+}e^{i\delta_r^{-+}} \right), & \bar{A}^{-+} &= |T^{+-}|e^{i\delta_T^{+-}} \left(e^{+i\alpha} + r^{+-}e^{i\delta_r^{+-}} \right), \\
A^{00} &= |T^{00}|e^{i\delta_T^{00}} \left(e^{-i\alpha} + r^{00}e^{i\delta_r^{00}} \right), & \bar{A}^{00} &= |T^{00}|e^{i\delta_T^{00}} \left(e^{+i\alpha} + r^{00}e^{i\delta_r^{00}} \right),
\end{aligned} \tag{1.27}$$

where we defined the ratios $r^\kappa e^{i\delta_r^\kappa} \equiv P^\kappa/T^\kappa$. Equations (1.27) define the amplitude conventions that are used in this analysis.

³Note that the equality $\arg[q/p] = e^{-2i\beta}$ is only valid to the Wolfenstein order $\mathcal{O}(\lambda^5)$, since V_{cd} , entering the definition of β has a small phase, which is not present in $B^0\bar{B}^0$ mixing. Along the same line, charmless $b \rightarrow u$ transitions only approximately measure α , which is of course academic for the current experimental accuracy.

1.4.1 Isospin Analysis of $B \rightarrow \rho\pi$

While it is not sufficient to extract α from only $B^0 \rightarrow \rho^\pm \pi^\mp$ decays, one way in which α can be extracted is the extended version of the isospin analysis of the $B \rightarrow \pi\pi$ [19], which is briefly explained in Appendix B. In this approach, one works in the limit of SU(2) flavor symmetry (neglecting electro-weak penguins) and in a quasi-two-body framework which treats ρ as a narrow resonance. It requires the measurement of the decay rates and CP violating asymmetries of all $B \rightarrow \rho\pi$ decays. The isospin decompositions of five $B \rightarrow \rho\pi$ amplitudes are given by [19]:

$$\begin{aligned}
A^{+0} &= \frac{1}{2}\sqrt{\frac{3}{2}}A_{3/2,2} - \frac{1}{2}\sqrt{\frac{1}{2}}A_{3/2,1} + \sqrt{\frac{1}{2}}A_{1/2,1} \\
A^{0+} &= \frac{1}{2}\sqrt{\frac{3}{2}}A_{3/2,2} + \frac{1}{2}\sqrt{\frac{1}{2}}A_{3/2,1} - \sqrt{\frac{1}{2}}A_{1/2,1} \\
A^{+-} &= \frac{1}{2}\sqrt{\frac{1}{3}}A_{3/2,2} - \frac{1}{2}A_{3/2,1} + \frac{1}{2}A_{1/2,1} - \sqrt{\frac{1}{6}}A_{1/2,0} \\
A^{-+} &= \frac{1}{2}\sqrt{\frac{1}{3}}A_{3/2,2} + \frac{1}{2}A_{3/2,1} - \frac{1}{2}A_{1/2,1} - \sqrt{\frac{1}{6}}A_{1/2,0} \\
A^{00} &= \sqrt{\frac{1}{3}}A_{3/2,2} + \sqrt{\frac{1}{6}}A_{1/2,0}
\end{aligned} \tag{1.28}$$

where a detailed derivation of the decomposition of A^{+-} is given below⁴. Notably, there are $\Delta I = 1/2$ components in the charged B decay into $\rho\pi$ final states, which implies a possible penguin contribution. Therefore, there is possible direct CP violation in the charged B decay. It is clear from Equation 1.28 that there are only two independent penguin contributions,

$$P^{+0} = -P^{0+} = \frac{1}{\sqrt{2}}(P^{+-} - P^{-+}) \quad (1.30)$$

$$P^{00} = -\frac{1}{2}(P^{+-} + P^{-+}) \quad (1.31)$$

A construction similar to the isospin triangle for $\pi\pi$ can be made in the $\rho\pi$ case. From the above, one has the following equation:

$$\sqrt{2}(A^{+0} + A^{0+}) = A^{+-} + A^{-+} + A^{00} \quad (1.32)$$

⁴The isospin decomposition of A^{+-} is given by,

$$\begin{aligned} A^{+-} &= \langle \rho^+, \pi^- | H_{\text{eff}} | u\bar{u}\bar{d}, d \rangle \\ &= (\langle 1, 1 | \otimes \langle 1, -1 |) H_{\text{eff}} (| 3/2, 1/2 \rangle \otimes | 1/2, -1/2 \rangle) + \\ &\quad (\langle 1, 1 | \otimes \langle 1, -1 |) H_{\text{eff}} (| 1/2, 1/2 \rangle \otimes | 1/2, -1/2 \rangle) \\ &= \left(\frac{1}{\sqrt{6}} \langle 2, 0 | + \frac{1}{\sqrt{2}} \langle 1, 0 | + \frac{1}{\sqrt{3}} \langle 0, 0 | \right) H_{\text{eff}} \left(\frac{1}{\sqrt{2}} \langle 2, 0 |_{3/2} + \frac{1}{\sqrt{2}} \langle 1, 0 |_{3/2} \right) + \\ &\quad \left(\frac{1}{\sqrt{6}} \langle 2, 0 | + \frac{1}{\sqrt{2}} \langle 1, 0 | + \frac{1}{\sqrt{3}} \langle 0, 0 | \right) H_{\text{eff}} \left(\frac{1}{\sqrt{2}} \langle 2, 0 |_{1/2} + \frac{1}{\sqrt{2}} \langle 1, 0 |_{1/2} \right) \\ &= \frac{1}{2} \sqrt{\frac{1}{3}} \langle 2, 0 | H_{\text{eff}} | 2, 0 \rangle_{3/2} + \frac{1}{2} \langle 1, 0 | H_{\text{eff}} | 1, 0 \rangle_{3,2} + \frac{1}{2} \langle 1, 0 | H_{\text{eff}} | 1, 0 \rangle_{1,2} + \sqrt{\frac{1}{6}} \langle 0, 0 | H_{\text{eff}} | 0, 0 \rangle_{1,2} \\ &= \frac{1}{2} \sqrt{\frac{1}{3}} A_{3/2,2} + \frac{1}{2} A_{3/2,1} + \frac{1}{2} A_{1/2,1} + \sqrt{\frac{1}{6}} A_{1/2,0} \end{aligned} \quad (1.29)$$

In the derivation, we use explicitly that the effective Hamiltonian H_{eff} conserves strong isospin. The subscripts label the change in isospin ΔI in the b -quark decay.

A similar relation holds for the charge conjugate states. The relative phase between the amplitudes

$$A^{+-} + A^{-+} + 2A^{00} \quad \text{and} \quad \bar{A}^{+-} + \bar{A}^{-+} + 2\bar{A}^{00}, \quad (1.33)$$

is then -2α . The geometric figures to be constructed in the case of $B \rightarrow \rho\pi$ are pentagons rather than triangles. In order to get α , one has to effectively solve a number of higher-order algebraic equation for this system. Thus the solution can be obtained only up to multiple discrete ambiguities. In the absence of penguin contributions, only the combinations $\sin(2\alpha \pm \hat{\delta})$ are observed, where $\hat{\delta} = \arg[A^{-+}A^{+-*}]$. Eight mirror solutions for α and $\hat{\delta}$ are identified

$$\begin{array}{cccccccc} \alpha & \rightarrow & \pi/4 - \hat{\delta}/2 & \pi/2 + \alpha & 3\pi/4 - \hat{\delta}/2 & \pi/4 + \hat{\delta}/2 & \pi/2 - \alpha & 3\pi/4 + \hat{\delta}/2 & \pi - \alpha \\ \hat{\delta} & \rightarrow & \pi/2 - 2\alpha & \pi + \hat{\delta} & 3\pi/2 - 2\alpha & -\pi/2 + 2\alpha & -\hat{\delta} & -3\pi/2 + 2\alpha & \pi - \hat{\delta} \end{array}$$

(1.34)

Given the effect of experimental errors and the multiple ambiguities, we can at best hope to get a constraint on α .

1.4.2 Dalitz Plot Analysis of $B^0 \rightarrow \pi^+\pi^-\pi^0$

So far, we have been working under the assumption that ρ is a stable narrow resonance. In reality, ρ -mesons have non-negligible decay width and decay dominantly into two pions. Several other hadronic resonances and non-resonant $B^0 \rightarrow 3\pi$ may

contribute to the same final states. It was first shown by Snyder and Quinn [20] that a time-dependent Dalitz plot analysis of $B^0 \rightarrow \pi^+\pi^-\pi^0$ decay can over-constrain the *a priori* unknown parameters of the various complex amplitudes by exploiting the interference between the amplitudes of intermediate states dominated by $B^0 \rightarrow \rho^+\pi^-$, $B^0 \rightarrow \rho^-\pi^+$ and the color-suppressed and yet unmeasured $B^0 \rightarrow \rho^0\pi^0$, using SU(2) flavor symmetry. With sufficient statistics, this leads to an unambiguous determination of the angle α of the Unitarity Triangle. The full Dalitz plot analysis is thus the natural extension of the narrow- ρ -approximation, quasi-two-body analysis, performed with smaller data samples.

Time Dependence

To develop the time-dependent formalism, we will use in the following the zeroth-order assumption that the amplitude $\mathcal{A}_{3\pi}$ and its complex conjugate $\bar{\mathcal{A}}_{3\pi}$ are dominated by the three resonances $\rho^+(770)$, $\rho^-(770)$ and $\rho^0(770)$. All other contributions including non-resonant ones are neglected for simplicity. We can then write [20]:

$$\mathcal{A}_{3\pi} = f_+ A^{+-} + f_- A^{-+} + f_0 A^{00}, \quad (1.35)$$

$$\bar{\mathcal{A}}_{3\pi} = f_+ \bar{A}^{+-} + f_- \bar{A}^{-+} + f_0 \bar{A}^{00}, \quad (1.36)$$

where the f_i are functions defined in equation (C.12), incorporating the kinematic and dynamical properties of the B^0 decay via vector resonances⁵. The amplitudes with tree and penguin contributions are defined in Eq. (1.27). Due to SU(2) flavor

⁵Note that neglecting the mass difference between the final state pions, and using Eq. (1.27) and

symmetry (penguins are $\Delta I = 1/2$ transitions only), and neglecting SU(2)-breaking electro-weak penguins, we can use the relation [19]

$$P^{00} = -\frac{1}{2} (P^{+-} + P^{-+}) . \quad (1.37)$$

Assuming CP violation in $B^0\bar{B}^0$ mixing is absent ($|q/p| = 1$), and assuming $\Delta\Gamma_{B_d} = 0$ as well as CPT invariance, the time-dependent decay rate is given by

$$|\mathcal{A}_{3\pi}^{\pm}(\Delta t)|^2 = \frac{e^{-|\Delta t|/\tau_{B^0}}}{4\tau_{B^0}} \left[|\mathcal{A}_{3\pi}|^2 + |\bar{\mathcal{A}}_{3\pi}|^2 \mp (|\mathcal{A}_{3\pi}|^2 - |\bar{\mathcal{A}}_{3\pi}|^2) \cos(\Delta m_d \Delta t) \right. \\ \left. \pm 2\text{Im} [\bar{\mathcal{A}}_{3\pi} \mathcal{A}_{3\pi}^*] \sin(\Delta m_d \Delta t) \right] \quad (1.38)$$

Inserting the amplitudes (1.35) and (1.36), one obtains for the terms in Eq. (1.38)

$$|\mathcal{A}_{3\pi}|^2 \pm |\bar{\mathcal{A}}_{3\pi}|^2 = \sum_{\kappa \in \{+, -, 0\}} |f_{\kappa}|^2 U_{\kappa}^{\pm} + 2 \sum_{\kappa < \sigma \in \{+, -, 0\}} \left(\text{Re} [f_{\kappa} f_{\sigma}^*] U_{\kappa\sigma}^{\pm, \text{Re}} - \text{Im} [f_{\kappa} f_{\sigma}^*] U_{\kappa\sigma}^{\pm, \text{Im}} \right) , \\ \text{Im} (\bar{\mathcal{A}}_{3\pi} \mathcal{A}_{3\pi}^*) = \sum_{\kappa \in \{+, -, 0\}} |f_{\kappa}|^2 I_{\kappa} + \sum_{\kappa < \sigma \in \{+, -, 0\}} \left(\text{Re} [f_{\kappa} f_{\sigma}^*] I_{\kappa\sigma}^{\text{Im}} + \text{Im} [f_{\kappa} f_{\sigma}^*] I_{\kappa\sigma}^{\text{Re}} \right) , \quad (1.39)$$

(C.17), leads to the following symmetric form of Eq. (1.35)

$$\mathcal{A}_{3\pi} = (s_{-0} - s_{+-}) {}^1F_{\rho^+}(s_{+0}) A^{+-} + (s_{+-} - s_{+0}) {}^1F_{\rho^-}(s_{-0}) A^{-+} + (s_{+0} - s_{-0}) {}^1F_{\rho^0}(s_{+-}) A^{00} .$$

with

$$U_{\kappa}^{\pm} = |A^{\kappa}|^2 \pm |\bar{A}^{\kappa}|^2, \quad (1.40)$$

$$U_{\kappa\sigma}^{\pm, \text{Re(Im)}} = \text{Re(Im)} [A^{\kappa} A^{\sigma*} \pm \bar{A}^{\kappa} \bar{A}^{\sigma*}] , \quad (1.41)$$

$$I_{\kappa} = \text{Im} [\bar{A}^{\kappa} A^{\kappa*}] , \quad (1.42)$$

$$I_{\kappa\sigma}^{\text{Re}} = \text{Re} [\bar{A}^{\kappa} A^{\sigma*} - \bar{A}^{\sigma} A^{\kappa*}] , \quad (1.43)$$

$$I_{\kappa\sigma}^{\text{Im}} = \text{Im} [\bar{A}^{\kappa} A^{\sigma*} + \bar{A}^{\sigma} A^{\kappa*}] , \quad (1.44)$$

where we used the short-hand notation $A^+ \equiv A^{+-}$, $A^- \equiv A^{-+}$ and $A^0 \equiv A^{00}$, respectively. Eqs. (1.40-1.44) correspond to 27 interdependent observables representing 11 unknowns. Removing the arbitrary global phase reduces to 10 the minimum number of unknowns that are determined by the fit. A few observations can be made:

- the occurrence of $\sin(2\alpha)$ and $\cos(2\alpha)$ terms in the observables provides the resolution of the eight-fold ambiguity on α obtained in the quasi-two-body analysis in the absence of penguin contributions; the resolution is however not complete, since the replacements $\alpha \rightarrow \pi/2 - \alpha$ and $\alpha \rightarrow -\pi + \alpha$ lead to identical results;
- the $\alpha \rightarrow \pi/2 - \alpha$ ambiguity can be resolved either if the phase difference $\delta_T^{\kappa} - \bar{\delta}_T^{\kappa}$ is non-zero, and/or if penguin contributions are present;
- penguins lead to terms proportional to $\sin(\alpha)$ and $\cos(\alpha)$, which resolve both $\alpha \rightarrow \pi/2 - \alpha$ and $\alpha \rightarrow -\pi + \alpha$ ambiguities.

Interference Pattern

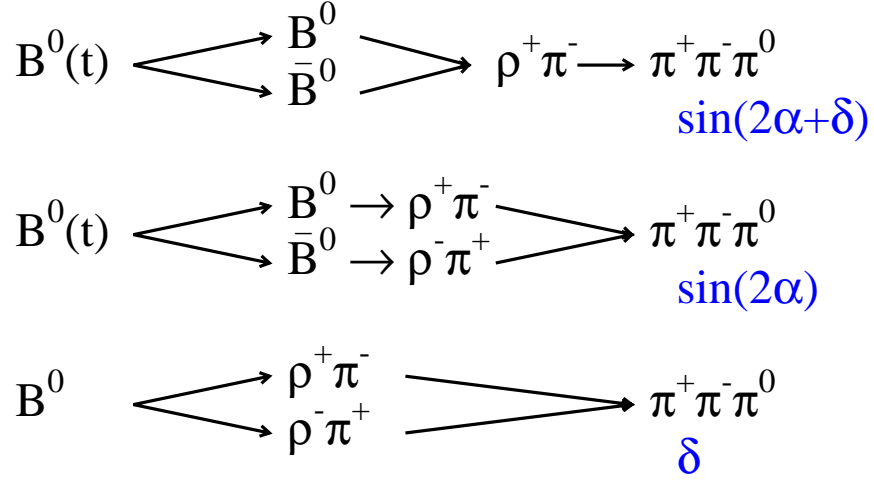


Figure 1.5: A representation of interference terms in $B^0 \rightarrow \rho^\pm \pi^\mp$.

The master equation (1.38) is said to lead to sufficient observables to determine the 10 fit unknowns. Figure 1.5 shows the origin of the most important phase dependence in the system. More specifically, equation (1.38) gives rise to four categories of terms:

1. $|\mathbf{f}_\kappa|^2 U_\kappa^\pm$: in absence of penguin amplitudes, these squares are independent of the weak and strong phases. They are similar to the Q2B cosine coefficients describing direct CPV.
2. $|\mathbf{f}_\kappa|^2 \mathbf{I}_\kappa$: these terms are entirely due to $B^0 \bar{B}^0$ oscillation and are similar to the Q2B sine coefficient describing mixing-induced CPV.
3. $\text{Re} [\mathbf{f}_\kappa \mathbf{f}_\sigma^*] U_{\kappa\sigma}^{\pm, \text{Re}}$ and $\text{Im} [\mathbf{f}_\kappa \mathbf{f}_\sigma^*] \mathbf{I}_{\kappa\sigma}^{\text{Re}}$: the real parts of the amplitude bilinears

are due to the interference between the ρ bands and not due to $B^0\bar{B}^0$ oscillation. In the absence of penguin amplitudes, they have no information on α , but measure the relative phase between the tree amplitudes.

4. $\text{Im} [f_\kappa f_\sigma^*] U_{\kappa\sigma}^{\pm, \text{Im}}$ and $\text{Re} [f_\kappa f_\sigma^*] I_{\kappa\sigma}^{\text{Im}}$: these terms arise from interference between $B^0\bar{B}^0$ oscillation and different ρ bands.

The Nominal Signal Model

Parameter	$\tau^+ \rightarrow \bar{\nu}_\tau(\rho^+ \rightarrow)\pi^+\pi^0$	$e^+e^- \rightarrow (\rho^0 \rightarrow)\pi^+\pi^-$
$m_{\rho(770)}$	775.5 ± 0.6	773.1 ± 0.5
$\Gamma_{\rho(770)}$	148.2 ± 0.8	148.0 ± 0.9
$a_{\rho\omega}$	$\equiv 0$	0.0020 ± 0.0001
$\phi_{\rho\omega}$	$\equiv 0$	13.0 ± 2.3
$m_{\rho(1450)}$		1409 ± 12
$\Gamma_{\rho(1450)}$		500 ± 37
$a_{\rho'}$		0.166 ± 0.005
$\phi_{\rho'}$		177.8 ± 5.2
$m_{\rho(1700)}$		1749 ± 20
$\Gamma_{\rho(1700)}$		$\equiv 235$
$a_{\rho''}$		0.071 ± 0.006
$\phi_{\rho''}$		$\equiv 0$

Table 1.1: *Result of the charged and neutral Gounaris-Sakurai model (C.27, C.37) fit to form factor data from τ decays (second column) and e^+e^- annihilation (third column). For the parameters belonging to both columns we assume that isospin invariance holds exactly. The parameters are used in the nominal form factor parameterization of the dominant charged and neutral amplitudes of the signal model. Note that some of these parameters exhibit strong correlations among each other so that only the entire set is well defined. The relative amplitude fractions $a_{\rho^{(\prime\prime)}}$ given here are defined according to Ref. [45] with a $m_{\rho^{(\prime\prime)}}^2$ in the nominator.*

Details of the resonance description are given in Appendix C. The nominal

signal model implemented in the DP fit is given below. Variations to this model will be considered as systematic uncertainties.

- The various amplitudes are summed coherently according to Eq. (C.10).
- For the charged Dalitz bands, only the three ρ resonances of Eq. (C.37) are considered in the nominal signal model. We make the assumption that the relative phases between the charged *rho* resonances are CP -conserving.
- For the neutral Dalitz band, we consider the ρ resonances of Eq. (C.37). We do not take into account $\rho(770) \leftrightarrow \omega(782)$ mixing, and the established isoscalar resonances $f_0(980)$, $f_0(1370)$ and $f_2(1270)$ because they are expected to be small.
- We use results from e^-e^- annihilation and τ decays to fix the masses and widths of the neutral and charged $\rho(X)$ resonances, respectively. The fits are performed with the GS parameterization (C.27) and the results are given in Table 1.1 and are plotted in Fig. C.4. Perfect agreement between data and the model is observed. Note also that these parameters are strongly correlated among each other so that only the entire set is well defined. As an example, reducing the $\rho(770)$ mass can be covered by a simultaneous reduction of the $\rho(1450)$ mass, or an increase of its relative amplitude. Variations of parameters for the purpose of systematic studies must be performed coherently.
- Sub-dominant contributions as those discussed in Section C.3.4 are not part of the nominal signal model. Also neglected is a possible contribution from the

$\rho_3(1690)$ resonance to both, the charged and neutral form factors. It is broad and almost degenerate with the $\rho(1700)$ and decays in $(23.6 \pm 1.3)\%$ of the cases into a $\pi\pi$ final state. Since it is spin three, its helicity distribution will differ from the one of the other ρ resonances. The influence of these modes on the results will be studied for systematics.

- Long-living modes with the same final states, like $B^0 \rightarrow D^-(\rightarrow \pi^-\pi^0)\pi^+$, $B^0 \rightarrow \bar{D}^0(\rightarrow \pi^+\pi^-)\pi^0$ or $B^0 \rightarrow K_s^0(\rightarrow \pi^+\pi^-)\pi^0$ are treated part of the B background model since they do not interfere with the strongly decaying signal resonances.

Chapter 2

PEP-II B Factory and *BABAR* Detector

The primary goal of the *BABAR* experiment is the systematic study of CP asymmetries in the decays of B mesons. To observe the time-dependent CP asymmetries in B^0 decay, three things need to be measured: the exclusive final state needs to be fully reconstructed; the flavor of the decaying particle needs to be tagged; and the proper time of the B^0 decay with respect to its production needs to be measured, as the asymmetry in most cases cancels to zero in time-integrated measurements of e^+e^- machines. The *BABAR* experiment is designed and optimized to achieve the goals specified above. The PEP-II B Factory is designed to deliver the B mesons to the experiment.

Figure 2.1 shows a longitudinal section of the detector center. The inner detector consists of a silicon vertex tracker, a drift chamber, a ring-imaging Cherenkov detector, and a CsI calorimeter. These detector systems are surrounded by a superconducting solenoid that is designed for a magnetic field of 1.5T. The steel flux return is instrumented for muon and neutral hadron detection.

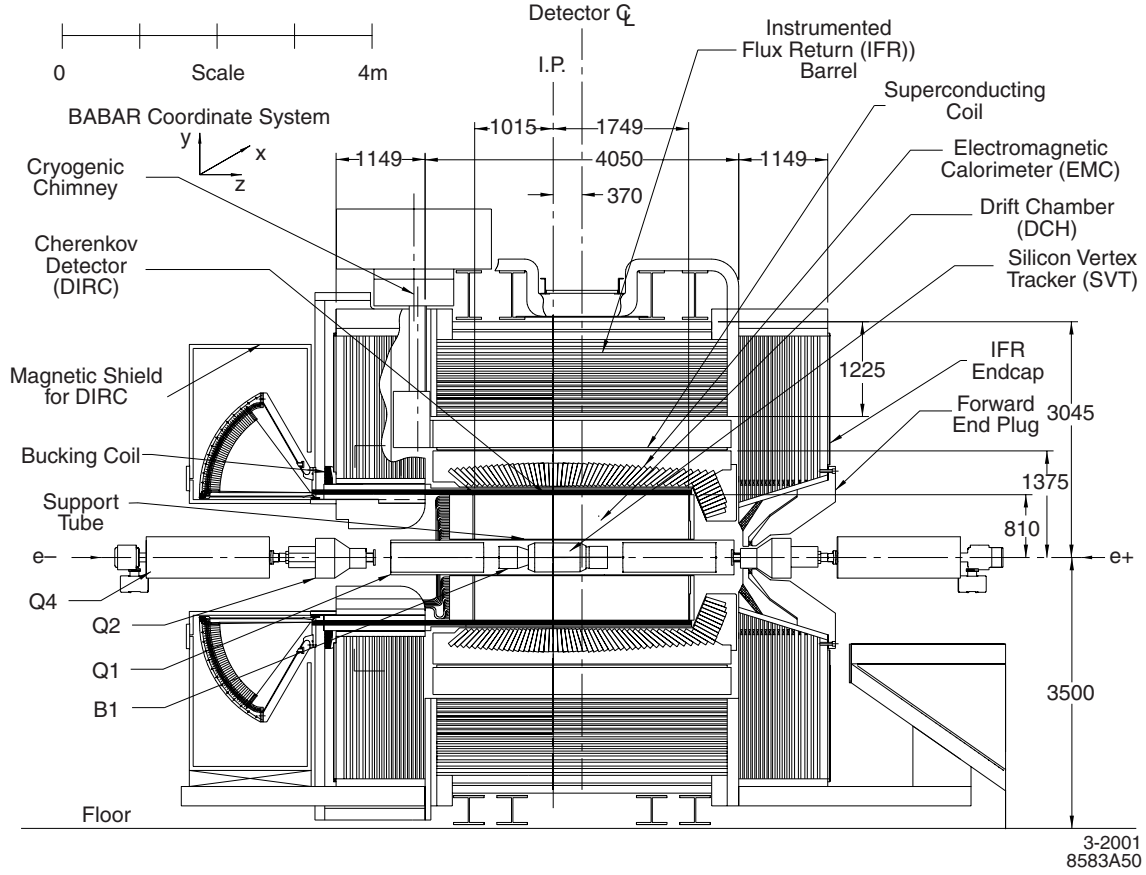


Figure 2.1: *BABAR* detector longitudinal cross section.

2.1 PEP-II Asymmetric B Factory

PEP-II is an e^+e^- storage ring system designed to operate at a center of mass energy of 10.58 GeV, corresponding to the mass of the $\Upsilon(4S)$ resonance. The parameters of these energy asymmetric storage rings are presented at Table 2.1.

The bunches collide head-on and are separated magnetically in the horizontal plane by a pair of dipole magnets (B1), followed by a series of offset quadrupoles, as shown in figure 2.1. The tapered B1 dipoles, located at ± 21 cm on either side of the interaction point (IP), and the Q1 quadrupoles are permanent magnets made of

Parameters	Design	Typical
Energy HER/LER(GeV)	9.0/3.1	9.0/3.1
Current HER/LER(A)	0.75/2.15	0.7/1.3
Number of bunches	1658	553-829
Bunch spacing(ns)	4.2	6.3-10.5
σ_x (μm)	110	120
σ_y (μm)	3.3	5.6
σ_z (mm)	9	9
Luminosity($10^{33} \text{ cm}^{-2} \text{ s}^{-1}$)	3	6
Luminosity(pb^{-1}/d)	135	500

Table 2.1: *PEP-II beam parameters*

samarium-cobalt placed inside the field of the *BABAR* solenoid, while the Q2, Q4 and Q5 quadrupoles, located outside or in the fringe field of the solenoid, are standard iron magnets. The collision axis is off-set from the z -axis of the *BABAR* detector by about 20 mrad in the horizontal plane to minimize the perturbation of the beams by the solenoidal field.

The interaction region is enclosed by a water-cooled beam pipe of 27.9 mm outer radius, composed of two layers of beryllium (0.83 and 0.53 mm thick) with a 1.48 mm water channel between them. To attenuate synchrotron radiation, the inner surface of the pipe is coated with a 4 μm thin layer of gold. In addition, the beam pipe is wrapped with 150 μm of tantalum foil on either side of the IP, beyond $z = +10.1 \text{ cm}$ and $z = -7.9 \text{ cm}$. The total thickness of the central beam pipe section at normal incidence corresponds to 1.06% of a radiation length. The beam pipe, the permanent magnets, and the SVT were assembled and aligned, and then enclosed in a 4.5 m-long support tube which spans the IP. The central section of this tube is fabricated from a

The SVT is designed to provide precision reconstruction of charged particle trajectories and decay vertices near the interaction region. As shown in figure 2.2 and figure 2.3, the *BABAR* silicon vertex tracker consists of five concentric cylindrical layers of double-sided silicon detectors. Each layer is divided in azimuth into modules. The inner three layers have six detector modules and are a traditional-barrel-style structure. The outer two consist respectively of 16 and 18 detector modules, and employ a new arch structure in which the detectors are electrically connected across an angle. The bend in the arch modules increases the solid angle coverage and avoids very large track incidence angles.

The inner sides of the detectors have strips (z strips) oriented perpendicular

to the beam direction to measure the z coordinate, whereas the outer sides, with longitudinal strips (ϕ strips), allow the ϕ coordinate measurement.

The inner modules are tilted in ϕ by 5° , allowing an overlap region between adjacent modules, a feature that provides full azimuthal coverage and is advantageous for alignment. The outer modules cannot be tilted, because of the arch geometry. To avoid gaps and to have a suitable overlap in the ϕ coordinate, layers 4 and 5 are divided into two sub-layers and placed at slightly different radii (see figure 2.3).

The total active silicon area is 0.96 m^2 and the material traversed by particles is $\sim 4\%$ of a radiation length. The geometrical acceptance of SVT is 90% of the solid angle in the center of mass system.

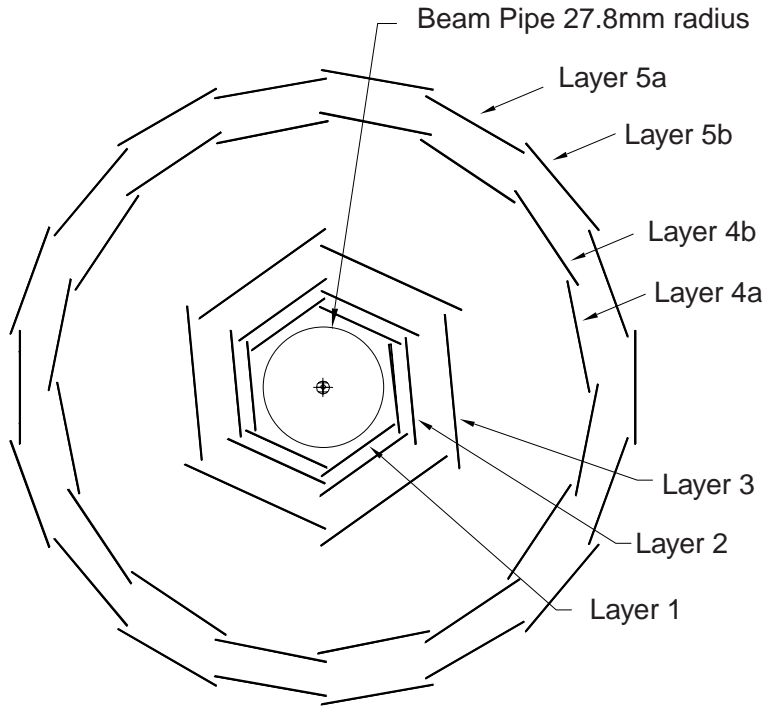


Figure 2.3: *Schematic view of SVT: transverse section.*

2.3 Drift Chamber

The principal purpose of the drift chamber (DCH) is the efficient detection of charged particles and the measurement of their momenta and angles with high precision. The reconstruction of decay and interaction vertices outside of the SVT volume, for example the K_s^0 decays, relies solely on the DCH. At low momenta, the DCH is required to provide particle identification by measurement of ionization loss, dE/dx . A resolution of about 7% allows π/K separation up to 700 MeV/ c .

The *BABAR* DCH is relatively small in diameter, but almost 3 m long, with 40 layers of small hexagonal cells providing up to 40 spatial and ionization loss measurements for charged particles with transverse momentum greater than 180 MeV/ c . Longitudinal position information is obtained by placing the wires in 24 of the 40 layers at small angles with respect to the z -axis. The chosen gas is a 80:20 mixture of helium:isobutane. This mixture has a radiation length that is five times larger than commonly used argon-based gases. The smaller Lorentz angle results in a rather uniform time-distance relationship and thereby improved spatial resolution.

A longitudinal cross-section and dimensions of the DCH are shown in figure 2.4. The DCH is bounded radially by the support tube at its inner radius and the DIRC at its outer radius. The device is asymmetrically located with respect to the IP. The forward length of 1749 mm is chosen so that particles emitted at polar angle of 17.2° traverse at least half of the layers of the chamber before exiting the front endplate. In the backward direction, the length of 1015 mm means that particles with polar angles

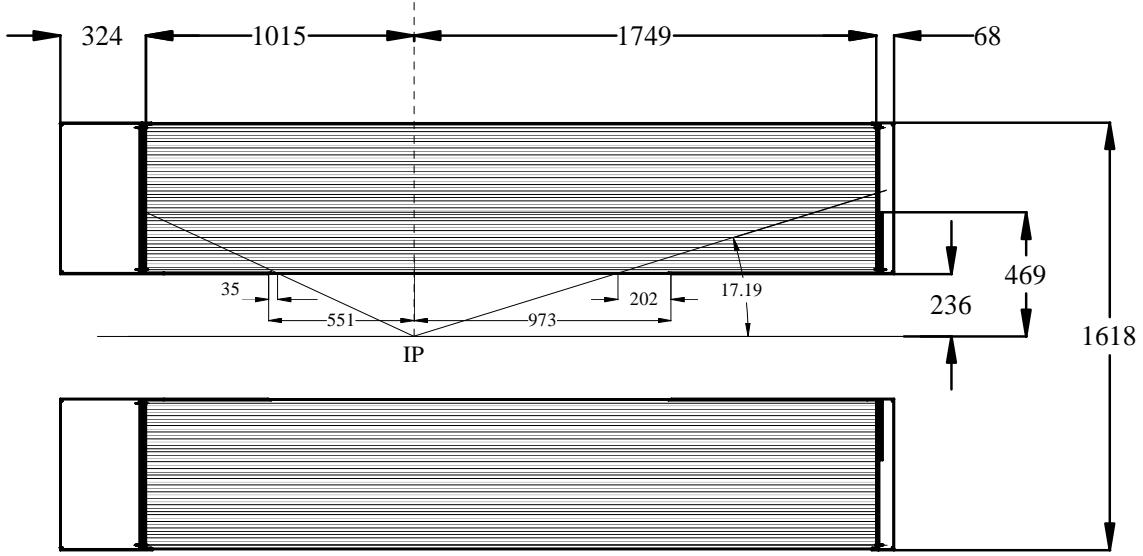
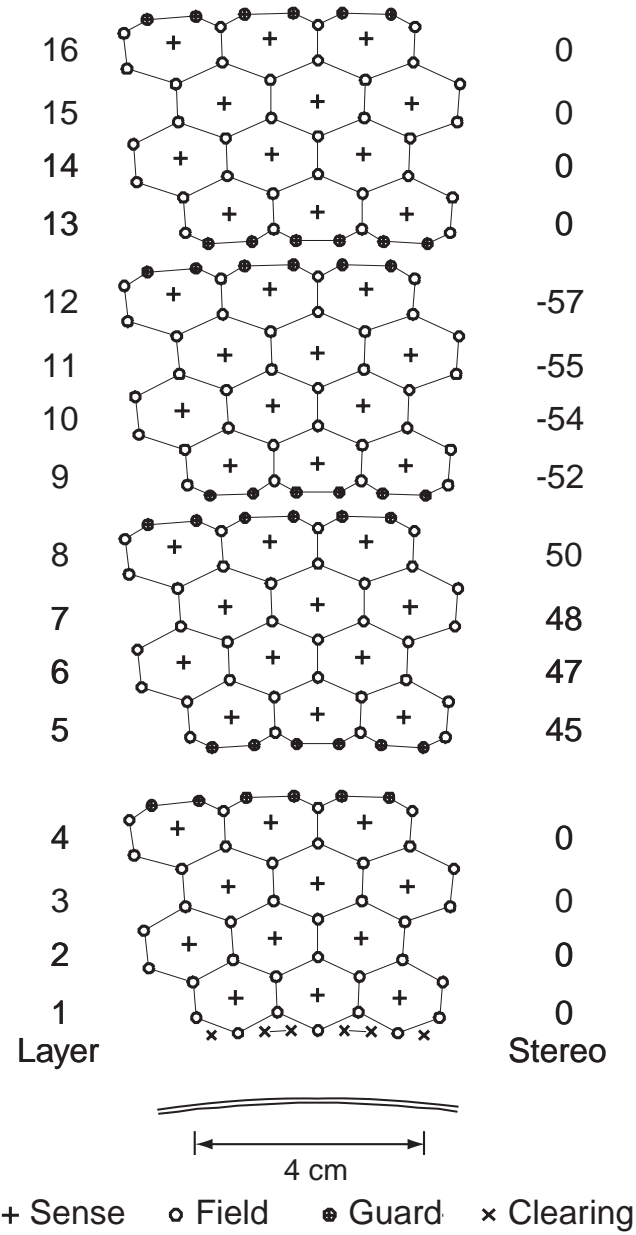


Figure 2.4: *Longitudinal section of the DCH with principal dimensions; the chamber center is offset by 370 mm from the interaction point.*

down to 152.6° traverse at least half of the layers.

The DCH consists of a total of 7104 small drift cells, arranged in 40 cylindrical layers. The layers are grouped by four into ten superlayers, with the same wire orientation and equal numbers of cells in each layer of a superlayer. Sequential layers are staggered by half a cell. This arrangement enables local segment finding and left-right ambiguity resolution within a superlayer, even if one out of four signals is missing. The stereo angles of the superlayers alternate between axial (A) and stereo (U,V) pairs, in the order AUVAUVAUVA, as shown in figure 2.5. The stereo angles vary between ± 45 and ± 76 mrad; they have been chosen such that the drilling patterns are identical for the two endplates.

The drift cells are hexagonal in shape. Each cell consists of one sense wire surrounded by six field wires, as shown in figure 2.5. While the field wires are at



1-2001
8583A14

Figure 2.5: Schematic layout of drift cells for the four innermost superlayers. Lines have been added between field wires to aid in visualization of the cell boundaries. The numbers on the right side give the stereo angle of sense wires in each layer. The 1 mm-thick beryllium inner wall is shown inside of the first layer.

ground potential, a positive high voltage is applied to the sense wires. An avalanche gain of approximately 5×10^4 is obtained at a typical operating voltage of 1960V and a 80:20 helium-isobutane gas mixture.

2.4 Detector of Internally Reflected Cherenkov Light

BABAR uses a new kind of ring-imaging Cherenkov detector called DIRC to achieve particle identification in a wide momentum range, in a small radial dimension and with high tolerance of background.

The DIRC is based on the principle that the magnitudes of angles are maintained upon reflection from a flat surface. Figure 2.6 shows a schematic of the DIRC geometry, which illustrates the principles of light production, transport and imaging. The radiator material of the DIRC is synthetic, fused silica in the form of long, thin bars with rectangular cross-sections. These bars serve both as radiators and as light pipes for the portion of the light trapped in the radiator by total internal reflection.

For the particles with $\beta \approx 1$, some photons will always lie within the total internal reflection limit, and will be transported to either one or both ends of the bar, depending on the particle incident angle. To avoid instrumenting both ends of the bar with photon detectors, a mirror is placed at the forward end, perpendicular to the bar axis, to reflect incident photons to the backward, instrumented end. Once photons arrive at the instrumented end, most of them emerge into a water-filled expansion region, called *standoff box*. A fused silica *wedge* at the exit of the bar reflects photons at large angles relative to the bar axis. It thereby reduces the size of the required

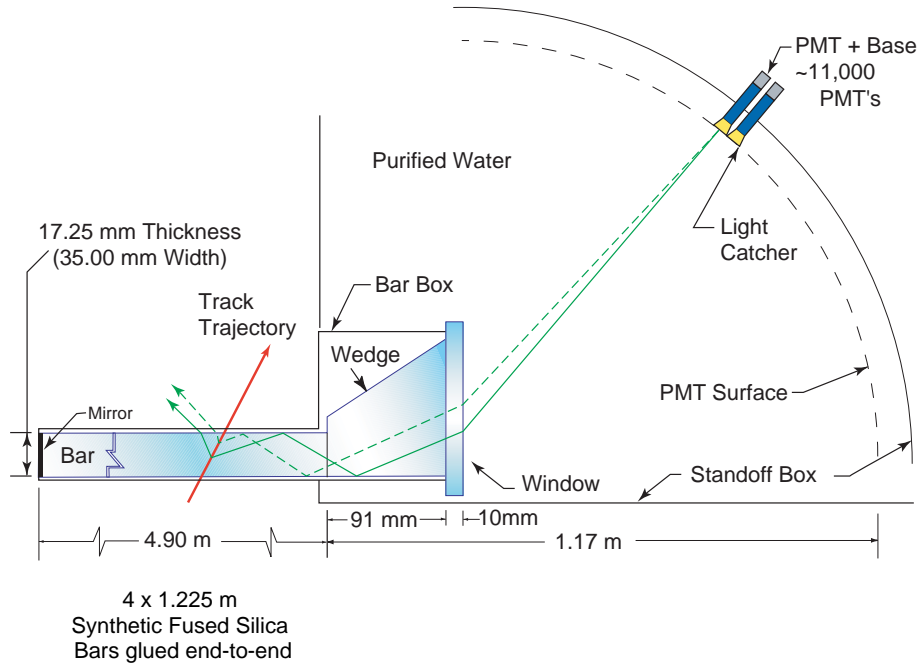


Figure 2.6: *Schematics of the DIRC fused silica radiator bar and imaging region.*

detection surface and recovers those photons that would otherwise be lost due to internal reflection at the fused silica water interface. The photons are detected by an array of densely packed photomultiplier tubes (PMTs), each surrounded by reflecting *light catcher* cones to capture light which would otherwise miss the active area of the PMT. The PMTs are placed at a distance of about 1.2 m from the bar end.

The DIRC bars are arranged in a 12-sided polygonal barrel. Because of the beam energy asymmetry, particles are produced preferentially forward in the detector. The principal components of the DIRC are shown schematically in figure 2.7. The bars are placed into 12 hermetically sealed containers, called *bar boxes*, made of very thin aluminum-hexcel panels. Each bar box contains 12 bars, for a total of 144 bars. Within a bar box the 12 bars are optically isolated by a $\sim 150 \mu\text{m}$ air gap between

neighboring bars, enforced by custom shims made from aluminum foil.

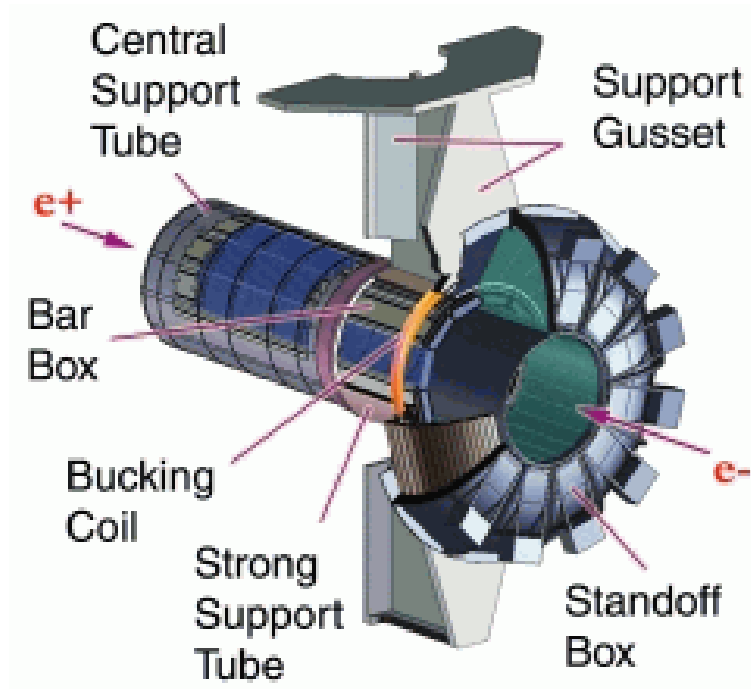


Figure 2.7: *Exploded view of the DIRC mechanical support structure.*

The bars are 17- mm-thick, 35- mm-wide, and 4.9- m-long. Each bar is assembled from four 1.225 m pieces that are glued end-to-end. Each bar has a fused silica wedge glued to it at the readout end. The wedge, which is made of the same material as the bar, is 91- mm-long with very nearly the same width as the bars and a trapezoidal profile. The 12 wedges in a bar box are glued to a common 10- mm-thick fused silica window, that provides the interface and seal to the purified water in the standoff box.

The standoff box is made of stainless steel, and consists of a cone, cylinder and 12 sectors of PMTs. It contains about 6000 liters of purified water. A steel shield, supplemented by a *bucking coil*, surrounds the standoff box to reduce the field in the PMT region to below 1T. The PMTs at the rear of the standoff box lie on a surface

that is approximately toroidal. Each of the 12 PMT sectors contains 896 PMTs with 29-mm-diameter, in a closely packed array inside the water volume.

2.5 Electromagnetic Calorimeter

The electromagnetic calorimeter (EMC) is designed to measure electromagnetic showers with excellent efficiency, and energy and angular resolution over the energy range from 20 MeV to 9 GeV. The *BABAR* EMC is a hermetic, total-absorption calorimeter, composed of a finely segmented array of thallium-doped cesium iodide crystals. The crystals are read out with silicon photodiodes that are matched to the spectrum of scintillation light.

Figure 2.8 shows a longitudinal cross section of the EMC. The EMC consists of a cylindrical barrel and a conical forward endcap. It has full coverage in azimuth and extends in polar angle from 15.8° to 141.8° corresponding to a solid-angle coverage of 90% in the center of mass system. The barrel contains 5760 crystals arranged in 48 distinct rings with 120 identical crystals each. The endcap holds 820 crystals arranged in eight rings. These crystals have a tapered trapezoidal cross section. The length of the crystals increases from 29.6 cm in the backward to 32.4 cm in the forward direction to limit the effects of shower leakage from increasingly higher energy particles.

The crystals are made of the thallium-doped CsI. The high light yield and small Moliere radius allow for excellent energy and angular resolution, while the short radiation length allows for shower containment at *BABAR* energies with relatively compact design. Furthermore, the high light yield and the emission spectrum permit efficient

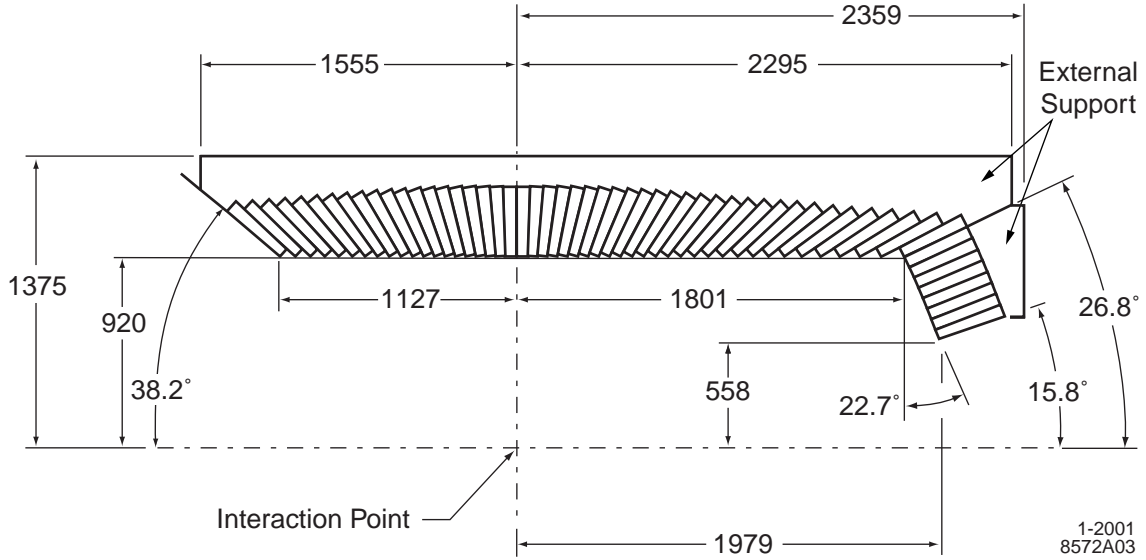


Figure 2.8: A longitudinal cross section of the EMC (only the top half is shown) indicating the arrangement of the 56 crystal rings. The detector is axially symmetric around the z -axis. All dimensions are given in mm.

use of silicon photodiodes which operate well in high magnetic fields. The transverse size of the crystals is chosen to be comparable to the Moliere radius achieving the required angular resolution at low energies while appropriately limiting the total number of crystals.

The photon detector consists of two $2 \times 1 \text{ cm}^2$ silicon PIN diodes glued to a transparent 1.2-mm-thick polystyrene substrate that, in turn, is glued to the center of the rear face of the crystal by an optical epoxy to maximize light transmission. The surrounding area of the crystal face is covered by a plastic plate coated with white reflective paint. The plate has two 3-mm-diameter penetrations for the fibers of the light pulser monitoring system. Each of the diodes is directly connected to a low-noise preamplifier. The entire assembly is enclosed by an aluminum fixture. This fixture is

electrically coupled to the aluminum foil wrapped around the crystal and thermally coupled to the support frame to dissipate the heat load from the preamplifiers.

2.6 Instrumental Flux Return

The Instrumented Flux Return (IFR) is designed to identify muons with high efficiency and good purity, and to detect neutral hadrons over a wide range of momenta and angles. The IFR uses the steel flux return of the magnet as a muon filter and hadron absorber. Single gap resistive plate chambers (RPCs) with two coordinate readout have been chosen as detectors. The RPCs are installed in the gaps of the finely segmented steel of the barrel and the end doors of the flux return, as illustrated in Figure 2.9. The steel is segmented into 18 plates, increasing in thickness from 2 cm for the inner nine plates to 10 cm for the outermost plates. The nominal gap between the steel plates is 3.5 cm in the inner layers of the barrel and 3.2 cm elsewhere. There are 19 PRC layers in the barrel and 18 in the endcaps. In addition, two layers of cylindrical RPCs are installed between the EMC and the magnet cryostat to detect particles exiting the EMC.

RPCs detect streamers from ionizing particles via capacitive readout strips. They offer several advantages: simple, low cost construction and the possibility of covering odd shapes with minimal dead space. Further benefits are large signals and fast response allowing for simple and robust front-end electronics and good time resolution, typically 1-2 ns. The position resolution depends on the segmentation of the readout; a value of a few mm is achievable.

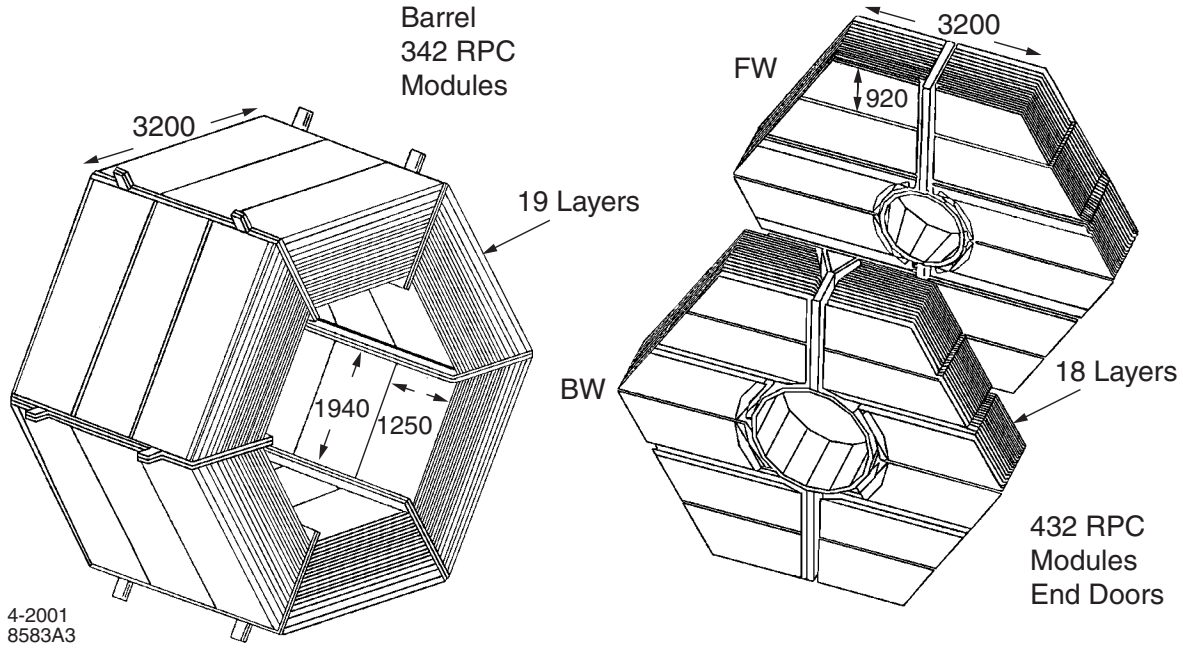


Figure 2.9: Overview of the IFR: Barrel sectors and forward and backward end doors; the shape of the PRC modules and their dimensions are indicated.

The IFR detectors cover a total active area of about 2000 m^2 . There are a total of 806 PRC modules, 57 in each of the six barrel sectors, 108 in each of the four half end doors, and 32 in the two cylindrical layers. The size and shape of the modules are matched to the steel dimensions with very little dead space. More than 25 different shapes and sizes were built. Because the size of a module is limited by the maximum size of the material available, two or three PRC modules are joined to form a gap-size chamber. The modules of each chamber are connected to the gas system in series, while the high voltage is supplied separately to each module.

2.7 Trigger

The basic requirement for the trigger system is the selection of events of interest with a high, stable, and well-understood efficiency while rejecting background events and keeping the total event rate under 120Hz. At design luminosity, beam-induced background rates are typically about 20kHz each for one or more tracks in the drift chamber with $p_t > 120 \text{ MeV}/c$ or at least one EMC cluster with $E > 100 \text{ MeV}$. The rates for the principal physics processes are typically much lower than that at a few hertz level. The total trigger efficiency is required to exceed 99% for all $B\bar{B}$ events and at least 95% for continuum events. It must also be able to operate in an environment with dead or noisy electronics channels. The trigger should contribute no more than 1% to dead time.

The trigger is implemented as a two-level hierarchy, the Level 1 (L1) in hardware followed by the Level 3 (L3) in software. During normal operation, the L1 is configured to have an output rate of typically 1kHz. Triggers are produced within a fixed latency window of 11-12 μs after the e^+e^- collision and delivered to the *Fast Control and Timing system* (FCTS). The L3 receives the output from L1, performs a second stage rate reduction for the main physics sources, and identifies and flags the special categories of events needed for luminosity determination, diagnostic and calibration purposes. At design luminosity, the L3 filter acceptance for physics is $\sim 90\text{Hz}$, while $\sim 30\text{Hz}$ contain the other special event categories.

The L1 trigger decision is based on the presence of charged tracks in the DCH

above a preset transverse momentum, showers in the EMC, and tracks detected in the IFR. The trigger data are processed by three specialized hardware processors. The *drift chamber trigger* (DCT) and *electromagnetic trigger* (EMT) both satisfy all trigger requirements independently with high efficiency, and thereby provide a high degree of redundancy, which enables the measurement of trigger efficiency. The *instrumented flux return trigger* (IFT) is used for triggering $\mu^+\mu^-$ and cosmic rays, mostly for diagnostic purposes.

The L3 trigger software comprises event reconstruction and classification, a set of event selection filters, and monitoring. The filters have access to the complete event data for making their decision, including the output of the L1 trigger processors and FCTS trigger scalars. L3 operates by refining and augmenting the selection methods used in L1. The L3 trigger has three phases. In the first phase, events are classified by defining L3 input lines, which are based on a logical OR or of any number of the 32 FCTS output lines. Any number of L3 input lines may be defined. The second phase comprises a number of *scripts*. Each script executes if its single L3 input line is true and subsequently produces a single pass-fail output flag. Internally, a script may execute one or both of the DCH and EMC algorithms, followed by one or more filters. The algorithms construct quantities of interest, while the filters determine whether or not those quantities satisfy the specific selection criteria. In the final phase, the L3 output lines are formed. Each output line is defined as the logical OR of selected script flags.

Chapter 3

Analysis Overview

3.1 Signature of the Charmless Three-body B Decay

B mesons decay dominantly through the Cabbibo favored $b \rightarrow c$ transition. Therefore, the charmless B decay, which involves $b \rightarrow u$ transition, is naturally suppressed by the $|V_{ub}/V_{cb}|^2$. The typical branching fraction of charmless three-body B -decays is at the order of 10^{-6} . Notice that the cross section for light quark productions $e^+e^- \rightarrow q\bar{q}(\text{continuum})$ is of the same order as the $b\bar{b}$ cross section at the $\Upsilon(4S)$ resonance. As a result, the continuum background ought to be suppressed by roughly a factor of 10^6 in order to study charmless B decays. To achieve this goal, one often exploits both B decay kinematics and event shape difference in different decays.

3.1.1 Decay Kinametics

The most commonly used kinematic variables to separate B decay from continuum production are:

- $m_{\text{ES}} \equiv \sqrt{E_c^2 - P_B^2}$, where $E_c = (s + 2P_{\Upsilon(4S)} \cdot P_B)/(2E_{\Upsilon(4S)})$, and $s = E_{CM}^2$.

- $\Delta E \equiv E_B^* - E_{CM}/2$, where E_B^* is the energy of the reconstructed B meson evaluated in the center of mass frame.

The variable m_{ES} is the beam-energy-substituted-mass. The typical resolution of m_{ES} for fully reconstructed B decay is about 2.5 MeV and is limited by our knowledge of the e^+e^- beam energy and direction. The distribution of m_{ES} for continuum background is parametrized empirically by the ARGUS function [23] which simply shows the phase space behavior. The variable ΔE is the difference between the energy of the fully reconstructed B meson and the expected energy of the B meson, both evaluated in the center-of-mass frame. The resolution of ΔE varies dramatically from mode to mode, depending on how many particles in the final states as well as the type of particles. Normally, the ΔE resolution is much worse if there is one or multiple π^0 s in the final state compared with final states involving only charged tracks. The distribution of ΔE for continuum background is commonly described by low order polynomials. The distributions of m_{ES} and ΔE for some typical processes are shown in Figure 3.1.

Some other kinematic variables related to B decays include $\cos\theta_{B,z}$, which is the cosine of the angle between B momentum z-axis and $\cos\theta_{T_B,z}$, which is the cosine of the angle between B thrust and the z-axis, both evaluated in the center of mass frame.

3.1.2 Decay Topology

Event shape variables further exploit the topological difference between B decay and the light quark decays. The spinless B mesons are produced with little momentum in the $\Upsilon(4S)$ frame, thus the decay is rather isotropic. It is schematically shown in

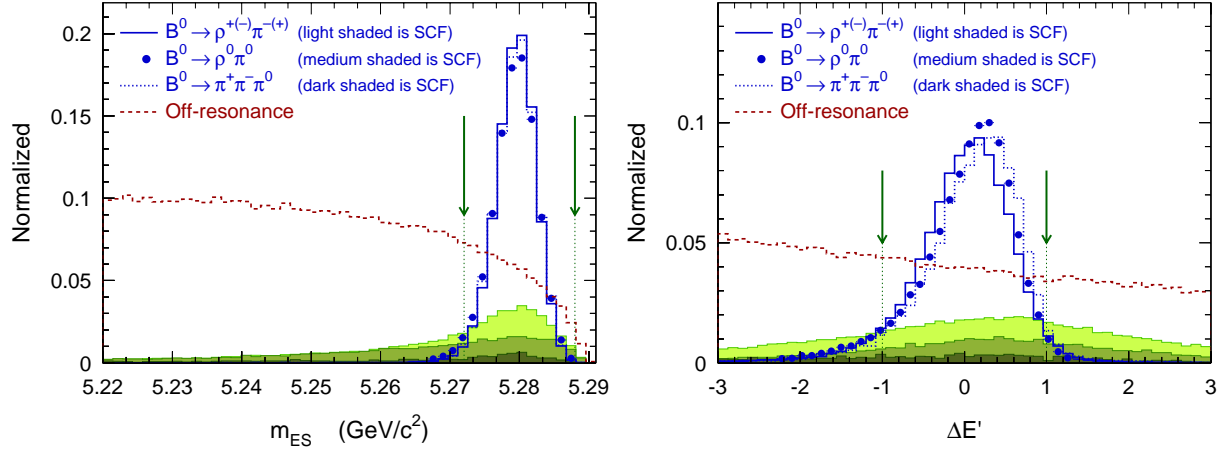


Figure 3.1: Distributions of m_{ES} (left plot) and a normalized ΔE (right plot) for truth-matched (solid) and misreconstructed $\rho(\pi\pi)\pi$ events (shaded), and for off-resonance data (dashed). The arrows indicate the cuts applied in the Dalitz plot analysis.

Figure 3.2. On the contrary, the light quark pairs are produced with a large boost. The decay products are formed by fragmentation and it has a jet-like topology. Additionally, the correlation between the direction of the signal B decay and the *rest-of-event* (ROE) is very powerful to separate B decays from continuum events for the same reason. The commonly used topological variables are:

- The *monomials* L_n , a set of momentum-weighted sums over the ROE tracks with respect to the B thrust axis T_B , are defined as:

$$L_n \equiv \sum_{i=\text{ROE}} p_i \times |\cos(\theta_{T_B,i})|^n \quad (3.1)$$

Typically, several monomials are used in the analysis simultaneously. It's a common practice to combine topological variables as well as other kinematic variables into one *Multivariate Analyzer* (MVA), such as a Neural Network, to best separate signal from

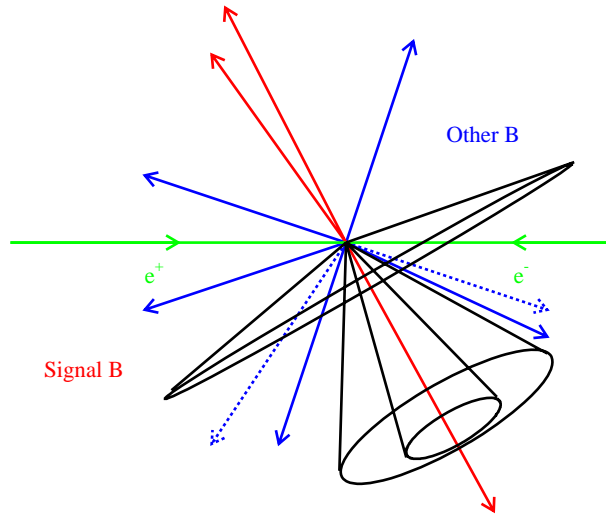


Figure 3.2: Drawings of decay topology of a generic signal event in the center of mass frame. The black cones around signal decay directions are commonly used to separate signal from background.

the background.

Two MVA techniques, a linear Fisher discriminant (FI) [54], and a non-linear Neural Network (NN) [55], have been studied. Optimization and training of the MVAs has been performed using off-resonance data contained in the signal region to reduce residual correlations of the NN with the kinematic variables used in the Maximum Likelihood fit (which will be discussed in Section 3.6). The FI and NN distributions for truth matched (TM) signal, combinatorial signal (SCF) and off-resonance data are plotted in Figure 3.3. As a qualitative measure of the discriminating power, we depict in Figure 3.4 the background efficiency versus the signal efficiency, obtained when cutting on the respective MVA outputs. We observe similar performance, with a slight advantage for the NN, so that it is adopted in the following analyses.

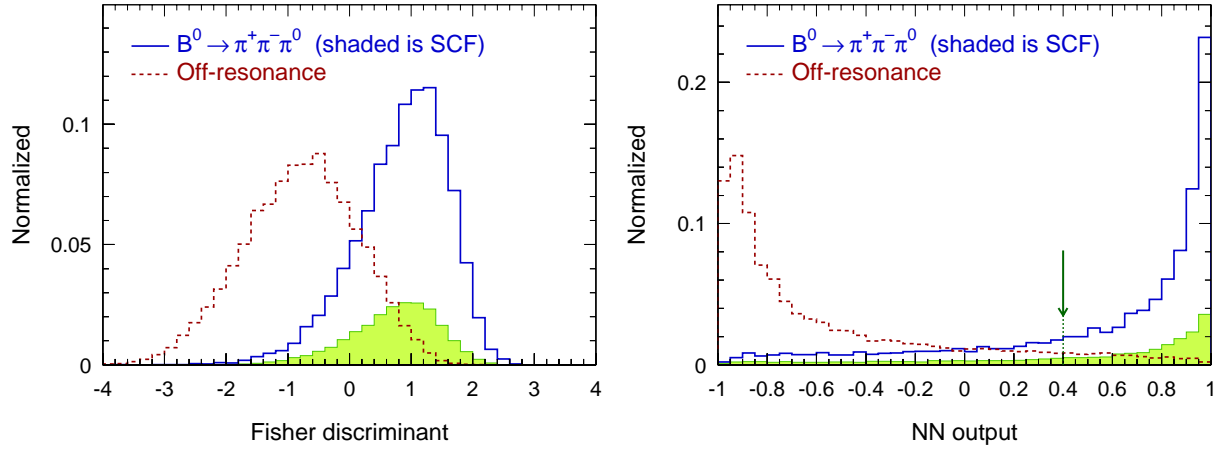


Figure 3.3: Output distributions for the Fisher discriminant (left plot) and the Neural Network (right plot), using the 4 discriminating variables defined in the text. Shown are TM signal (solid line), SCF signal (shaded area), and off-resonance data (dashed line). The arrow indicates the cut applied.

3.1.3 Suppression of B Related Background

Compared to charmless two-body B decays, charmless three-body B decays suffer from additional background from other charm and charmless B -decays, particularly due to the large decay width of the broad ρ resonance. Since some of these B -background modes can exhibit CP -violating asymmetries, and because their branching fractions are not always well-known, the 'peaking' B -related background is potentially more dangerous than the continuum background. We investigated the cross-feed from other B -decays and evaluated the systematic biases they can introduce in our measurements. The general strategy to deal with such background is to study the dominant contributions exclusively and introduce fixed terms in the likelihood fit that correspond to each contribution.

Charmed B -background Modes

Using generic $B^+ B^-$ and $B^0 \bar{B}^0$ Monte Carlo simulation, we select $b \rightarrow c$ events

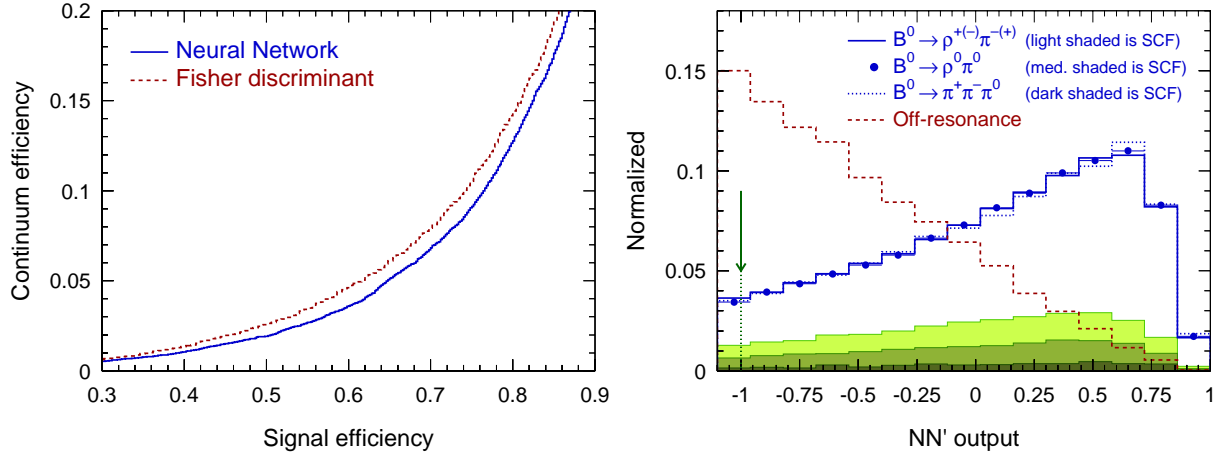


Figure 3.4: *Left: background efficiency as a function of the signal efficiency (including both TM and SCF), obtained from cuts on the MVA outputs. Right: normalized NN output for truth-matched (solid) and misreconstructed $\rho(\pi\pi)\pi$ events (shaded), and off-resonance data (dashed line). The arrow indicates the cut value applied.*

at the generator level, *i.e.* at least one of the final state particles of both the tag and the CP sides, are required to originate from a charmed mother or grandmother. In general, charmed B decays have high multiplicity. Thus, for the kinematic variables m_{ES} and ΔE , these events do not peak in the signal region. On the other hand, their NN distribution does exhibit a peaking structure. Figure 3.5 also demonstrates the ΔE distribution for the charmed B -background of $B^0 \rightarrow \rho^\pm \pi^\mp$ decay processes.

Charmless B -background Modes

An extensive list of charmless $B\bar{B}$ modes has been studied for each decay mode to evaluate the systematic uncertainties on the event yields and CP parameters. These modes can be categorized as 2-, 3- or 4-body final states, the decay kinematics of which all differ significantly:

- **2-body modes:** to reconstruct a $B \rightarrow \rho\pi$ candidate from pairs of pions or kaons, one adds an additional track taken from the ROE: as a consequence,

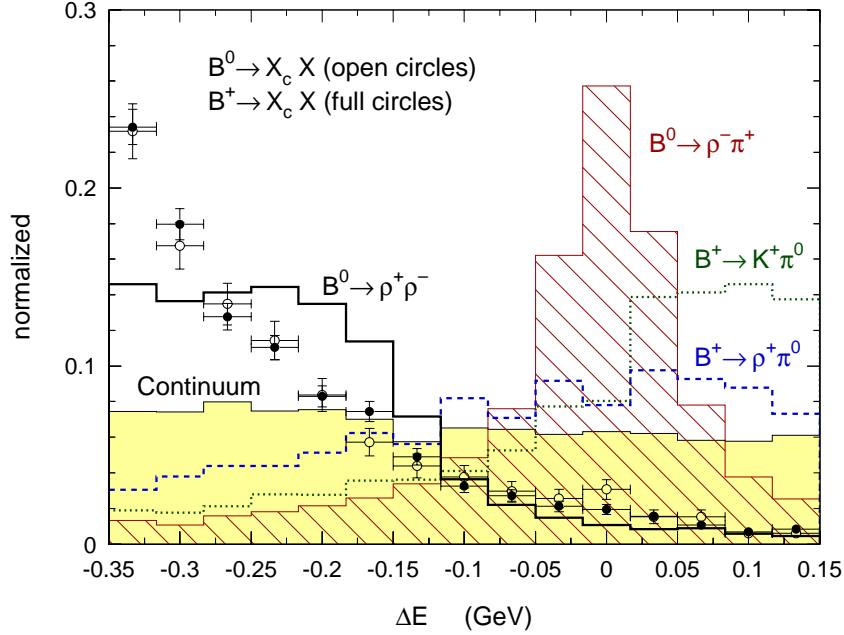


Figure 3.5: *Enlarged ΔE band. Shown are neutral and charged $b \rightarrow c$ events (full and open circles, respectively), signal $\rho^\pm \pi^\pm$ events (hatched region), and representative four (solid), three (dashed) and two-body (dotted) modes, all taken from MC simulation. The shaded band indicates the continuum contribution taken from off-resonance data.*

these events populate the positive ΔE region. The rates of the 2-body decays are well-known experimentally.

- **3-body modes:** by exchanging charged tracks between the signal B and the ROE, or by picking up fake soft charged π s, one can reconstruct a $B \rightarrow \rho\pi$ candidate from another 3-body mode. This approximately leaves ΔE unaltered, *i.e.*, $\Delta E, (3 - \text{body}) \sim 0$ – albeit with worse resolution. The kinematics of these processes resemble that of signal, so that the 3-body cross-feed is difficult to suppress without compromising the signal efficiency. In particular, 3-body background exhibits similar kinematic properties as the mis-reconstructed $B \rightarrow \rho\pi$ signal. The branching fractions of most of the 3-body modes have been

measured, although in many cases less accurately than those of most 2-body modes.

- **4-body modes:** by using only 3 objects of a 4-body decay, one can reconstruct a $B \rightarrow \rho\pi$ candidate, which accumulates in the negative ΔE region. Recently, there have been extensive efforts in the current B -factories to measure such decays.

Naturally the topological variables are not powerful to separate B -background from the signal. In this case ΔE is the most powerful variables to reject such backgrounds. Figure 3.5 shows the ΔE distributions for signal and for typical multi-body backgrounds for the $B^0 \rightarrow \rho^\pm \pi^\mp$ analysis. We use the measured branching fractions for the experimentally known decay modes. In cases where only upper limits are given, we translate the limits into branching fractions using the available information from the related publication. For all the other modes, not yet measured, educated guesswork is used to deduce their branching fractions. This is done using similar, known modes and, wherever possible, rules based on isospin symmetry and/or form factor arguments, usually assuming naive factorization of the matrix elements. If we must, we rely on ad hoc assumptions that consequently entail large systematic uncertainties.

For B decay into two vector mesons the vector-vector state can have $L = 0, 1, 2$ orbital angular momenta corresponding to longitudinal and transverse polarizations. Only longitudinally polarized particles create sufficiently fast decay pions and kaons to produce significant background after selection. We conservatively assume that these unmeasured modes are longitudinally saturated.

3.2 Vertexing and Δt Determination

In a time-dependent CP -violation measurement, it is crucial to determine the time difference between the two B decays in the $\Upsilon(4S)$ frame, as schematically shown in Figure 3.6. The SVT provides excellent spatial resolution for determining the decay vertices which are separated by the boost of the initial e^+e^- system. In this section, we describe the method of determining the Δt .

We use the same vertexing algorithms and the same Δz reconstruction technique as previous time-dependent analyses of B decays, namely the lifetime and mixing analyses [14, 13] using fully reconstructed B mesons, the $\sin 2\beta$ measurements [15] and the $B \rightarrow h^+h^-$ analysis [17]. Specifically, the vertex of the fully reconstructed $B \rightarrow \rho\pi$ candidates is determined using the `GeoKin` algorithm. The decay vertex of the “other B ” in the event is then determined using the `VtxTagBtaSelFit` algorithm including full beam-constraints (the so-called “pseudo-track”). We use a $\Delta z \rightarrow \Delta t$ conversion that is different from the one in the previous analyses cited above. The previous analyses use the *average τ_B approximation*. This $\Delta z \rightarrow \Delta t$ conversion includes a correction for the small boost of the B mesons in the $\Upsilon(4S)$ rest frame. In contrast to, *e.g.*, the $\sin 2\beta$ analysis using $J/\psi K_s^0$ or the lifetime measurement using fully reconstructed B decays, the present analyses deal with an event sample that is dominated by continuum background. For continuum events the *average τ_B approximation* does not make sense as there is no B flight in the $\Upsilon(4S)$ rest frame to be corrected for. This “correction” then introduces a smearing that results in correlations between the per-event error $\sigma(\Delta t)$ and Δt which are not simple to model. We avoid this by using the *boost approximation*. This simpler $\Delta z \rightarrow \Delta t$ conversion results in a slightly ($\simeq 4\%$)

worse Δt resolution for signal events than the *average τ_B approximation*. We use the same Δt resolution function parameters as the $\sin 2\beta$ analysis (i.e. measured in data using the *average τ_B approximation*), and apply a small correction estimated from Monte Carlo. This correction depends on the B lifetime and relativistic kinematics which are both well modeled in the Monte Carlo.

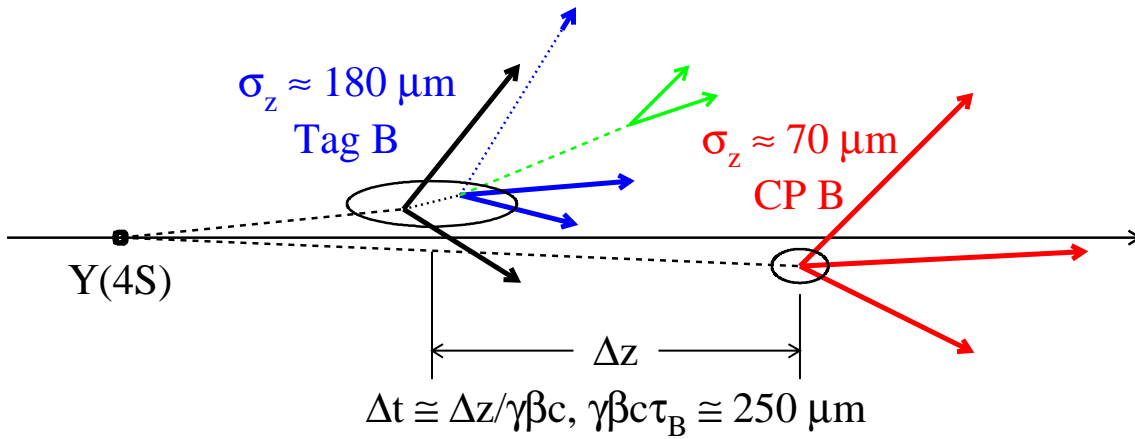


Figure 3.6: *Schematics of the determination of the decay time difference.*

3.3 B -Flavour Tagging

Another important ingredient in a time-dependent CP -violation measurement is to determine the flavor of the other B meson. Even for a branching fraction measurement for a charged B decay mode where tagging is in principle not necessary, tagging often provides additional sensitivity to the measurement by exploiting the content from the other B decay. In this section, we review the tagging algorithm.

For these analyses, the **ElbaTagger** algorithm is used to tag the flavour of the other (non- $\rho\pi$) B meson in the event. The algorithm searches for prominent charge-

carrying features of B -decays and uses them to determine the charge of the bottom-quark.

The ElbaTagger is a hybrid of two tagging algorithms: a cut-based tagging algorithm, N.O.T., and a neural network-based algorithm, NetTagger. Events with clearly identified leptons or kaons are used by N.O.T. to tag the B -flavour; the remaining events are passed to NetTagger, which exploits lower-momentum or unidentified leptons and soft pions to tag the flavour. Since each individual algorithm has strengths over the range of all events, they are combined into a single algorithm.

The ElbaTagger classes events into one of 4 mutually exclusive categories: **Lepton**, **Kaon**, **NT1**, or **NT2**. Events with a high-momentum identified electron ($p^* > 1.0 \text{ GeV}/c$) or muon ($p^* > 1.1 \text{ GeV}/c$) fall into the **Lepton** category, and the sign of the lepton is used to tag the flavor of the B -meson. Events that do not have such a lepton, but which contain one or more identified Kaons are tagged by the sum of the Kaon charges and fall into the **Kaon** category.

If an event cannot be classed as either **Lepton** or **Kaon** then it is passed to the NetTagger. If the output for the event is at very low (high) values of the NetTagger output, 0.0-0.25 (0.75-1.0), then it is classed as a \bar{B}^0 (B^0) in the **NT1** category. If the output is in the range 0.25-0.4 (0.6-0.75), then it is classed as a \bar{B}^0 (B^0) in the **NT2** category.

While the ElbaTagger enjoys reasonable data and Monte Carlo agreement, its tagging efficiency for signal events is measured using the **TagMix** method on **BReco** data. For mis-reconstructed signal events and B -background modes mistaken for our signal due to picking a track from the tag side, the tagging properties can be modi-

fied compared to the signal case. In particular, tagging efficiencies for each tagging category are affected. For example, the **Lepton** category owes less tracks to the tag side than do other hadronic categories, leaving less room for combinatorial effects with the CP side. This leads to a lower tagging efficiency in this category for the background modes. Specific B -background tagging efficiencies are thus obtained from MC simulations.

3.4 Data Sample and Event Processing

The results presented in this thesis are based on data collected between 1999 and 2002 with the *BABAR* detector. The data sample consists of:

- Run-1(1999): on-resonance - 0.5 fb^{-1} , off-resonance - 0.0 fb^{-1} ;
- Run-1(2000): on-resonance - 20.3 fb^{-1} , off-resonance - 2.6 fb^{-1} ;
- Run-2(2001): on-resonance - 35.6 fb^{-1} , off-resonance - 3.8 fb^{-1} ;
- Run-2(2002): on-resonance - 25.6 fb^{-1} , off-resonance - 3.1 fb^{-1} ;

For the study of the $B^0 \rightarrow \pi^+ \pi^- \pi^0$ Dalitz plot analysis, we also include the data taken in the first half of year 2004:

- Run-3(2003): on-resonance - 31.4 fb^{-1} , off-resonance - 2.4 fb^{-1} .
- Run-4(2003): on-resonance - 80.9 fb^{-1} , off-resonance - 4.2 fb^{-1} .

Fully simulated samples of Monte Carlo events are used to study the signal and background properties as well as the selection efficiencies. Imperfect simulation of shower leakage and neutral energy resolution in the EMC is corrected by applying the

“killing, smearing and scaling” procedure. Note, that these additional corrections are applied only to the B -decays with one or more π^0 s in the final states. Energy scaling effects are corrected separately for Run-1, Run-2 and Run-3, and weighted into the final Monte Carlo samples according to the integrated luminosities in these runs.

The preselection is designed to screen out apparently unrelated background events while keeping signal efficiencies as high as possible. The preselection begins by looping over all the combinations of either charged **GoodTracksLoose** tracks and/or **pi0LooseMass** candidates depending on what the final states are, and combining them into a list of B -candidates. The event is accepted if at least one B -candidate passes the following requirements:

- $m_{\text{ES}} > 5.1 \text{ GeV}/c^2$
- $|\Delta E| < 0.45 \text{ GeV}$

Tracks (**GoodTracksLoose**) and neutrals (**CalorNeutral**, $E_\gamma > 100 \text{ MeV}$) which do not contribute to the B -candidate reconstruction, are used for the calculation of event shape variables and B -flavor tagging.

The selection is subsequently designed to further improve the signal to noise ratio, *e.g.* by cutting on the continuum fighting MVA. Also used is the information of other kinematic variables, *e.g.* the mass and helicity structure of the intermediate resonance particles. The selection also cleans up the sample employing the *particle identification* (PID) information. And finally, selection cuts remove regions of the discriminating variables where modelling is difficult, *e.g.* the tail of the Δt distribution.

3.5 Misreconstruction and Multiple Candidates

Selected signal events are divided broadly into two categories: truth matched (TM) signal events and self-cross-feed (SCF) signal events. Truth matched signal events refer to those events where the correct final-state particles are identified in the reconstruction. The self-cross-feed signal events, also called misreconstructed signal events, are signal events where at least one particle not from the signal B decay is used in the reconstruction.

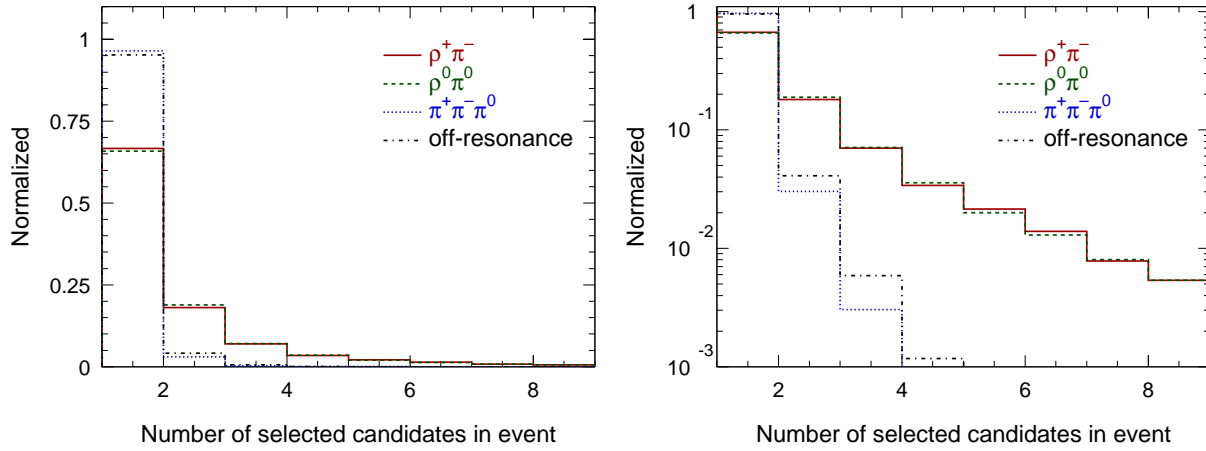


Figure 3.7: *Number of candidates per event passing the full selection. Shown are $B^0 \rightarrow \rho^\pm\pi^\mp$ (solid line), $B^0 \rightarrow \rho^0\pi^0$ (dashed line), $B^0 \rightarrow \pi^+\pi^-\pi^0$ (dotted line), and continuum background events (dashed-dotted line), represented in a linear (left plot) and logarithmic (right plot) scale.*

One problem related to the signal misreconstruction is that a given event can have multiple candidates that pass all the selections. Multiple candidates can occur both in background events and in good signal events due to combinatorics. Figure 3.7 shows the distributions of the number of candidates per event after all the selection cuts for the $B^0 \rightarrow \pi^+\pi^-\pi^0$ Dalitz plot analysis. In general, the average candidate multiplicity for continuum events is slightly lower than that of signal events. This is

due to the fact that continuum events have lower track multiplicity and continuum events are distributed more uniformly in the Dalitz plot than the signal events.

In the analysis, events with more than one candidate in the fitting region will be counted only once, *i.e.* the normalization is given by the number of events which have at least one candidate in the fitting region. The method to determine the best candidate varies among different analyses.

3.6 Maximum Likelihood Fit

The selected on-resonance data sample is assumed to consist of signal, continuum background and B -background components. The event yields for signal and continuum background, the time-dependent CP -violating parameters, as well as time-independent charge asymmetries are measured simultaneously by means of a *Extended Maximum Likelihood* (ML) fit. The fit exploits the topological variable and the kinematic variables to separate signal from background. The fit also exploit the time difference between the B decays to measure the time-dependent asymmetries. Explicit background contributions are also considered for background from charmed and charmless B decays. The probability density $\mathcal{P}_{i,c}$ for a single event i in tagging category c is the sum over the probability densities of all components, namely

$$\mathcal{P}_{i,c} = N_{\rho\pi} f_c^{\rho\pi} \frac{1}{2} \mathcal{P}_{i,c}^{\rho\pi} + N_{q\rho\pi}^c \mathcal{P}_{i,c}^{q\rho\pi} + \Xi_c^{\rho\pi} , \quad (3.2)$$

where:

- $N_{\rho\pi}$ is the number of signal events of type $\rho\pi$ in the entire data sample.
- $f_c^{\rho\pi}$ is the fraction of signal events of type $\rho\pi$ that are tagged in category c .

- $N_{q\rho\pi}^c$ is the number of continuum background events that are tagged in category c .
- $\mathcal{P}_c^{\rho\pi} = \mathcal{P}^{\rho\pi}(m_{\text{ES}}) \cdot \mathcal{P}^{\rho\pi}(\Delta E) \cdot \mathcal{P}^{\rho\pi}(\text{NN}) \cdot \mathcal{P}_c^{\rho\pi}(\Delta t)$,
- $\Xi_c^{\rho\pi}$ denotes the B -background contributions.

To avoid potential bias on the signal yields, we split the signal PDFs into two parts: truth matched events and self-cross-feed events. The signal piece of Eq. (3.2) is therefore modified as follows:

$$N_{\rho\pi} \mathcal{P}_{i,c}^{\rho\pi} \longrightarrow N_{\rho\pi} \left\{ (1 - f_{\text{scf}}) \mathcal{P}_{i,c,\text{TM}}^{\rho\pi} + f_{\text{scf}} \mathcal{P}_{i,c,\text{scf}}^{\rho\pi} \right\}, \quad (3.3)$$

where f_{scf} is the fraction of misreconstructed events in the signal. In the case of a charged B decay, one has to take into account the further complication that the charge of the B could be misreconstructed as well, thus introducing dilution to the charge asymmetry measurement. The extended likelihood over all tagging categories is given by

$$\mathcal{L} = \prod_{c=1}^5 e^{-N'_c} \prod_i^{N_c} \mathcal{P}_{i,c}, \quad (3.4)$$

where N'_c is the number of events expected in category c . Including this term allows for the direct fitting of event yields rather than fractions. The dominant background to $B \rightarrow \rho\pi$ decay is from continuum production. Due to the large continuum background over signal excess in our fitting sample, it is crucial to get a perfect description of the continuum events. The strategy adopted is to include sideband events in the fit and determine all the continuum related yields and PDF parameters from data

simultaneously with the signal parameters.

3.7 Correlations

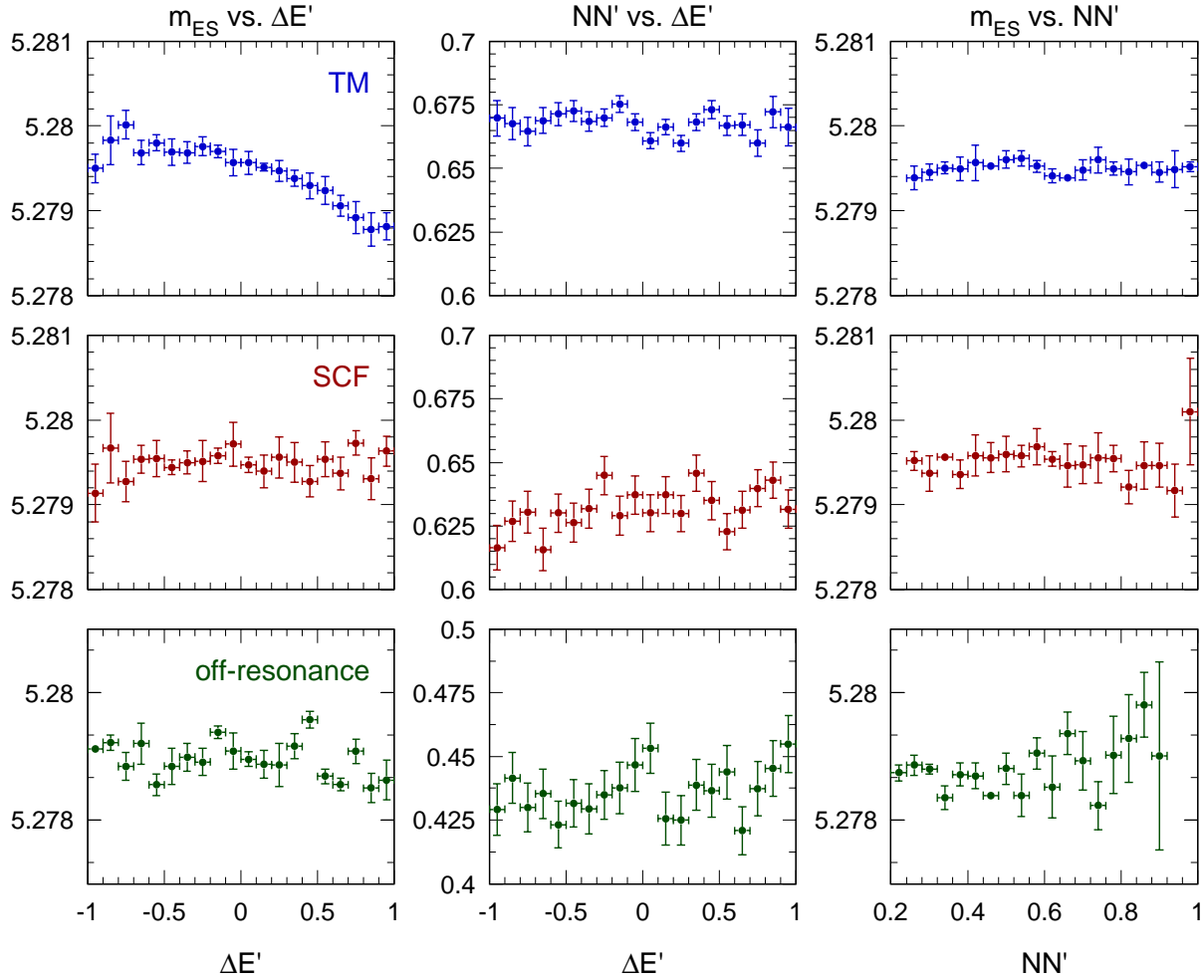


Figure 3.8: Correlation profiles of m_{ES} versus $\Delta E'$, NN' versus $\Delta E'$, and m_{ES} versus NN' , for correctly reconstructed $\rho^{\pm}\pi^{\mp}$ signal events (upper line), mis-reconstructed (center line) events, and off-resonance events (lower line).

The ML fit designed is a multi-dimensional fit which uses the discriminant variables m_{ES} , ΔE , NN and Δt as input. Yet, the likelihood model is built upon the assumption that these variables do not exhibit correlations among themselves. Viola-

tion of this assumption leads to biases in the fit. Using the $B^0 \rightarrow \pi^+\pi^-\pi^0$ Dalitz plot analysis as an example, some of the correlation profiles, for correctly reconstructed signal events and mis-reconstructed $\rho^\pm\pi^\mp$ events, and off-resonance events are plotted in figure 3.8. Significant correlations are only observed for TM events between m_{ES} and $\Delta E'$. Their linear correlation coefficient amounts to -8.6% , which is a known feature and understood to be dominated by the common uncertainty on the beam energy. The effect of the residual correlation among discriminant variables is estimated from Monte Carlo simulation and is assigned as systematic uncertainty.

Chapter 4

Study of $B^\pm \rightarrow \rho^\pm \pi^0$ Decays

4.1 Introduction

The $B^\pm \rightarrow \rho^\pm \pi^0$ has not been previously observed although a branching fraction of the order 10^{-5} is expected. The difficulty in this analysis is the presence of multiple π^0 s in the final state. CLEO reported an upper limit of 4.3×10^{-5} on this decay [38]. It is clear that the observation of this mode is beyond their search sensitivity. In particular, they noticed that it is impossible for them to distinguish a decay dominant by the ρ resonance from a non-resonant $\pi^+ \pi^0 \pi^0$ decay.

4.2 Candidate Selection

In order to reconstruct the $\rho^\pm \pi^0$ final state, we loop over all the combinations of one charged **GoodTracksLoose** track, two **pi0LooseMass** candidates, and combine them into a list of B -candidates. To further improve the signal-to-background ratio, candidates which pass the preselection must satisfy additional requirements.

- $5.20 < m_{\text{ES}} < 5.29 \text{ GeV}/c^2$.
- $-0.15 < \Delta E < 0.10 \text{ GeV}$. See Fig. 4.1 for ΔE versus m_{ES} scatter plots for

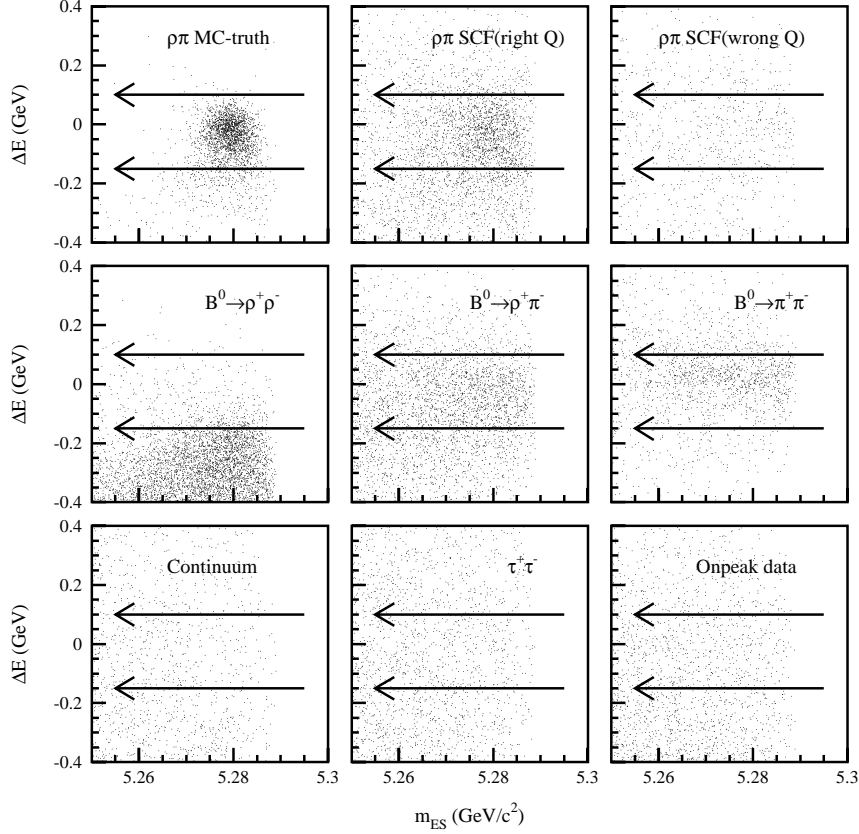


Figure 4.1: *CM energy difference, ΔE , versus the energy-substituted-mass, m_{ES} , for the various signal contributions and background processes. Indicated by the arrows are the selection cuts applied on ΔE .*

various signal contributions and background processes.

- To exploit the information of the intermediate resonance ρ , candidate events should have invariant masses $m(\pi^\pm \pi^0)$ within the following ranges: $0.4 < m(\pi^\pm \pi^0) < 1.3 \text{ GeV}/c^2$.
- The helicity angle (the polar angle of the charged pion in the ρ frame) of the ρ^+ and ρ^- candidates is required to satisfy $|\cos\theta_H(\rho)| > 0.25$. Here we exploit the

fact that since ρ is a vector particle, it is longitudinally polarized in the $B \rightarrow \rho\pi$ decay.

- The charged track must fail the tight electron ID, the tight Kaon ID and the tight proton ID.
- The continuum-fighting Neural Network (xNN) output is required to be larger than 0.6. The NN is built using the six discriminating variables: $m(\rho)$, $\cos\theta_H(\rho)$, L_0 , L_2 , $\cos\theta_{B,z}$ and $\cos\theta_{T_B,z}$.

All cut efficiencies for signal $B^\pm \rightarrow \rho^\pm \pi^0$ Monte Carlo, data, and $udsc$ MC and $\tau^+\tau^-$ samples are shown in Table 4.1.

In case of more than one candidates pass the selection criteria for a single event, we choose the candidate with the ρ invariant mass closest to the PDG value. If there is more than one candidate with the same ρ invariant mass, we use the first one. The final selection efficiencies, mischarge (ω_Q) and combinatorial background rates (f_{scf}) are summarized in Table 4.2. The fractions of misreconstructed signal events vary significantly in different tagging categories and they are summarized in Table 4.3.

4.3 Backgrounds from B Decay

Table 4.4 gives the branching fractions and efficiencies for some of the cross-feed modes considered. Several other background modes were examined and only the ones that have more than one event expected after final candidate selection are included. An asterisk indicates the modes which are not known experimentally and whose branching fractions have been inferred from theoretical arguments, this is presented in ref. [37] in detail.

Cut description	$\epsilon_{\rho\pi}^{\text{MC}} [\%]$	$\epsilon_{\text{on}}^{\text{Dat}}$	$\epsilon_{\text{off}}^{\text{Dat}}$	$\epsilon_{uds}^{\text{MC}}$	$\epsilon_{c\bar{c}}^{\text{MC}}$	$\epsilon_{\tau^+\tau^-}^{\text{MC}}$
Reconstruction	44.8	-	-	2.4	1.1	0.8
$-0.15 < \Delta E < 0.10$ GeV	82.5	45.6	45.0	47.9	47.6	39.7
$5.20 < m_{\text{ES}} < 5.29$ GeV/ c^2	97.6	74.5	76.1	74.5	72.5	76.8
Photon quality (π_1^0)	96.5	91.0	91.7	90.2	91.1	93.1
Photon quality (π_2^0)	90.7	78.6	80.4	79.9	84.2	78.4
$0.11 < m_{\pi_1^0} < 0.16$ GeV	98.6	95.8	95.7	95.7	94.5	96.9
$0.11 < m_{\pi_2^0} < 0.16$ GeV	97.5	94.0	94.0	94.1	93.2	95.0
electron veto	99.0	97.2	97.2	98.4	97.3	91.1
muon veto	98.6	98.2	98.2	98.2	96.6	92.1
kaon veto	98.2	82.3	82.6	87.3	70.2	96.4
proton veto	99.7	94.6	94.4	91.8	95.4	99.6
$m(\pi^+\pi^0) < 5.14$ GeV	99.6	99.8	99.9	99.7	99.8	99.9
$m(\pi^0\pi^0) < 5.14$ GeV	99.9	100	100	100	100	100
$0.4 < m_\rho < 1.3$ GeV	93.0	54.2	54.7	56.6	52.5	67.9
$ \cos\theta_H(\rho) > 0.25$	98.3	79.4	79.6	80.7	80.0	74.3
xNN > 0.6	66.7	4.3	4.2	4.1	3.2	8.3
Total efficiency	17.6			0.0079	0.0021	0.0058

Table 4.1: $\rho^\pm\pi^0$ analysis: Summary of cut efficiencies for signal MC, data and $udsc$ MC samples. The efficiencies for each individual line of the table are given relative to the number of events retained after passing the skim cuts, they don't include the loss of events from the other cuts. Signal Monte Carlo includes any event that passes the selection.

It is difficult to distinguish a $\pi^+\pi^0\pi^0$ non-resonant contribution from signal events. Currently no branching fraction measurement exists for this non-resonant decay. We try to estimate how significant the non-resonant contribution can be. We perform a search similar to that for signal, but for non-resonant events in the center of the $\pi^+\pi^0\pi^0$ Dalitz plot. The non-resonant signal efficiency in this search is 7.7%; we find the following yield:

$$N_{\text{non-res}} = -14.8 \pm 9.6(\text{stat.}) \pm 8.8(\text{syst.}) \quad (4.1)$$

Given that the non-resonant efficiency in the nominal $\rho^\pm\pi^0$ analysis is 2.7% we make

Mode	$\epsilon(\%)$	$\langle f_{scf} \rangle(\%)$	$\omega_Q(\%)$
$\rho^\pm \pi^0$	17.6 ± 0.1	38.6 ± 0.3	20.9 ± 0.3

Table 4.2: *Summary of the final selection efficiency, the averaged misreconstruction rate and the fraction of misreconstructed signal that has the wrong charge assignment for $B^\pm \rightarrow \rho^\pm \pi^0$ events. Errors given are statistical only.*

	Lepton	Kaon	NT1	NT2	NoTag
$f_{scf}(\%)$	27.7 ± 0.7	38.9 ± 0.4	31.9 ± 1.0	39.3 ± 0.8	42.8 ± 0.5

Table 4.3: *Summary of fraction of misreconstructed signal events for $B^\pm \rightarrow \rho^0 \pi^\pm$ events in different tagging categories. Errors given are statistical only.*

the reasonable assumption that the number of non-resonant events in the $\rho^\pm \pi^0$ signal region is negligible. A measurement of the non-resonant branching fraction is not attempted here. Instead, we estimate only the possible number of events in the signal region. In the final result it is stated that all the signal $\pi^\pm \pi^0 \pi^0$ events are assumed to contain a ρ resonance.

No attempt is made to group other B -related background into 2,3 and 4-body modes in the likelihood fit; rather, most modes are treated individually. ΔE and m_{ES} correlations in various B -background modes are accounted for by using 2-dimensional non-parametric shapes. In the nominal fit we assumed a charge asymmetry of zero for both charged and neutral B -background modes. This is a reasonable assumption since the measured values that exist are statistically compatible with zero and none of the modes is expected to have a significant charge asymmetry. A possible non-zero asymmetry is taken into account when the B -background systematic errors are estimated.

#	Mode	BR (10^{-6})	ϵ (%)	N_{exp}
1	$B^0 \rightarrow \rho^+ \rho^-$ long.	40.0^{+50*}_{-35}	1.84	65.4^{+82}_{-57}
2	$B^0 \rightarrow \rho^+ \rho^-$ tran.	40.0^{+50*}_{-35}	0.05	$1.8^{+2.2}_{-1.3}$
3	$B^+ \rightarrow \rho^+ \rho^0$ long.	$31.7^{+8.1}_{-9.8}$	0.61	$17.2^{+4.4}_{-5.3}$
4	$B^0 \rightarrow \rho^\pm \pi^\mp$	22.5 ± 4.0	2.31	46.2 ± 8.2
5	$B^0 \rightarrow \rho^- K^+$	$7.3^{+2.6}_{-2.5}$	0.38	2.5 ± 1.0
6	$B^0 \rightarrow K^*(K\pi)\pi^0$	8.7 ± 5.0	0.50	3.9 ± 2.2
7	$B^0 \rightarrow K^*(K_s\pi^0)\pi^0$	7.5 ± 5.0	0.58	3.9 ± 2.6
8	$B^+ \rightarrow K^{*+}(K\pi^0)\pi^0$	4.4 ± 2.5	1.57	6.1 ± 3.5
9	$B^+ \rightarrow \rho^+ \gamma$	2.3 ± 2.3	0.65	1.3 ± 1.3
10	$B^0 \rightarrow \pi^0 \pi^0$	1.6 ± 1.6	3.40	4.8 ± 4.8
11	$B^+ \rightarrow \pi^+ \pi^0$	5.2 ± 0.8	1.24	5.7 ± 0.9
12	$B^+ \rightarrow K^+ \pi^0$	12.7 ± 1.2	0.44	5.0 ± 0.5
13	$B^+ \rightarrow K^{*++} \pi^0$	40 ± 40	0.42	15 ± 15
14	$B^+ \rightarrow (K^{**}\rho)^+$	20 ± 20	0.07	1.2 ± 1.2
15	$B^0 \rightarrow K^{*0} \pi^0$	72 ± 72	0.36	23 ± 23
16	$B^0 \rightarrow (K^{**}\rho)^0$	20 ± 20	0.09	1.8 ± 1.8
17	$B^+ \rightarrow a_1^+ \pi^0$	35 ± 35	0.80	25 ± 25
18	$B^+ \rightarrow K_S^0 (\rightarrow \pi^0 \pi^0) \pi^+$	4.1 ± 0.4	1.47	5.4 ± 0.4
Total charmless				235 ± 80
18	$B^0 \rightarrow \text{charm}$	—	—	73 ± 22
19	$B^+ \rightarrow \text{charm}$	—	—	134 ± 40
Total				442

Table 4.4: *Classification of background from charged and neutral Bs. Efficiencies and expected event yields are obtained from Monte Carlo. The asterisk corresponds to modes where the branching fraction has been estimated from theoretical argument. Only the modes that have a non-insignificant contribution are listed. The number of expected events correspond to a data sample of 81.9 fb^{-1} .*

4.4 Systematic Uncertainties due to B -background

To evaluate of the systematic error due to B -background we vary the branching fractions and CP parameters within a chosen range and check how the measured quantities are affected. Details of the estimated systematic uncertainties are presented.

Uncertainty on the Branching Fractions

Mode	BR-variation		A_{CP} -variation	
	ΔN^{sig}	$\Delta A_{CP}^{\text{sig}}$	ΔN^{sig}	$\Delta A_{CP}^{\text{sig}}$
$B^0 \rightarrow \rho^+ \rho^-$	10.2	0.003	-	-
$B^+ \rightarrow \rho^+ \rho^0$ long.	0.7	0.013	0.03	0.019
$B^0 \rightarrow \rho^\pm \pi^\mp$	1.2	0.002	0.17	0.011
$B^0 \rightarrow \rho^- K^+$	0.3	0.001	-	-
$B^0 \rightarrow K^* \pi^0$	0.3	0.000	0.26	0.006
$B^+ \rightarrow K^{*+} (K \pi^0) \pi^0$	1.3	0.001	1.60	0.023
$B^+ \rightarrow \rho^+ \gamma$	0.5	0.001	-	-
$B^0 \rightarrow \pi^0 \pi^0$	1.1	0.002	-	-
$B^+ \rightarrow \pi^+ \pi^0$	0.3	0.001	0.00	0.002
$B^+ \rightarrow K^+ \pi^0$	0.1	0.000	0.00	0.001
$B^+ \rightarrow K^{*+} \pi^0 (K^{*+} \rho^0)$	1.2	0.001	0.30	0.014
$B^0 \rightarrow K^{*0} \pi^0 (K^{*0} \rho^0)$	2.0	0.002	0.51	0.022
$B^+ \rightarrow a_1^+ \pi^0$	1.8	0.001	0.59	0.023
$B^+ \rightarrow K_S^0 \pi^+$	0.1	0.000	0.13	0.004
Other Modes	1.4	0.002	-	-
$B \rightarrow \text{charm}$	1.5	0.000	-	-
Total	11.1	0.015	1.8	0.048

Table 4.5: B -background systematic errors due to branching fraction and A_{CP} variations. The Other Modes category refers to the charmless modes that are nominally negligible (< 1 event) but the uncertainty in their branching fractions yields an expectation above 1 event.

For the study of the systematics related to the uncertainty on the branching fractions of the B -background components, we consider two cases:

- If the branching fraction is measured, we vary the branching fraction within the

uncertainty of the measurement.

- If the branching fraction is not measured (*i.e.* modes with an asterisk in Table 4.4), we vary the branching fraction within the estimated range and we divide the change in the $\rho^\pm\pi^0$ signal yield by $\sqrt{3}$ to take into account the smaller RMS of a uniform prior compared to that of a Gaussian standard deviation.

Some of the modes have branching fractions that are correlated (modes 1-2, modes 6-8, modes 13-14, modes 15-16); and the systematic uncertainties from these modes are added linearly. The resulting values are then added in quadrature with each other and the other non-correlated modes. The largest effect due to the branching ratio uncertainties is observed for the determination of the signal yield.

Systematics Related to B -background A_{CP}

In addition, we have determined the uncertainty on the measured charge asymmetry due to the possible direct CP violation in the B -background modes. For each B -background mode, we determine the range of variation of A_{CP} as reconstructed in this analysis according to whether or not there has already been a measurement of its physical charge asymmetry, A_{CP}^* . If there is a measurement, we quote the measured uncertainty as the range of variation for A_{CP}^* . If there is no measurement, we consider the maximum CP violation scenario for the computation of the systematic error. We also take into account the possible difference between A_{CP} and A_{CP}^* for every mode. This is the dilution effect $D \equiv A_{CP}/A_{CP}^*$ and for each B -background mode, A_{CP} is varied from $-DA_{CP}^*$ to $+DA_{CP}^*$.

The charm contribution is conservatively varied by 30%. For the $B^0 \rightarrow \rho^\pm\pi^\mp$ analysis [37] extensive analyses are carried out to accurately estimate the charm con-

tribution [37], it is determined that the uncertainty on estimating the charm contamination is 24%. The charm A_{CP} is expected to be zero and is not varied. A summary of the systematic errors related to B backgrounds is given in table 4.5.

4.5 The Maximum Likelihood Fit

We use the likelihood function defined in equation 3.2, but in addition we fit for the charge asymmetry. Thus we further split the SCF PDFs into two parts: misreconstructed events with correct ($[Q_\rho]$) and incorrect ($[-Q_\rho]$) charge assignments. The signal piece of equation (3.2) is therefore modified in the following way:

$$\begin{aligned}
 (1 + Q_\rho A_{CP}^{\rho\pi}) \mathcal{P}_{i,c}^{\rho\pi} \longrightarrow & (1 + Q_\rho A_{CP}^{\rho\pi}) \left[(1 - f_{\text{scf}}) \mathcal{P}_{i,c,\text{tru}}^{\rho\pi} + f_{\text{scf}} (1 - \omega_Q) \mathcal{P}_{i,c,\text{scf}[Q_\rho]}^{\rho\pi} \right] \\
 & + (1 - Q_\rho A_{CP}^{\rho\pi}) f_{\text{scf}} \omega_Q \mathcal{P}_{i,c,\text{scf}[-Q_\rho]}^{\rho\pi} .
 \end{aligned} \tag{4.2}$$

4.6 Fit Results

The result of the final fit to the data of 81.9 fb^{-1} is shown in Table 4.6. After correcting for the expected bias of 14.4 events obtained from the Monte Carlo fits, we find $169.0 \text{ } B^\pm \rightarrow \rho^\pm \pi^0$ events in the selected data set with a statistical error of 28.7 events. The statistical significance of this previously unobserved signal amounts to 9.2σ , which we calculate by looking at the difference in the $-\ln(\mathcal{L})$ values when the signal yield is fixed to zero and when it is fixed to the bias corrected value. To calculate the total significance, the signal yield is fixed to 21.1 instead of zero, which corresponds to the systematic uncertainty. This yields a signal significance of 7.3σ .

Parameter	Description	Value
N_{signal}	Number of $B^\pm \rightarrow \rho^\pm \pi^0$ events	183 ± 29
A_{CP}^{signal}	CP -violating charge asymmetry in $B^\pm \rightarrow \rho^\pm \pi^0$	-0.24 ± 0.16
ξ	Continuum ARGUS slope parameter	-16.8 ± 1.1
$\langle m_B \rangle$	mean of the m_{ES} PDF GeV/c^2	5.2813 ± 0.0007
ΔE_{p1}	Slope of the continuum ΔE PDF	-1.10 ± 0.13
β_1	Continuum NN parameter	1.38 ± 0.08
β_2	Continuum NN parameter	1.63 ± 0.28
β_3	Continuum NN parameter	-1.16 ± 0.11
A_{CP}^{cont}	Charge asymmetry in continuum events	0.005 ± 0.009
$N_{\text{cont}}^{\text{Lepton}}$	Num. of continuum events in Lepton category	36.3 ± 7.8
$N_{\text{cont}}^{\text{Kaon}}$	Num. of continuum events in Kaon category	2971 ± 57
$N_{\text{cont}}^{\text{NT1}}$	Num. of continuum events in NT1 category	523 ± 24
$N_{\text{cont}}^{\text{NT2}}$	Num. of continuum events in NT2 category	1975 ± 46
$N_{\text{cont}}^{\text{NoTag}}$	Num. of continuum events in NoTag category	7053 ± 86

Table 4.6: *Summary of the final $\rho^\pm \pi^0$ fit prior to signal yield bias correction.*

Figure 4.2 shows the distribution of m_{ES} and ΔE , enhanced in signal content by cutting on the signal-to-continuum likelihood ratios of the discriminating variables. There is clearly a signal present in the data. The agreement between data and Monte Carlo expectation is fairly good, but the statistics is still low.

To check in an unbiased way whether the observed signal events are consistent with $\rho\pi$ signal or not, the analysis is repeated without using the ρ related information (*i.e.* $m(\rho)$ and $\cos\theta_H(\rho)$) in the selection. The neural network is replaced by a two-variable one (L_0, L_2), and in the case of multiple candidates the one with the best soft π^0 mass was selected. A PDF for the $m(\rho)$ was added to the likelihood, parametrized as a double Gaussians for truth matched signal and continuum events. The parameters of the continuum double-Gaussian were floating in the fit to data while the signal ρ -parameters were fixed to values determined from Monte Carlo. The resulting ρ mass

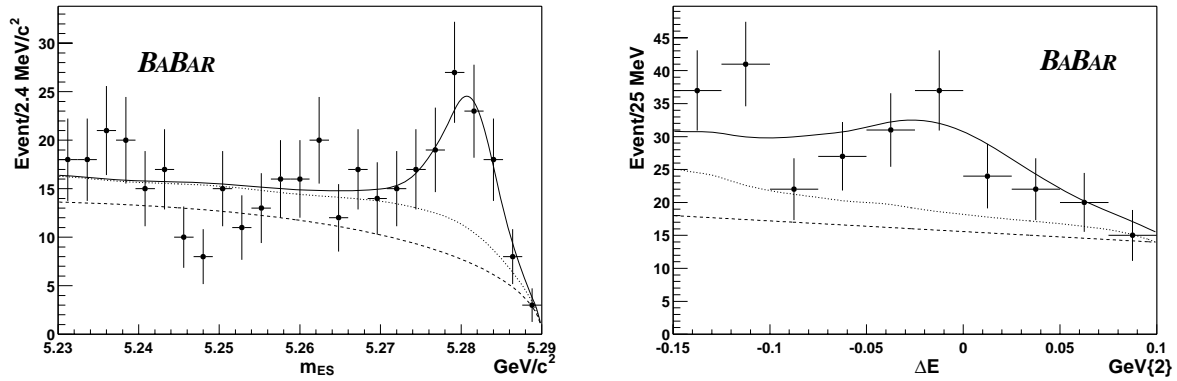


Figure 4.2: Distributions of m_{ES} , ΔE , enhanced in signal content for $B^\pm \rightarrow \rho^\pm \pi^0$ analysis. The solid curve represents a projection of the maximum likelihood fit result. The dashed curve represents the contribution from continuum events, and the dotted line indicates the combined contributions from continuum events and B -related backgrounds.

distribution, enhanced in truth matched signal content by cutting on the signal-to-background likelihood ratio of other discriminating variables, are shown in Figure 4.3.

The signal in the data is perfectly consistent with $B^\pm \rightarrow \rho^\pm \pi^0$ events.

4.7 Study of the Systematic Uncertainties

The nominal value of the efficiency for $B^\pm \rightarrow \rho^\pm \pi^0$ selection is calculated using fully simulated Monte Carlo events. All the fits in this analysis are done with no constraints applied to the absolute number of $\rho^\pm \pi^0$ events. One could use this information to calculate corresponding branching fraction, but first the following corrections have to be taken into account.

- To take tracking efficiency corrections into account, the Monte Carlo efficiency has to be scaled by an average factor of 0.99. Since there is only one charged track in this channel, according to the *BABAR* tracking recipe a 0.8% systematic error should be assigned.

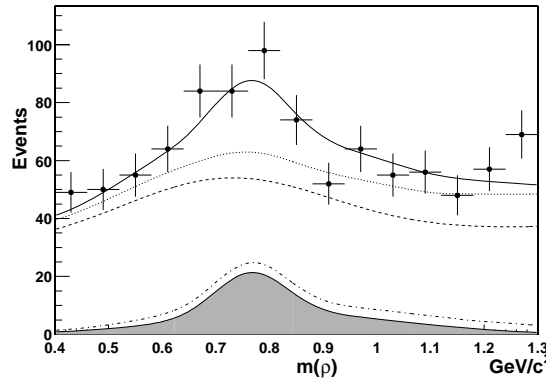


Figure 4.3: *Distribution of m_ρ , enhanced in the signal content in $B^\pm \rightarrow \rho^\pm \pi^0$ analysis. The solid curve represents a projection of the maximum likelihood fit result. The dashed curve represents the contribution from continuum events, and the dotted line indicates the combined contributions from continuum events and B -related backgrounds. The dash-dotted curve shows the true-signal plus SCF contributions whereas the shaded area represents the true-signal contribution only. To make this plot the fit was repeated after all removing ρ -related information from the NN and the selection.*

- π^0 killing and smearing is applied by default to every Monte Carlo sample. The systematic uncertainties are taken from the standard *BABAR* recipe.
- The total of $B\bar{B}$ events is obtained using *BABAR* B -counting procedure and equals to: 88.9 ± 0.2 million.
- PID killing for the tracks is performed according to the *BABAR* recipe. It results in 1.7% relative change in the signal Monte Carlo efficiency, which is assigned as a systematic error.
- All other systematic errors will be discussed in detail in the rest of this section.

Study of the Fit Systematic Uncertainties

- **Tagging:** To determine the tagging fraction systematic uncertainty, we used the statistical errors on these numbers from Breco [15]. Fits were re-done by varying

the tagging fractions conservatively. The difference observed with respect to the nominal fit is taken as systematic error.

- **Self cross feed:** The uncertainty in the SCF fraction was determined from fully reconstructed $B^0 \rightarrow D^- \rho^+$ events, and the assumption was made that both channels have the same SCF uncertainty. The study of the $D\rho$ control sample shows that the uncertainty is $\pm 5\%$, and to be conservative we doubled this value.
- **Mischarge rate:** In the case when the charged track is soft, the wrong charge might be assigned to the ρ . This occurs among the events that are classified as SCF. Since the SCF uncertainty is $\pm 10\%$, the mischarge rate was also varied by the same amount for the systematic uncertainty.
- **Neural network:** The NN PDF systematic uncertainty was evaluated using the correction function from **BReco** validation. This correction was again obtained from the $D^- \rho^+$ control sample. Very little discrepancy between the data and Monte Carlo was found for the $\rho^\pm \pi^0$ NN output. The data was refit with the observed difference in the NN shape and the resulting difference is taken as the systematic uncertainty.
- m_{ES} : The systematic uncertainty due to the m_{ES} PDF was obtained after comparing $D^- \rho^+$ events in data and generic Monte Carlo. It was observed that there is a 7.1% difference in the resolution between the data and generic Monte Carlo. Since the mean of this PDF is allowed to float, only the resolution can introduce a systematic effect. The events were fit with a $\pm 7.1\%$ smearing of the m_{ES} PDF

and the largest difference was taken as the systematic uncertainty.

- **ΔE :** The uncertainty in the ΔE distribution is dominated by the hard π^0 in the decay. To determine this systematic uncertainty, we chose a direct comparison between the data and signal MC. We use a control sample of the $K^+\pi^0$ that contains a hard pion, to evaluate this uncertainty. Since in the $\rho^+\pi^0$ sample there are two π^0 s, these two shifts were added linearly to obtain a total possible shift. This is a conservative estimate since we do not expect the same large discrepancy for the soft pions as for the hard ones.
- **B -background:** The B -background modeling is the main source of systematic uncertainty in this analysis, and a conservative estimation of this uncertainty is described in section 4.4.

We perform fits on the large Monte Carlo samples with the measured proportions of signal, continuum and B -backgrounds. Biases observed in these tests are due to imperfection in the likelihood model, *e.g.*, correlations between the discriminating variables of the signal and B -background PDFs. The observed signal yields are corrected for these fit biases and the full correction is assigned as a systematic uncertainty. The effect of these systematic uncertainties on the signal yield and charge asymmetry can be found in tables 4.7 and 4.8.

Study of the Efficiency Systematic Uncertainties

It is necessary to know the systematic uncertainty on the signal selection efficiency if a branching fraction is to be calculated. The basis for evaluating the systematic uncertainties on the cuts that are applied in the selection process is a comparison between data and Monte Carlo. We use the $B^0 \rightarrow D^-\rho^+$ validation sample to look

at the differences in the m_{ES} and m_ρ shapes. For ΔE a $B^+ \rightarrow K^+\pi^0$ sample is used. To smear the ΔE shape, we employ the same method as when evaluating the ΔE fit uncertainty. The procedure to evaluate the NN cut systematic uncertainty is more involved. It uses the validation data and Monte Carlo samples. The fitter is changed such that the $D^-\rho^+$ yield can be fit directly. Two fits are performed, one without a NN cut and one with the nominal cut. The yields from these two fits provide a measure for the data efficiency. This is compared to the Monte Carlo efficiency and the difference is taken as the systematic uncertainty. The systematic uncertainties on the various cuts are summarized in Table 4.7.

4.8 Summary

We have measured the $B^\pm \rightarrow \rho^\pm \pi^0$ branching ratio and its direct CP violating asymmetry, A_{CP} using a maximum likelihood analysis. The result is obtained from a data sample of a total integrated luminosity of 81.9 fb^{-1} collected at the $\Upsilon(4S)$ resonance and 9.5 fb^{-1} taken 40 MeV below the $\Upsilon(4S)$ resonance in the (2000–2002) period by the *BABAR* detector at the PEP-II asymmetric-energy B Factory at SLAC. The measured branching fraction is $(10.9 \pm 1.9(\text{stat.}) \pm 1.9(\text{syst.})) \times 10^{-6}$, and the CP -violating charge asymmetry is $0.24 \pm 0.16(\text{stat.}) \pm 0.06(\text{syst.})$. To obtain this result, the assumption is made that the $\pi^\pm \pi^0 \pi^0$ non-resonant decay is negligible and all the signal events observed contain the ρ^\pm resonance. The total significance for the observed signal yield corresponds to 7.3σ .

	$B^\pm \rightarrow \rho^\pm \pi^0$	Comments
	Signal yields and efficiencies	
N_{signal}	183.4	fit to data
Corrected N_{signal}	169.0	corrected for the fit bias
$\epsilon_{\text{signal}}^{\text{raw}}$	$17.6 \pm 0.1\%$	smeared signal MC
ϵ_{signal}	$17.5 \pm 0.1\%$	tracking correction
Statistical Error on N_{signal}	28.7	parabolic error from fit
	Relative efficiency and scaling systematics	
Tracking	0.6%	per-track-corrections
PID for tracks	1.7%	PID killing AWG recipe
π^0 -correlated	10.0%	smearing/scaling/killing
π^0 -uncorrelated	2.0%	smearing/scaling/killing
ΔE cut	2.6%	BReco-MC PDF cut diff.
m_{ES} cut	0.0%	BReco-MC PDF cut diff.
m_ρ cut	0.3%	BReco-MC PDF cut diff.
$\cos\theta_H(\rho)$ cut	1.5%	BReco-MC PDF cut diff.
NN cut	4.0%	BReco-MC PDF cut diff.
$N(B\bar{B})$	1.1%	B-counting
Sub-total:	11.6%	
	Fit systematics	
B Tagging	3.7	parameters from BReco
Fraction of SCF($\pm 10\%$)	5.9	parameter variation
Mischarge Fraction($\pm 10\%$)	0.1	parameter variation
ΔE PDF	7.1	PDF shift and shape
m_{ES} PDF	2.5	PDF shift and shape
NN PDF	3.0	PDF shift and shape
B -background	11.2	variation of fractions
Fitting procedure	14.4	bias observed in full MC fits
Sub-total:	21.1	events
Total Systematic Error	17.0%	
Branching Fraction	$(10.9 \pm 1.9 \pm 1.9) \times 10^{-6}$	

Table 4.7: *The breakdown of systematic uncertainty for $B^\pm \rightarrow \rho^\pm \pi^0$ branching fraction measurement.*

A_{CP}	0.24	fit to data and sign-flip
Statistical Error on A_{CP}	0.16	parabolic error from fit
	Fit systematics	
B Tagging	0.004	parameters from BReco
Fraction of SCF($\pm 10\%$)	0.006	parameter variation
Mischarge Fraction($\pm 5\%$)	0.002	parameter variation
ΔE PDF	0.021	PDF shift and shape
m_{ES} PDF	0.003	PDF shift and shape
NN PDF	0.0	PDF shift and shape
B -background	0.050	variation of fractions
Total Systematic Error:	0.06	Charge asymmetry
A_{CP}	$(0.24 \pm 0.16 \pm 0.06)$	

Table 4.8: *The breakdown of systematic uncertainty for $B^\pm \rightarrow \rho^\pm \pi^0$ charge asymmetry measurement.*

Chapter 5

Study of $B^\pm \rightarrow \rho^0 \pi^\pm$ Decay

5.1 Introduction

Both CLEO [38] and Belle [39] have previously published observations of the $B^\pm \rightarrow \rho^0 \pi^\pm$ decay. We will present an updated measurement with higher precision on the branching fraction and will investigate the CP -violating charge asymmetry. From a theoretical point of view, it is interesting for us to probe direct CP violation in $B^\pm \rightarrow \rho^0 \pi^\pm$ decays [31, 32, 33]. Reference [33] points out that the direct CP asymmetry in $B^\pm \rightarrow \rho^0 \pi^\pm$ could be as large as 30%–50% if the effect of ρ - ω mixing is included and the invariant mass of the $\pi^+ \pi^-$ pair is in the vicinity of the ω resonance.

In addition, it is well known that the ratio of branching fractions, R , as defined in Equation 5.1, is particularly interesting because the theoretical prediction varies over a wide range depending on the assumptions made in its calculation [34, 35, 30, 36]. The latest result from Belle shows [39]:

$$R \equiv \frac{\text{Br}(B^0 \rightarrow \rho^\pm \pi^\mp)}{\text{Br}(B^+ \rightarrow \rho^0 \pi^+)} = 2.6 \pm 1.1 \quad (5.1)$$

This is consistent with values obtained by CLEO [38]. Theoretical calculations done at tree level including factorization for the hadronic matrix element give $R \approx 6$ [30]. Calculations that include penguin contributions, off-shell B^* excited states or additional $\pi\pi$ resonances [36] yield better agreement with the measured value of R . So a precise measurement of the branching fraction will help us to clarify this puzzle and to constrain the magnitude of the various form factors needed in the theoretical calculations in B decays.

5.2 Candidate Selection

In order to reconstruct the $\rho^0\pi^\pm$ final state, we loop over all the combinations of three charged **GoodTracksLoose** track candidates, and combine them into a list of B -candidates. To further improve the signal-to-background ratio, candidates which pass the preselection must satisfy additional requirements:

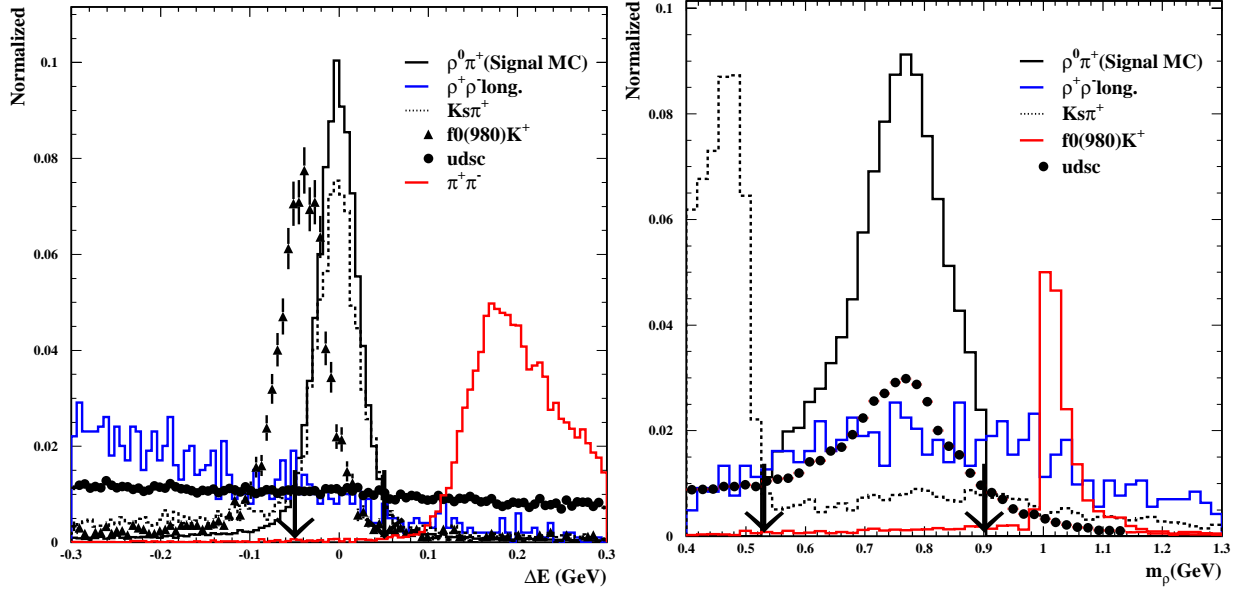


Figure 5.1: ΔE distributions (left) and $\pi^+\pi^-$ invariant mass (right) in the $B^\pm \rightarrow \rho^0\pi^\pm$ analysis for the various signal contributions and background processes. Indicated by the two arrows are the selection cuts.

- $5.23 < m_{\text{ES}} < 5.29 \text{ GeV}/c^2$.
- $-0.05 < \Delta E < 0.05 \text{ GeV}$. The left plot in Figure 5.1 shows ΔE distributions for the signal and various background processes.
- Candidate events should have at least one invariant mass combination, $m(\pi^+\pi^-)$ within the following range: $0.53 < m(\pi^+\pi^-) < 0.9 \text{ GeV}/c^2$. The right plot in Figure 5.1 shows the $\pi^+\pi^-$ mass for the various signal and background processes.
- The helicity angle of the ρ candidates must satisfy $|\cos\theta_H(\rho)| > 0.25$.
- The absolute time interval cut, $|\Delta t| < 20 \text{ ps}$.
- The error on Δt must satisfy $\sigma_{\Delta t} < 2.5 \text{ ps}$.
- All of the three signal tracks must fail the tight electron ID, the tight Kaon ID and the tight proton ID.
- The continuum-fighting Neural Network (NN) cut, $0.6 < \text{NN} < 1.0$. The NN is built using the six discriminating variables: $m(\rho)$, $\cos\theta_H(\rho)$, L_0 , L_2 , $\cos\theta_{B,z}$ and $\cos\theta_{T_B,z}$.
- The number of signal photons in the DIRC associated with the track of the bachelor hadron(the one which is not used for ρ^0 reconstruction) should be no less than 5. This requirement implies the restriction to the DIRC geometrical acceptance.
- In order to remove $B \rightarrow D^0 X$, $D^0 \rightarrow K\pi$ or $\pi\pi$ background, the invariant mass $m_{K\pi}$ or $m_{\pi\pi}$ should be outside $[1.844, 1.884] \text{ GeV}$.

All cut efficiencies for signal $B^\pm \rightarrow \rho^0 \pi^\pm$ Monte Carlo, data, uds MC samples are shown in Table 5.1.

Cut description	$\epsilon_{\rho\pi}^{\text{MC}}, [\%]$	$\epsilon_{\text{on}}^{\text{Data}}$	$\epsilon_{\text{off}}^{\text{Data}}$	$\epsilon_{\text{uds}}^{\text{MC}}$	$\epsilon_{c\bar{c}}^{\text{MC}}$	$\epsilon_{\tau^+\tau^-}^{\text{MC}}$
Reconstruction	78.2	-	-	5.1	5.9	1.7
$-0.05 < \Delta E < 0.05$ GeV	78.2	18.3	18.1	18.9	17.5	15.9
$5.23 < m_{\text{ES}} < 5.29$ GeV/ c^2	98.6	44.5	45.7	45.7	42.7	45.7
electron veto	98.2	88.5	88.6	94.9	90.7	75.5
kaon veto	95.9	58.4	58.5	66.5	39.6	90.6
proton veto	99.2	86.2	86.2	77.9	87.7	98.7
$N_\gamma^{\text{DIRC}} \geq 5$ (Bachelor)	86.3	81.2	80.5	80.7	77.4	83.3
$\Delta t < 20$ ps	99.6	97.4	97.4	97.9	97.0	97.5
$\sigma(\Delta t) < 2.5$ ps	97.0	89.5	92.4	92.4	89.1	80.9
$0.53 < m_\rho < 0.9$ GeV/ c^2	76.5	31.8	32.1	31.1	27.0	50.6
$ \cos\theta_H(\rho) < 0.25$	98.2	73.8	74.1	76.0	73.2	72.4
NN Cut	85.3	11.6	11.4	14.9	15.6	1.0
D^0 veto	97.4	98.1	97.7	97.8	98.1	100
Total(%)	29.0	-	-	$5.4 \cdot 10^{-3}$	$2.7 \cdot 10^{-3}$	$1.9 \cdot 10^{-4}$

Table 5.1: $\rho^0 \pi^\pm$ analysis: Summary of cut efficiencies for signal MC, data and uds MC samples. The efficiencies for each individual line of the table are given relative to the number of events retained after passing the skim cuts; they don't include the loss of events from the previous cuts.

Approximately 7% of selected signal events have more than one candidate after full selection, and the average number of candidates per event is 1.1. The multiple candidates in $\rho^0 \pi^\pm$ are mainly due to the soft charged track in the B to vector pseudo-vector type of decays. The candidate is chosen with the reconstructed ρ^0 invariant mass closest to the PDG value. If there is more than one candidate with the same ρ^0 invariant mass, we select the first one.

In Table 5.2, we summarize the selection efficiencies, fraction of combinatorial background and mischarge rate obtained from Monte Carlo after the candidate selection as described in the preceding sections.

Decay mode	$\epsilon(\%)$	$f_{\text{scf}}(\%)$	$\omega_Q(\%)$
$\rho^0\pi^\pm$	29.04 ± 0.016	7.149 ± 0.024	0.227 ± 0.053

Table 5.2: *Signal efficiency, fraction of misreconstructed signal events (SCF) and mischarge rate of the candidate selection. The numbers are obtained from $B^\pm \rightarrow \rho^0\pi^\pm$ signal MC. The mischarge rate is to be understood as relative to the fraction of SCF so that the overall mischarge rate is 1.6%. The errors given are statistical only.*

5.3 Validation of ΔE and m_{ES}

$B^+ \rightarrow \bar{D}^0(K^+\pi^-)\pi^+$ events can provide important information for the study of $B^\pm \rightarrow \rho^0\pi^\pm$ decays. Like $B^0 \rightarrow D^-\rho^+$ events, it has a large branching fraction, and more importantly, it has exactly three charged tracks in the final state as does $B^\pm \rightarrow \rho^0\pi^\pm$. This feature enables us to measure the distributions of B -related quantities, such as m_{ES} and ΔE , precisely from the data. The selection of $D^0\pi^\pm$ events is similar to the selection of $\rho^0\pi^\pm$ events with the following D mass cut instead of the ρ mass cut:

- $|m_D - 1.864| < 0.02 \text{ GeV}/c^2$,

where 1.864 is the nominal D^0 mass from the PDG. A likelihood fit was performed on the $\bar{D}^0\pi^+$ sample using m_{ES} , ΔE , Δt with both signal and continuum components floating and B -background fixed to the Monte Carlo expectation.

Table 5.3 shows some fit results from $\bar{D}^0\pi^+$ data and Monte Carlo, compared with the fitted results from $\rho^0\pi^\pm$ Monte Carlo. All of them are consistent each other. We find the relative shift of -3.63 MeV for ΔE between data and Monte Carlo in

$B^+ \rightarrow \bar{D}^0(K^+\pi^-)\pi^+$, the ratio of the width of ΔE between data and MC is 1.01, and the ratio of the width of m_{ES} between data and MC is 0.98. The summary of the data-MC difference can be found in Table 5.4. The assumption is made that these shifts can be related to $\rho^0\pi^\pm$ data and Monte Carlo. These numbers will be used in the evaluation of systematic uncertainties on the fitted $\rho^0\pi^+$ yield.

Parameters	$\bar{D}^0\pi^+$ data	$\bar{D}^0\pi^+$ MC	$\rho^0\pi^+$ MC
$\langle\Delta E\rangle$ MeV	-5.03 ± 0.33	-1.40 ± 0.13	-1.15 ± 0.14
$\sigma(m_{ES})$ MeV/ c^2	2.47 ± 0.03	2.52 ± 0.01	2.42 ± 0.01
$\sigma(\Delta E)$ MeV	18.77 ± 0.28	18.51 ± 0.09	20.53 ± 0.10

Table 5.3: *Summary of the results extracted from the $\bar{D}^0\pi^+$ fit.*

Parameters	$\sigma(m_{ES})_{\text{data}}/\sigma(m_{ES})_{\text{MC}}$	$\delta\langle\Delta E\rangle$ (MeV)	$\sigma(\Delta E)_{\text{data}}/\sigma(\Delta E)_{\text{MC}}$
$B^\pm \rightarrow D^0\pi^\pm$	0.98 ± 0.01	-3.63 ± 0.35	1.01 ± 0.02

Table 5.4: *Summary of the validation on the kinematic variables extracted from $\bar{D}^0\pi^+$ fit.*

5.4 Backgrounds from B Decays

The number of expected events from dominant B -background modes is obtained from Monte Carlo simulation and can be found in Table 5.5.

The branching fractions for various B -backgrounds have been described in chapter 4. For $B^+ \rightarrow \pi^+ f_0(980) \rightarrow \pi^+\pi^-\pi^+$ decay mode, the branching ratio has not been measured and there are no reliable theoretical arguments that could be used to infer it from other measurements. Although a tighter cut on $m_{\pi^+\pi^-}$ will remove most of them, the selection efficiency of this mode is still 1.2%. Of primary concern is the possible interference between this channel and our signal. An independent branching fraction

measurement $B^+ \rightarrow \pi^+ f_0(980) \rightarrow \pi^+ \pi^- \pi^+$ is performed. The resulting upper limit is given in Table 5.5. Here, we neglect this contamination because of the production rate of $\pi^+ f_0(980)$ is tiny in this analysis. The possible interference effect between ρ^0 and $f_0(980)$ will be discussed in detail in section 5.8 in detail.

Another possible contamination is from $B^+ \rightarrow \sigma^0 \pi^+$, where σ^0 is a very broad S-wave resonance with a mass around 500 MeV, with a width of about 300-400 MeV [41], and which decays into a $\pi^+ \pi^-$ final state. Since we know very little about the σ resonance, a 2-variable NN fit is performed in order to understand the contamination from $B^+ \rightarrow \sigma^0 \pi^+$. In this new fit, we remove the ρ information from the neural network, and use only event shape variables, L_0 and L_2 as input variables to the neural network. Two fits were done. One fit to the onpeak data sample with m_{ES} , ΔE and 2-variable NN, the other fit to onpeak data with an additional discriminant, m_ρ . We found only 6.2 events difference between the two fits. There is no significant change on the signal yield after we add the ρ information. So we can conclude that the signal events from onpeak data fit is consistent with pure ρ resonance. Hence, we assume that the contamination from this mode is negligible.

The non-resonant contribution can in principle occur for all pionic and kaonic $B \rightarrow 3/4$ -body final states. The selection efficiency in this analysis is very small (2.3%) due to cuts on the $\pi^+ \pi^- \pi^+$ Dalitz plot. At the same time, the branching fraction of inclusive $B^+ \rightarrow \pi^+ \pi^- \pi^+$ decay has been measured at *BABAR* [40] to be $(10.9 \pm 3.9) \times 10^{-6}$. The current world-average-value of the branching fraction of $B^+ \rightarrow \rho^0 \pi^+$ is 9.0×10^{-6} , it can be concluded that the inclusive $B^+ \rightarrow \pi^+ \pi^- \pi^+$ decay is dominated by $\rho^0 \pi^+$ decays. Additionally, the same 2-variable NN test results indicate that there

is no significant S-wave contribution from other sources to the fitted signal yield. Thus we assume the measured signal events contain only ρ^0 resonance.

No attempt is made to group B -backgrounds into 2, 3 and 4-body modes as the total number of contributing modes are not enormous. Instead all of them are treated individually. The ΔE , m_{ES} and NN distributions were parametrized by empirical PDF. ΔE and m_{ES} correlation in B -background is investigated by using a 2-dimensional PDF. No significant difference is observed by switching two one dimensional PDFs to one two dimensional PDF, therefore, for the purpose of simplicity, one dimensional PDFs are used for B -background throughout this analysis.

In Table 5.5, we list the various background modes and the number of expected events corresponding to a data sample of 81.9 fb^{-1} . In the nominal fit we assumed a charge asymmetry of zero for both charged and neutral background modes. A possible non-zero asymmetry is taken into account when the systematic errors from the uncertainties of B -background charge asymmetries are estimated.

5.5 Systematic Uncertainty due to B -background

The principle and detailed procedure of the evaluation of the B -background systematic error is described in Chapter 4. The systematic errors due to imperfect B -background modeling are summarized in Table 5.6.

5.6 Maximum Likelihood Fit

The likelihood function is similar to the one used in Chapter 4. It is found that tagging category information does not bring addition sensitivity to this analysis due to the clean signal in the data. Thus for simplicity no tagging category related

Cl	Mode	BR(10^{-6})	Eff.(%)	N_{exp}
0	$B^+ \rightarrow \rho^+ \rho^0$ long	30.1 ± 9.0	0.296	7.9 ± 2.4
0	$B^+ \rightarrow \eta'(\eta' \rightarrow \rho^0 \gamma) K^+$	21.4 ± 1.7	0.035	0.7 ± 0.1
0	$B^+ \rightarrow \eta'(\eta' \rightarrow \rho^0 \gamma) \pi^+$	$3.0 \pm 2.0^*$	0.838	2.2 ± 1.5
1	$B^+ \rightarrow K^{*0}(K\pi)\pi^+$	10.3 ± 2.6	1.228	11.1 ± 2.8
1	$B^+ \rightarrow K^+ \rho^0$	3.9 ± 1.2	1.439	4.9 ± 1.5
1	$B^+ \rightarrow K_s^0(\pi^+ \pi^-) \pi^+$	9.0 ± 0.9	0.668	5.3 ± 0.5
1	$B^+ \rightarrow K^+ f_0(980)$	11.7 ± 4.0	0.108	1.1 ± 0.4
1	$B^+ \rightarrow \pi^+ \omega(\pi^+ \pi^-)$	0.14 ± 0.04	29.0	3.6 ± 1.0
1	$B^+ \rightarrow \pi^+ f_0(980)$	1.2^*	1.170	1.8
2	$B^0 \rightarrow \rho^+ \rho^-$ long	$40^{+50}_{-35}^*$	0.179	$6.3^{+7.8}_{-5.5}$
2	$B^0 \rightarrow \rho^0 \rho^0$ long	$3.5 \pm 3.5^*$	0.537	1.7 ± 1.7
2	$B^0 \rightarrow a_1^+ \pi^-$	$35 \pm 35^*$	0.173	5.3 ± 5.3
3	$B^0 \rightarrow \rho^\pm \pi^\mp$	22.6 ± 2.8	1.435	29.3 ± 5.2
3	$B^0 \rightarrow \rho^+ K^-$	7.3 ± 1.8	0.174	1.1 ± 0.3
3	$B^0 \rightarrow K^{*+}(K^+ \pi^0) \pi^-$	8.7 ± 5.0	0.185	1.4 ± 0.8
4	$B^+ \rightarrow (K_X^{(**)} \pi)^+$	$40 \pm 26^*$	0.082	2.9 ± 1.9
4	$B^0 \rightarrow (K_X^{(**)} \pi)^0$	$72 \pm 54^*$	0.117	7.4 ± 5.5
Total Charmless				92.2 ± 11.3
5	$B^+ \rightarrow \text{charm}$	-	-	54.1 ± 7.4
6	$B^0 \rightarrow \text{charm}$	-	-	19.2 ± 4.4

Table 5.5: *Classification of background from charged and neutral Bs. The branching fractions were obtained from ref. [37], efficiencies and expected event yields are obtained from MC. The errors on the event yields mainly reflect the uncertainties on the branching fractions. The asterisk corresponds to modes where the branching ratio is estimated from theoretical argument in ref. [37]. Only the modes that have at least one event in either channel are listed.*

Mode	BR-variation		\mathbf{A}_{CP} -variation	
	ΔN_{sig}	$\Delta A_{CP}^{\text{sig}} [\%]$	ΔN^{sig}	$\Delta A_{CP}^{\text{sig}} [\%]$
$B^+ \rightarrow \rho^+ \rho^0 \text{long}$	0.17	0.03	0.04	0.23
$B^+ \rightarrow \eta'(\eta' \rightarrow \rho^0 \gamma) K^+$	0.00	0.00	0.00	0.00
$B^+ \rightarrow \eta'(\eta' \rightarrow \rho^0 \gamma) \pi^+$	0.31	0.05	0.05	0.23
$B^0 \rightarrow \rho^+ \rho^- \text{long}$	0.19	0.03	0.04	0.00
$B^0 \rightarrow \rho^0 \rho^0 \text{long}$	0.04	0.01	0.01	0.00
$B^+ \rightarrow K^{*0}(K\pi)\pi^+$	1.80	0.13	0.53	1.75
$B^+ \rightarrow K^+ \rho^0$	0.87	0.19	0.16	0.72
$B^+ \rightarrow K_S^0(\pi^+ \pi^-)\pi^+$	0.13	0.01	0.03	0.29
$B^+ \rightarrow K^+ f_0(980)$	0.11	0.01	0.01	0.07
$B^0 \rightarrow \rho^\pm \pi^\mp$	0.94	0.10	0.31	0.00
$B^0 \rightarrow \rho^+ K^-$	0.06	0.00	0.01	0.00
$B^0 \rightarrow a_1^\pm \pi^\mp$	0.18	0.04	0.04	0.21
$B^0 \rightarrow K^{*+}(K^+ \pi^0)\pi^-$	0.32	0.02	0.01	0.00
$B^+ \rightarrow (K_X^{**} \pi)^+$	0.19	0.04	0.02	0.19
$B^0 \rightarrow (K_X^{**} \pi)^0$	0.06	0.02	0.03	0.21
$B^+ \rightarrow \text{charm}$	0.29	0.02	0.13	1.15
$B^0 \rightarrow \text{charm}$	0.15	0.01	0.01	0.15
Total	2.3	0.27	0.66	2.2

Table 5.6: *Systematic errors due to the uncertainties of B-background branching fractions and possible charge asymmetries in $B^\pm \rightarrow \rho^0 \pi^\pm$ analysis.*

information is used in likelihood fit.

5.7 Fit Results

The result of the final fit to the data of 81.9 fb^{-1} is shown in Table 5.7. Figure 5.2 and Figure 5.3 show the distributions of m_{ES} , ΔE and NN for data samples that are enhanced in signal, using cuts on the signal-to-continuum likelihood ratios of the discriminating variables that are not being plotted.

Due to the possible existence of a scalar contribution to the same final state, additional care is taken in this analysis. One way of looking at the problem is to repeat

Parameter	Description	Value
N_{signal}	Number of fitted $B^\pm \rightarrow \rho^0 \pi^\pm$ events	243.1 ± 26.5
A_{CP}^{signal}	CP asymmetry in fitted $B^\pm \rightarrow \rho^0 \pi^\pm$ sample	-0.19 ± 0.11
$\mu(\Delta E)$	Mean of core gaussian in signal ΔE PDF GeV	-0.001 ± 0.003
$\mu(m_{ES})$	Center of CB function in signal m_{ES} PDF GeV/c^2	5.2803 ± 0.0003
N_{cont}	Number of continuum events	8141.8 ± 93.3
ξ	Continuum Argus shape parameter	-30.8 ± 1.9
ΔE_{p1}	Slope of continuum ΔE distribution	-0.89 ± 0.39
β_1	Continuum NN parameter	5.49 ± 0.81
β_2	Continuum NN parameter	0.75 ± 0.17
β_3	Continuum NN parameter	1.45 ± 0.03

Table 5.7: *Summary of the final $B^\pm \rightarrow \rho^0 \pi^\pm$ fit result.*

the analysis without making any assumption about the intermediate resonance, and then look at the distribution of signal on the Dalitz plot, *i.e.* $m(\rho)$ and $\cos\theta_H(\rho)$.

A detailed study that does not use any ρ related information was carried out. In addition the m_{ES} and ΔE which are still kept in the analysis, the six-variable-NN is replaced with a two-variable-NN that contains only the event shape variables, L_0 and L_2 . The new fitted signal yield is compatible with the nominal fit result where the ρ related quantities are used. The ρ mass and helicity distributions in the signal enhanced region can be adequately described by a $B^\pm \rightarrow \rho^0 \pi^\pm$ signal, as shown in Figure 5.4.

5.8 Study of the Systematic Uncertainties

Corrections and Uncertainties on Signal Efficiency

Corrections and uncertainties that we need to apply for each component of the signal efficiency are:

- Following the *BABAR* recipe, we find that tracking efficiency in Monte Carlo needs

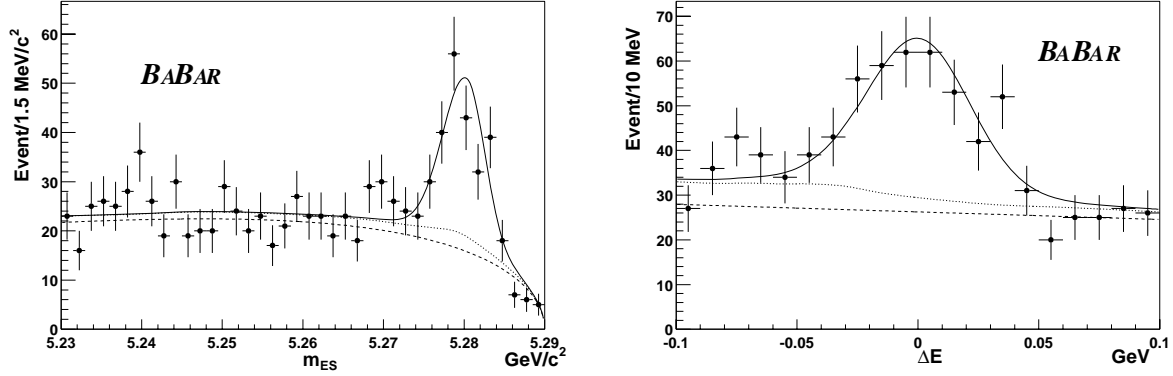


Figure 5.2: Distributions of m_{ES} , ΔE distributions for samples enhanced in $\rho^0\pi^\pm$ signal using likelihood ratio cuts. The solid curve represents a projection of the maximum likelihood fit results. The dashed curve represents the contribution from continuum events, and the dotted line indicates the combined contributions from continuum events and B -backgrounds. For demonstration purpose, we loosened the ΔE cut from $-0.05 < \Delta E < 0.05$ GeV to $-0.1 < \Delta E < 0.1$ GeV, and repeat the fit to get ΔE distribution.

to be scaled by an average factor of 0.975. We also assign a 0.8% systematic error for each track, which gives a total systematic error of 2.4%.

- PID killing for the tracks is performed according to the standard *BABAR* recipe. It results in a 5.2% relative change in the signal Monte Carlo efficiency which is assigned as a systematic error.
- Uncertainties on the ΔE and m_{ES} cuts is evaluated by comparing the difference between data and MC from Breco data sample (see Section 5.3).
- The uncertainty on the NN cut is similarly obtained from control samples. Due to the use of ρ related information in NN we use $B^0 \rightarrow D^-\rho^+$ as the control sample.

Uncertainties in the Signal Yield and Charge Asymmetry

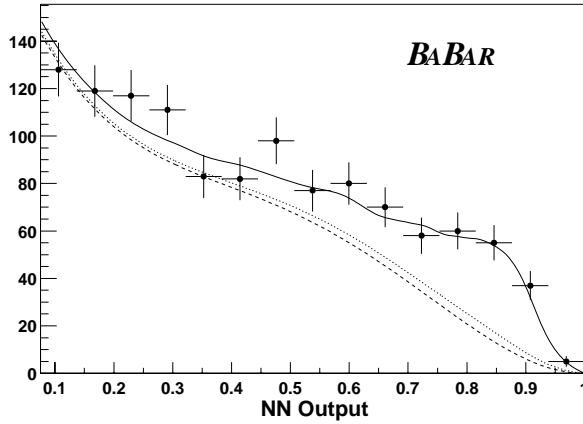


Figure 5.3: *Distribution of NN output for sample enhanced in $\rho^0\pi^\pm$ signal using likelihood ratio cut.*

The final state of this channel consists of three charged tracks. The sources of the systematic uncertainties are listed below:

- **SCF fraction:** The SCF fraction is very small(7.1%) in this analysis. It is varied by 5% to take into account the uncertainty of this quantity due to data and Monte Carlo difference. The variation on the signal yield and A_{CP} was taken as the systematic error.
- **Mischarge rate:** Also varied by 5%.
- **m_{ES} and ΔE PDFs:** Uncertainties taken from Section 5.3 is used to smear the ΔE and m_{ES} PDFs. The fit is redone with the smeared PDF and the difference in the fit result gives the uncertainty related to m_{ES} and ΔE .
- **NN PDF:** Systematic uncertainty due to the NN PDF can be evaluated using the correction function from the same $B^0 \rightarrow D^-\pi^+$ sample.
- **B -background:** The B -background modeling is one of the main sources of

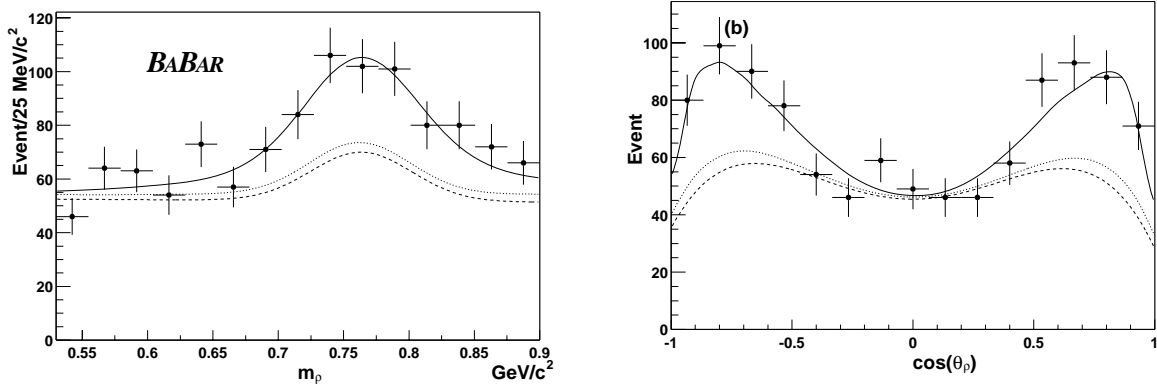


Figure 5.4: *Distributions of $m(\rho)$ and $\cos\theta_H(\rho)$ for samples enhanced in $\rho^0\pi^\pm$ signal using likelihood ratio cuts.*

systematic in the $B^\pm \rightarrow \rho^0\pi^\pm$ analysis. An estimation of this uncertainty is described in detail in Section 5.5.

To find the total systematic uncertainty on the signal yield and A_{CP} , these individual contributions are added in quadrature. The effects of these systematic uncertainties can be found in Table 5.8 and Table 5.9 respectively.

Uncertainties from Interference Effect

Besides ρ^0 , a few other resonances, namely, $f_0(980)$ and σ^0 , also decay dominantly into $\pi^+\pi^-$ final states. The interference between these resonances and ρ^0 may cause a considerable effect on the $B^\pm \rightarrow \rho^0\pi^\pm$ branching fraction measurement. Fortunately, the intrinsic interference between vector particles(ρ^0) and scalar particles($f_0(980)$, σ^0) is zero if one integrates over the entire helicity angle. Therefore, we only take into account the direct contribution from other resonances as if no interference ever happened.

5.9 Summary

We have measured the $B^\pm \rightarrow \rho^0 \pi^\pm$ branching fraction and its direct CP violating charge asymmetry A_{CP} using a maximum likelihood method. The results are obtained from a data sample with a total integrated luminosity of 81.9 fb^{-1} collected at the $\Upsilon(4S)$ resonance and 9.5 fb^{-1} taken 40 MeV below the $\Upsilon(4S)$ resonance in the (2000-2002) period by the *BABAR* detector at the PEP-II asymmetric-energy B factory at SLAC. The measured branching fraction is $(9.5 \pm 1.1(\text{stat.}) \pm 0.8(\text{syst.})) \times 10^{-6}$ and the CP violating charge asymmetry is $-0.19 \pm 0.11(\text{stat.}) \pm 0.02(\text{syst.})$. No evidence for direct CP violation in $B^\pm \rightarrow \rho^0 \pi^\pm$ decays is found.

	$B^+ \rightarrow \rho^0 \pi^+$	Comments
Signal yield and efficiencies		
Corrected N_{signal}	237.9	fit to data
ϵ_{signal}^{raw}	$(29.0 \pm 0.1)\%$	Signal MC
ϵ_{signal}	$(28.3 \pm 0.1)\%$	tracking eff. correction
Statistical Error	26.5	Parabolic error from fit
Efficiency and scaling systematics, [%]		
Tracking	2.4	per-track-corrections
PID for tracks	5.2	PID killing AWG recipe
ΔE cut eff.	1.0	BReco-vs-MC
m_{ES} cut eff.	0.0	BReco-vs-MC
NN cut eff.	4.0	BReco-vs-MC
$N_{\gamma}^{DIRC} > 5$ cut eff.	1.0	PIDReco-vs-MC
$N(B\bar{B})$	1.1	B-counting
Sub-total	7.2%	
Fit systematic		
Fraction of SCF($\pm 5\%$)	1.3	parameter variation
Mischarge Fraction($\pm 5\%$)	0.1	parameter variation
ΔE PDF	0.7	PDF shift and shape
m_{ES} PDF	1.6	PDF shift and shape
NN PDF	3.2	PDF shift and shape
Fitting procedure	8.2	Bias in MC fits
B -Background	2.3	variation of B -bkg parameters
Sub-total	9.3	absolute systematic from fit
Total Systematic error	19.5	total absolute systematic error
Branching fraction	$(9.5 \pm 1.1 \pm 0.8) \times 10^{-6}$	

Table 5.8: Summary of the systematic errors on the fitted signal yield in $B^{\pm} \rightarrow \rho^0 \pi^{\pm}$.

A_{CP}	-0.19	fit to data
Statistical Error	0.11	Parabolic error from fit
Fit systematic		
Fraction of SCF($\pm 5\%$)	0.0012	parameter variation
Mischarge Fraction($\pm 5\%$)	0.0001	parameter variation
ΔE PDF	0.0004	PDF shift and shape
M_{ES} PDF	0.0016	PDF shift and shape
NN PDF	0.0028	PDF shift and shape
B -background	0.0222	variation of fractions and CP parameters
Detector Charge Bias	0.009	estimate
Sub-total	0.024	

Table 5.9: Summary of the systematic errors on the fitted charge asymmetry in $B^{\pm} \rightarrow \rho^0 \pi^{\pm}$ analysis.

Chapter 6

Study of $B^0 \rightarrow \rho^0 \pi^0$ Decay

6.1 Introduction

The channel $B^0 \rightarrow \rho^0 \pi^0$ itself is of interest for many reasons: it is a charmless color-suppressed mode, and thus there is little experimental data which could highlight the underlying processes of such decays. Naive color-counting arguments lead one to expect the branching fraction of a color-suppressed mode to be $1/9$ that of a corresponding non color-suppressed mode. Final state interactions, or the presence of normally sub-leading diagrams, can dramatically modify this naive picture. Computing the branching fractions as a function of some dynamical parameter N_c^{eff} or *effective number of colors*, one finds the ratio of the branching fraction of $B^0 \rightarrow \rho^\pm \pi^\mp$ to the branching fraction of $B^0 \rightarrow \rho^0 \pi^0$ to be between 3.5 and 70 [42]. More importantly, if $B^0 \rightarrow \rho^0 \pi^0$ is found to be less suppressed than expected, it will be a key component in the $\pi^+ \pi^- \pi^0$ Dalitz plot analysis [20]. Even if it cannot be used in the Dalitz plot analysis, the $B^0 \rightarrow \rho^0 \pi^0$ branching fraction can be used to constrain $|\alpha_{\text{true}} - \alpha_{\text{eff}}|$, where α_{eff} is measured in the Dalitz plot analysis with $B^0 \rightarrow \rho^\pm \pi^\mp$ [21].

Only 90% CL upper limits have been set on $B^0 \rightarrow \rho^0 \pi^0$ by CLEO [38], 5.1×10^{-6}

(on 9.7×10^6 $B\bar{B}$ pairs) and by Belle [39], 5.3×10^{-6} (on 31.9×10^6 $B\bar{B}$ pairs).

Technically speaking, the difficulties induced by small branching fractions are mainly two-fold. First, the signal to continuum background ratio, is much smaller than in the other $B \rightarrow \rho\pi$ analyses. Second, the signal will be highly polluted by other intermediate states leading to the same $\pi^+\pi^-\pi^0$ final state. ($B^0 \rightarrow \rho^\pm\pi^\mp$ is one such channel, but other intermediate states such as $B^0 \rightarrow f_0\pi^0$ also contribute.) B -related modes leading to other final states will also contaminate the signal, as in other $B \rightarrow \rho\pi$ analyses.

In the present analysis, we choose to not look at the interfering parts of the $\pi^+\pi^-\pi^0$ Dalitz plot. To study these interference regions requires a more involved analysis that will be described later. This analysis studies only the central region of the ρ^0 band. The ρ polarization feature depopulates this region, which decreases the analysis' sensitivity. Still, we may have enough sensitivity to discover an enhanced $B^0 \rightarrow \rho^0\pi^0$ signal outside the interfering region.

The analysis proceeds in two steps. We first measure the $B^0 \rightarrow \rho^0\pi^0$ yield to obtain its branching fraction. If the signal is significant enough we perform a time-dependent CP analysis. $B^0 \rightarrow \rho^0\pi^0$ is a CP eigenstate; its time-dependent probability density function (PDF) is given by:

$$f_{B^0 \text{ tag}} = \frac{e^{-|\Delta t|/\tau}}{4\tau} \left[1 + \frac{\Delta D_{c_{\text{tag}}}}{2} + \langle D \rangle_{c_{\text{tag}}} (S \sin(\Delta m_d \Delta t) - C \cos(\Delta m_d \Delta t)) \right] \quad (6.1)$$

$$f_{\bar{B}^0 \text{ tag}} = \frac{e^{-|\Delta t|/\tau}}{4\tau} \left[1 - \frac{\Delta D_{c_{\text{tag}}}}{2} - \langle D \rangle_{c_{\text{tag}}} (S \sin(\Delta m_d \Delta t) - C \cos(\Delta m_d \Delta t)) \right] \quad (6.2)$$

where c_{tag} is the tagging category of the tagging B , $\langle D \rangle_{c_{\text{tag}}}$ and $\Delta D_{c_{\text{tag}}}$ are the average dilution factor and tag-asymmetry dilution in the tagging category c_{tag} . CP violation

would be established if $C \neq 0$ (direct CP violation) or $S \neq 0$ (CP violation induced by the interference between decay with and without mixing). This latter parameter is linked to $\sin 2\alpha$.

6.2 Selection

The following event selection is performed in order to select $B^0 \rightarrow \rho^0 \pi^0$ events.

- $0.01 < \text{LAT}_\gamma < 0.6$
- $E_{\gamma, \text{LAB}} > 0.05 \text{ GeV}$
- Only π^0 s constructed from resolved $\gamma\gamma$ are used, $0.11 < m(\pi^0) < 0.16 \text{ GeV}/c^2$
- $0.53 < m(\pi^+ \pi^-) < 0.9 \text{ GeV}/c^2$
- $|\cos \theta_H(\rho)| > 0.25$
- Veto of $B^0 \rightarrow \rho^\pm \pi^\mp$ events, *i.e.* we reject the candidate if it passes: $0.4 < m(\pi^+ \pi^0) < 1.3 \text{ GeV}/c^2$ or $0.4 < m(\pi^- \pi^0) < 1.3 \text{ GeV}/c^2$
- Two body veto to remove $B^+ \rightarrow \pi^+ \pi^0$ and $B^+ \rightarrow K^+ \pi^0$: $m(\pi^\pm \pi^0) < 5.14 \text{ GeV}/c^2$
- $5.23 < m_{\text{ES}} < 5.2875 \text{ GeV}/c^2$
- $-0.15 < \Delta E < 0.10 \text{ GeV}$
- PID cuts: both tracks must fail the **Tight** electron, proton and kaon IDs
- Time cut: $|\Delta t| < 20 \text{ ps}$ and $\sigma_{\Delta t} < 2.5 \text{ ps}$
- Continuum-fighting NN cut. The NN is built using the six discriminant variables:
 $m(\rho), \cos \theta_H(\rho), L_0, L_2, \cos \theta_{B,z}, \cos \theta_{T_B,z}$.

Table 6.1 summarizes the efficiency of each cut when applied to signal Monte Carlo, continuum Monte Carlo, off-peak data and on-peak “sideband” data. The tables show good agreement between continuum Monte Carlo, off-peak and on-peak-“sideband”.

Cut description	$\epsilon_{\rho^0\pi^0}^{\text{MC,Corr}} [\%]$	$\epsilon_{\rho^0\pi^0}^{\text{MC,Uncorr}}$	$\epsilon_{\text{off}}^{\text{data}}$	$\epsilon_{\text{on(SB)}}^{\text{data}}$	$\epsilon_{\text{udsc}}^{\text{MC}}$
skim	52.9	58.1			4.0
track quality	99.8	99.8	99.7	99.7	99.7
$0.01 < \text{LAT}(\gamma) < 0.6$	97.2	97.7	92.3	92.1	92.4
$E_\gamma > 0.05 \text{ GeV}$	98.4	98.7	95.7	96.2	96.0
$0.11 < m(\pi^0) < 0.16$	97.9	98.1	96.1	96.4	96.3
$0.4 < m(\rho^0) < 0.9$	73.6	73.9	21.6	22.1	22.1
$0.25 < \cos\theta_H(\rho) $	98.4	98.4	80.9	81.4	82.1
$-0.15 < \Delta E < 0.1^*$	81.1	82.3	23.3	48.0	23.1
$5.23 < m_{ES} < 5.29^*$	99.4	99.4	44.3	60.3	42.4
$ \Delta t < 20 \text{ ps}$	98.9	98.9	94.1	93.0	93.5
$\sigma(\Delta t) < 2.5 \text{ ps}$	95.3	95.3	92.1	90.6	91.4
ρ^\pm veto	96.6	96.6	98.3	97.6	98.5
Two Body veto	99.9	99.9	100.	97.1	100.
electron veto	98.4	98.4	92.6	93.1	94.5
kaon veto	97.1	97.2	76.5	75.1	69.6
proton veto	99.5	99.5	94.1	94.6	92.0
NN Cut	81.1	81.2	6.97	7.61	6.89

Table 6.1: *Cut efficiencies for signal MC with π^0 killing and smearing corrections applied, signal MC without π^0 corrections, offpeak data, onpeak sidebands data ($m_{ES} < 5.23$ or $m_{ES} > 5.29$, and $\Delta E < -0.15$ or $\Delta E > 0.1$, as indicated by the “*”), and udsc MC. The table gives efficiencies for a cut relative to the previous cut. Note that MC tracking correction has not been applied.*

Approximately 8% of signal events that pass the selection have multiple B candidates, and on average, there are 1.1 candidates per event. Most (>90%) of these multi-candidate events have two B candidates. In case of such multiple candidates the candidate with ρ mass closest to the PDG value is selected.

Table 6.2 summarizes the final signal efficiency and background contamination in the data sample. The selection efficiency for signal is 20.2%, with a relative SCF fraction of 9.1%. For 1999, 2000, 2001 and 2002 data set (81.9 fb^{-1}), there are 7048 events that pass the selection and enter the likelihood fit.

Mode	ϵ (%)	f_{SCF} (%)
$B^0 \rightarrow \rho^0 \pi^0$	20.2 ± 0.1	9.1 ± 0.2

Table 6.2: *Summary of the selection efficiency of $B^0 \rightarrow \rho^0 \pi^0$.*

6.3 Backgrounds from B Decays

In total, we expect 73.6 charmless B -related background events and 59.0 charmed B -background events in the 81.9 fb^{-1} data sample after the full selection.

The criterion to retain a mode is that more than one event remains after the selection: according to this, 17 charmless modes plus generic charmed modes are retained. Those modes are classified according to their PDF shapes and CP properties. The classes are summarized in table 6.3.

6.4 Maximum Likelihood Fit

Since we are looking for a decay into CP eigenstate, we do not have the charge of the B decay included in the likelihood. We use the likelihood function defined in Equation 3.2 for this analysis.

Class	Mode	BR ($\times 10^{-6}$)	N _{exp}
9	$B^+ \rightarrow \rho^+ \rho_{\text{long}}^0$	$30.1^{+8.3*}_{-9.9}$	$15.7^{+4.4}_{-5.2}$
0	$B^0 \rightarrow \rho^+ \rho_{\text{long}}^-$	40.0^{+50*}_{-35}	$10.1^{+12.6}_{-8.8}$
1	$B^0 \rightarrow \eta'(\rho^0 \gamma) \pi^0$	$0.0 \pm 1.0^*$	$0.0^{+2.0}_{-0.0}$
2	$B^0 \rightarrow \pi^0 K^{*0}(K^+ \pi^-)$	0.0 ± 1.4	0.0 ± 2.1
11	$B^+ \rightarrow \rho^+ \pi^0$	15.0^{+15*}_{-10}	$15.0^{+15.0}_{-10.0}$
3	$B^0 \rightarrow K^{*0}(\rightarrow (K \pi)^0) \gamma$	40.2 ± 2.7	1.7 ± 0.1
18	$B^0 \rightarrow K_s^0(\rightarrow \pi^+ \pi^-) \pi^0$	3.5 ± 0.5	1.7 ± 0.2
4	$B^0 \rightarrow \rho^+ \pi^-$	11.3 ± 1.4	7.6 ± 0.9
5	$B^0 \rightarrow \rho^- \pi^+$	11.3 ± 1.4	8.6 ± 1.1
6	$B^0 \rightarrow \rho^- K^+$	7.3 ± 1.8	0.7 ± 0.2
12	$B^+ \rightarrow K^+ \pi^0$	12.7 ± 1.2	0.8 ± 0.1
13	$B^+ \rightarrow \pi^+ \pi^0$	5.8 ± 1.0	1.4 ± 0.2
14	$B^+ \rightarrow (K^{**} \pi)^+$	$40 \pm 26^*$	2.2 ± 1.4
15	$B^0 \rightarrow (K^{**} \pi)^0$	$72 \pm 54^*$	3.1 ± 2.3
10	$B^+ \rightarrow a_1^+(\rightarrow (\rho \pi)^+) \pi^0$	$35.0 \pm 25.0^*$	5.1 ± 3.6
7	$B^0 \rightarrow f_0 \pi^0$	$0.0 \pm 3.0^*$	$0.0^{+2.9}_{-0.0}$
8	$B^0 \rightarrow \pi^+ \pi^- \pi^0(\text{non} - \text{res})$	$0.0 \pm 5.0^*$	$0.0^{+3.7}_{-0.0}$
Sub-total	$B \rightarrow \text{charmless}$	-	74 ± 22
16	$B^0 \rightarrow \text{charm}$	-	21.0 ± 6.3
17	$B^+ \rightarrow \text{charm}$	-	38 ± 11
Total			132 ± 25

Table 6.3: *Classifications of major B-background modes. A “*” indicates that the branching fraction is estimated.*

6.5 Fit Results

This section discusses the result of the final fit on data. There are 7048 data events that pass the selection and enter the final fit. In the nominal fit, 18 parameters are floated; their fitted values are shown in Table 6.4. The signal yield is found to be $24.9 \pm 11.5(\text{stat.})$, with a significance of 2.8σ (computed as $\sqrt{-2 \ln(\mathcal{L}_{\text{null}}/\mathcal{L}_{\text{max}})}$). The total fitted continuum yield is 6892.6 ± 83.9 which agrees reasonably well with that estimated from off-peak data (6691 ± 340).

Parameter	Description	Value
$N_{\rho\pi}$	Number of $B^0 \rightarrow \rho^0\pi^0$ events	24.9 ± 11.5
$N_{B\rho\pi}^{\text{Lepton}}$	Number of continuum events in Lepton tag. cat.	24.3 ± 5.4
$N_{B\rho\pi}^{\text{Kaon}}$	Number of continuum events in Kaon tag. cat.	1616.5 ± 40.9
$N_{B\rho\pi}^{\text{NT1}}$	Number of continuum events in NT1 tag. cat.	331.3 ± 18.4
$N_{B\rho\pi}^{\text{NT2}}$	Number of continuum events in NT2 tag. cat.	1110.9 ± 33.6
$N_{B\rho\pi}^{\text{NoTag}}$	Number of continuum events in NoTag tag. cat.	3809.6 ± 62.2
ξ	Cont. ARGUS function slope	-23.3 ± 2.1
ΔE_{p1}^π	Cont. ΔE linear term	-0.67 ± 0.17
a_2	Cont. NN polynomial coefficient order 2	-0.058 ± 0.023
a_3	Cont. NN polynomial coefficient order 3	0.085 ± 0.022
a_4	Cont. NN polynomial coefficient order 4	-0.116 ± 0.020
a_5	Cont. NN polynomial coefficient order 5	0.081 ± 0.014
$\mu(\Delta t)_1$	Cont. 1st Gaussian mean of Δt Res.	0.043 ± 0.010
$\sigma(\Delta t)_1$	Cont. 1st Gaussian sigma of Δt Res.	1.089 ± 0.036
$\sigma(\Delta t)_2$	Cont. 2nd Gaussian sigma of Δt Res.	2.313 ± 0.301
$\sigma(\Delta t)_3$	Cont. 3rd Gaussian sigma of Δt Res.	12.339 ± 1.363
$f(\Delta t)_1$	Cont. 1st Gaussian fraction of Δt Res.	0.157 ± 0.048
$f(\Delta t)_2$	Cont. 2nd Gaussian fraction of Δt Res.	0.032 ± 0.005

Table 6.4: *The full $B^0 \rightarrow \rho^0\pi^0$ fit result on data.*

Figure 6.1 shows distributions of m_{ES} and ΔE enhanced in signal content by cuts on the signal-to-continuum likelihood ratios of the discriminating variables that are not being plotted. The agreement between data and Monte Carlo expectation is acceptable. No significant $B^0 \rightarrow \rho^0\pi^0$ signal is seen.

6.6 Systematic Uncertainties on the Signal Yield

Systematic Uncertainties Related to B -backgrounds

Two approaches are used to study the systematics on the yield due to uncertainties related to B -backgrounds. One is conventional: contributions to the systematic error by each B -background mode, obtained by varying its yield by one standard de-

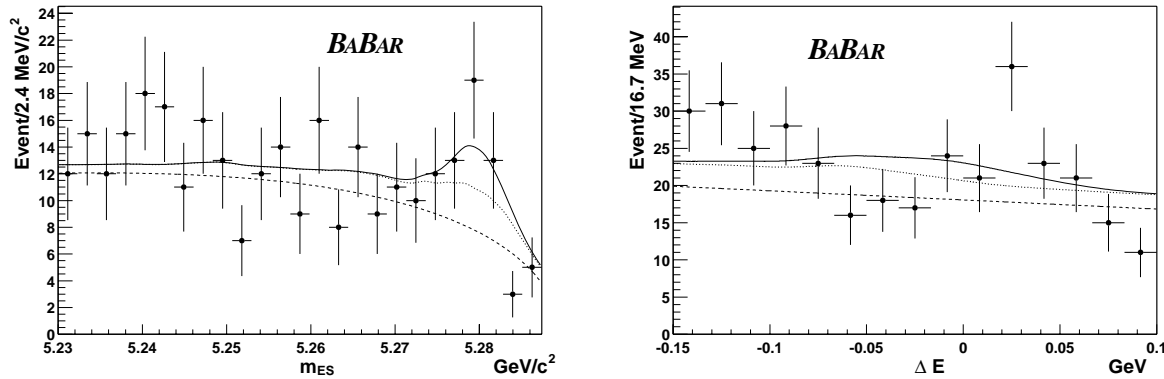


Figure 6.1: *Distributions of m_{ES} (left) and ΔE (right) for samples enhanced in $\rho^0\pi^0$ signal content using cuts on the signal-to-continuum likelihood ratio. The solid curves represent projections of the fit result. The dashed curves represent the contribution from continuum events, and the dotted lines indicate the combined contributions from continuum events and B backgrounds.*

viation. Table 6.5 shows the contribution from major B -background modes to the systematic uncertainty on the signal yield. The total error calculated with this approach is $^{+2.0}_{-3.3}$. All contributions are added quadratically. For unknown modes with only estimated branching fractions, the uncertainties are divided by $\sqrt{3}$ and taken as the standard deviations.

The other approach is used as a crosscheck. It is as follows:

1. Generate events according to PDF. In each generation, randomize B -background yields simultaneously. For a known branching fraction, we take the measured mean and uncertainty as the mean and width of a Gaussian randomization. For an estimated branching fraction, we take the mean and range to define a flat distribution.
2. Use these yields together with the rest of the nominal inputs, then fit back on this data set with the modified branching fraction and get a new signal yield.

Channel	ΔN
$B^+ \rightarrow \pi^+\pi^0$	+0.03 / - 0.03
$B^+ \rightarrow K^+\pi^0$	+0.02 / - 0.02
$B^0 \rightarrow \rho^+\pi^-$	+0.16 / - 0.11
$B^0 \rightarrow \rho^-\pi^+$	+0.17 / - 0.12
$B^0 \rightarrow \rho^-K^+$	+0.01 / - 0.03
$B^+ \rightarrow \rho^+\pi^0$	+1.02 / - 1.43
$B^0 \rightarrow K_S\pi^0$	+0.04 / - 0.04
$B^0 \rightarrow K^{*0}(K^+\pi^-)\pi^0$	+0.00 / - 1.44
$B^0 \rightarrow K^{*0}(K^+\pi^-)\gamma$	+0.03 / - 0.05
$B^0 \rightarrow (K^{**}\pi)^0$	+0.16 / - 0.10
$B^+ \rightarrow (K^{**}\pi)^+$	+0.05 / - 0.05
$B^0 \rightarrow \eta'(\rho^0\gamma)\pi^0$	+0.00 / - 0.76
$B^0 \rightarrow f_0(980)\pi^0$	+0.00 / - 0.33
$B^0 \rightarrow \pi^+\pi^-\pi^0$ (non-res)	+0.00 / - 1.91
$B^0 \rightarrow \rho^+\rho^-\text{long}$	+0.51 / - 0.67
$B^+ \rightarrow \rho^+\rho^0\text{long}$	+1.07 / - 0.77
$B^+ \rightarrow a_1^+\pi^0$	+0.35 / - 0.31
$B^0 \rightarrow \text{charm}$	+1.11 / - 1.00
$B^+ \rightarrow \text{charm}$	+0.31 / - 0.31
Total	+2.00 / - 3.26

Table 6.5: *Contributions to the signal yield uncertainty from each involved B-background mode. The positive contribution comes from varying a yield down by one standard deviation and the negative from varying up by one standard deviation. The results are obtained from fits to data.*

3. Use the unmodified nominal parameter set to fit on the same toy set again and get a signal yield.
4. The difference between results obtained in 2) and 3) has a distribution, of which the RMS (or width if Gaussian-like) is taken as the systematic uncertainty on signal yield due to uncertainties in B -background branching fractions.

With this approach, the systematic uncertainty due to B -background branching fraction uncertainties is found to be 4.5 events, in good agreement with the previous

approach.

Other Systematic Uncertainties from Likelihood Fit

Other sources of systematic uncertainties have been studied and the results are shown in table 6.6. The total contribution from these sources is 3.5 events.

Sources	Variation	ΔN
B^0 lifetime	1σ according to PDG	0.17
B^+ lifetime	1σ according to PDG	0.07
m_{ES} PDF	corrected according to BReco $D\rho$	1.29
ΔE PDF	corrected according to BReco $D\rho$	0.96
Tag. cat. efficiencies	1σ according to BReco or MC	0.15
Signal Δt resolution	1σ according to BReco measurements	0.34
Signal NN PDF	BReco $D\rho$ used to correct the PDF	2.21
SCF fraction	Varied by 5% relative	0.05
B -bkg tag. fractions	Statistic Uncertainties from MC	0.80
Fitting procedure	Fits to data-size MC chunks	2.02
Total		3.53

Table 6.6: Contributions to the $B^0 \rightarrow \rho^0 \pi^0$ signal yield uncertainty from sources other than B -background branching fractions.

Systematics due to Interferences

Interferences between $B^0 \rightarrow \rho^0 \pi^0$ and $B^0 \rightarrow f_0(980)\pi^0$ or $\sigma(400 - 1200)\pi^0$ occur at the level of decay amplitudes. While the decay $B^0 \rightarrow \rho^0 \pi^0$ is $S \rightarrow VP$, the decays $B^0 \rightarrow f_0(980)\pi^0$ or $\sigma(400 - 1200)\pi^0$ are both $S \rightarrow SP$. To conserve total angular momentum, the orbital angular momentum of SP must be $L = 0$ while that of VP must be $L = 1$. The total wave function of VP then has Y_1 (the spherical harmonic function) for the orbital angular momentum part and the total wave function of SP has Y_0 . Therefore the total wave functions of VP and SP are orthogonal when integrated over the whole phase space. With the above argument, it is expected the interferences

between $B^0 \rightarrow \rho^0 \pi^0$ and $B^0 \rightarrow f_0(980) \pi^0$ or $\sigma(400 - 1200) \pi^0$ are very small.

Interference between $B^0 \rightarrow \rho^0 \pi^0$ and $B^0 \rightarrow \rho^\pm \pi^\mp$ is negligible since we cut away the interference corners in the Dalitz plot.

Total Systematic Uncertainty

The total systematic uncertainty on yield is $^{+4.1}_{-4.8}$ events according to the previous studies. Since it is not too asymmetric, we simply take 4.8 as the total systematic uncertainty on the observed signal yield. The systematic uncertainties are summarized in Table 6.7.

6.7 Setting the Upper Limit on the Branching Fraction

Given the current levels of expected signal yield and background in this analysis, the final fit is not sensitive enough to actually measure the branching fraction for $B^0 \rightarrow \rho^0 \pi^0$. In this case, an upper limit on the branching fraction is set, using an approach similar to [43]. The method used for this analysis is outlined as follows:

1. Generate toy Monte Carlo with the nominal expected number of background events and a signal hypothesis, $\mu_s^{\text{input}} = \mu_s^{\text{expected}}$. This is done multiple times, and each toy Monte Carlo experiment is fitted for the signal yield, μ'_s . The collection of μ'_s forms a distribution, $D_{s+b}(\mu'_s, \mu_s^{\text{input}})$, for the original signal hypothesis.
2. Many toy Monte Carlo samples with a signal hypothesis of zero events and with the expected number of background events are also generated. Again, each data sample is fitted and we obtain the distribution of the fitted signal yield, $D_b(\mu'_s, 0)$.
3. For a particular data sample, a fit is first performed using the likelihood function

	$B^0 \rightarrow \rho^0 \pi^0$	Comments
	Signal yields and efficiencies	
N_{signal}	24.9	fit to data
$\epsilon_{\text{signal}}^{\text{raw}}$	$20.2 \pm 0.1\%$	smeared signal MC
ϵ_{signal}	$20.0 \pm 0.1\%$	tracking correction
Statistical Error	11.5	parabolic error from fit
	Efficiency and scaling systematics	
Tracking	1.6%	per-track-corrections
PID for tracks	4.0%	PID killing AWG recipe
π^0 -correlated	5.0%	smearing/scaling/killing
π^0 -uncorrelated	0.8%	smearing/scaling/killing
ΔE cut	0.1%	data-vs-MC shift
m_{ES} cut	0.0%	data-vs-MC shift
NNcut	1.0%	data-vs-MC
$\text{Br}(\rho \rightarrow \pi^+ \pi^-)$	1.6%	$\Gamma(\pi^+ \pi^-)/\Gamma(\text{Total})$ err.
$N(B\bar{B})$	1.1%	B-counting
Sub-total:	7.0%	
	Fit systematics	
$\tau_{B^0} \pm 0.016$ ps	0.17	parameter variation
$\tau_{B^+} \pm 0.016$ ps	0.07	parameter variation
Δt Resolution	0.34	parameters from BReco
B Tagging of signal	0.15	parameters from BReco
B -bkg tagging fractions	0.8	Statistic Errors from MC
Fraction of SCF($\pm 5\%$)	0.05	parameter variation
ΔE PDF	0.96	PDF shift and shape
m_{ES} PDF	1.29	PDF shift and shape
NN PDF	2.21	PDF shift and shape
B -background	$+2.00$ -3.26	variation of fractions
Fitting procedure	2.02	bias observed in full MC fits
Sub-total:	4.8	events
Systematics error	19.3%	After unblinding
Branching ratio	$(1.40 \pm 0.64 0.27) \times 10^{-6}$	

Table 6.7: The breakdown of systematics for measurements of $B^0 \rightarrow \rho^0 \pi^0$ Branching Ratio.

to obtain the number of signal events in the sample, μ_s^{fitted} . The *confidence level* (CL) for this measurement, given a signal hypothesis μ_s^{expected} , is:

$$CL(\mu_s^{\text{fitted}}, \mu_s^{\text{expected}}) \equiv \frac{D_{s+b}(\mu'_s \leq \mu_s^{\text{fitted}}; \mu_s^{\text{expected}})}{D_b(\mu'_s \leq \mu_s^{\text{fitted}}, 0)} \quad (6.3)$$

4. The 90% confidence limit corresponding to this fitted signal yield, μ_s^{fitted} , is defined by the requirement:

$$CL(\mu_s^{\text{fitted}}, \mu_s^{90}) = 1 - 0.90 \quad (6.4)$$

A scan is performed over signal hypotheses until the minimum signal hypothesis which satisfies the requirement is determined. This signal hypothesis is μ_s^{90} .

The above procedure yields a relationship between μ_s^{90} and μ_s^{fitted} , which is determined from toy Monte Carlo studies. From this curve one can get the corresponding upper limit at a 90% confidence level. To get the upper limit on the branching fraction, however, one must consider all the systematic uncertainties, including those on the fitted yield, on the event selection efficiency and on scaling factors such as the number of B mesons and the ρ decay width. To be conservative, the upper limit on the yield is shifted up by one standard deviation of the systematic error, and the efficiency and number of B mesons are shifted down by one standard deviation.

The upper limit on the uncorrected signal yield is obtained to be 42.1 with the method described above.

6.8 Summary

All nominal fits and cross-checks on toy Monte Carlo, fully simulated Monte Carlo and data show consistent results. The measurement on the full data set of years (1999-2002) corresponding to 81.9 fb^{-1} gives a signal yield of $24.9 \pm 11.5(\text{stat.}) \pm 4.7(\text{syst.})$. The corresponding branching fraction is $(1.4 \pm 0.6(\text{stat.}) \pm 0.3(\text{syst.})) \times 10^{-6}$. We set a 90% confidence-level upper limit of $\mathcal{B} < 2.8 \times 10^{-6}$ for the color-suppressed mode $B^0 \rightarrow \rho^0 \pi^0$.

Chapter 7

$B^0 \rightarrow \pi^+\pi^-\pi^0$ Dalitz Plot Analysis

The main challenge of the $B^0 \rightarrow \pi^+\pi^-\pi^0$ Dalitz plot analysis is the construction of a realistic signal probability density function, where both the kinematic and dynamical properties as well as their time dependence are modeled to good accuracy. Some basic properties of the Dalitz plot are discussed in appendix C.

7.1 Event Selection

The candidate selection applied here differs in one fundamental aspect from the one used in the previous quasi-two-body analyses: due to the rather involved time-dependent fit, with at minimum 9 physical observables, we attempted to reduce the total number of events entering the likelihood fit. Without compromising the signal efficiency, this goal can only be achieved by sacrificing the m_{ES} and ΔE sidebands. The obvious drawback is that not all empirical shape parameters of the continuum background can be determined by the fit together with the signal parameters. One rather must extrapolate them from sidebands and off-resonance data, which leads to systematic errors. On the other hand, tighter selection requirements lead to improved rejection of poorly constructed self-cross-feed (SCF) events, thus increasing the effi-

ciency of truth-matched (TM) events.

The main part of the $B^0 \rightarrow \pi^+\pi^-\pi^0$ event selection is similar to the one described in the previous quasi-two-body analyses. Details on the ntuple preselection, the vertexing and flavor tagging are given therein.

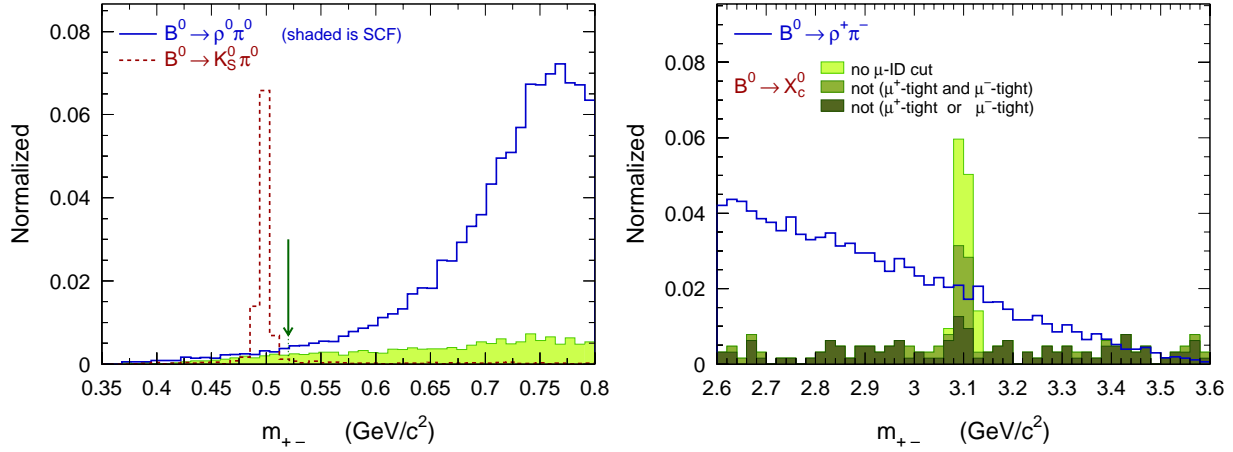


Figure 7.1: *Left: distributions of m_{+-} for $B^0 \rightarrow \rho^0\pi^0$ (solid line for TM and shaded for SCF) and $B^0 \rightarrow K_S^0\pi^0$ events. The arrow indicates the minimum requirement applied. Right: background from $B^0 \rightarrow J/\psi\pi^0 \rightarrow \mu^+\mu^-\pi^0$ events in m_{+-} . The shaded regions indicate different tight-muon PID requirements, of which the second one (medium shaded) is adopted in the analysis. Also shown is the distribution of the $B^0 \rightarrow \rho^\pm\pi^\mp$ signal component.*

- **Dalitz plot (DP):** We remove $B^0 \rightarrow K_S^0\pi^0$ events, of which the Δt distribution is distorted due to the long K_S^0 lifetime. Since they represent a δ (plus resolution) peak in m_{+-} (see left hand plot in Fig. 7.1), we require $m_{+-} > 0.52 \text{ GeV}/c^2$, which is equivalent to $m' < 0.857$. We also remove the center of the Dalitz plot, where no signal is expected, by requiring that either one of the three invariant masses (m_{+0} , m_{-0} , m_{+-}) be lower than $1.5 \text{ GeV}/c^2$.
- **PID:** both tracks must fail the `tight` electron, proton and kaon flags of the

standard Micro selectors. To suppress $B^0 \rightarrow J/\psi \pi^0 \rightarrow \mu^+ \mu^- \pi^0$ events (branching fraction 1.3×10^{-6}), we require that at least one of the charged tracks not to be flagged as a tight muon (see right hand plot in Fig. 7.1). This removes about 45% of the background events without affecting the signal efficiency.

• **Kinematic cuts:**

- m_{ES} : $5.272 < m_{\text{ES}} < 5.288 \text{ GeV}/c^2$. See left hand plot in Fig. 3.1 for the signal and continuum distributions of m_{ES} . Compared to ΔE , only a slight dependence of m_{ES} on the π^0 energy is observed.

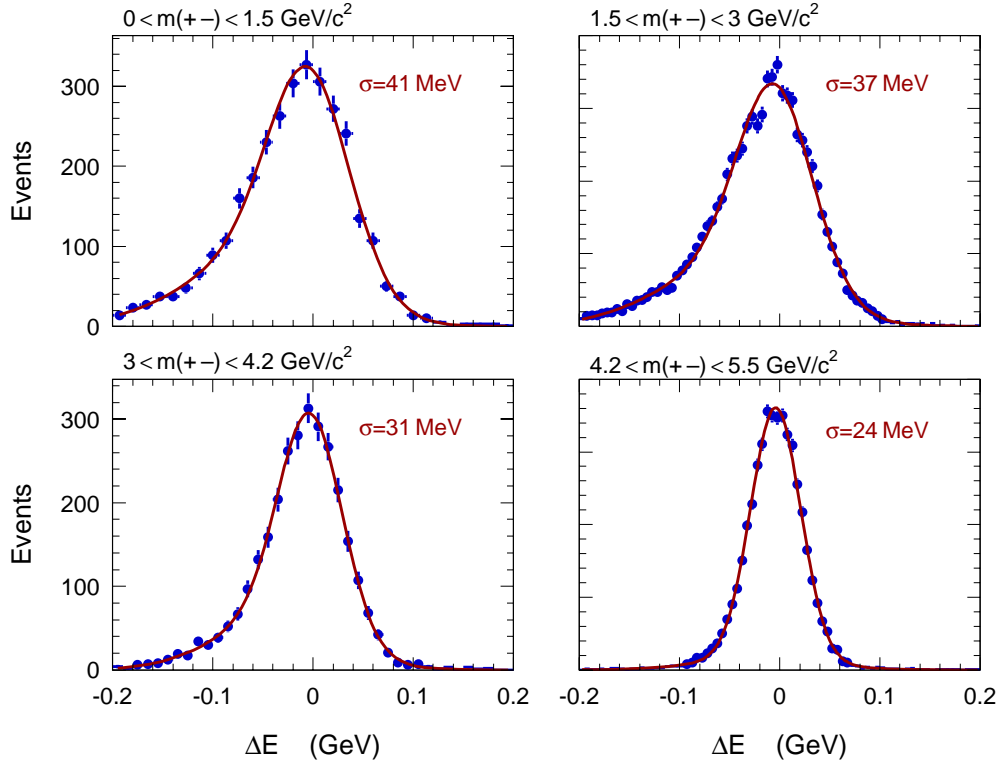


Figure 7.2: Truth-matched ΔE distribution for $\rho^\pm \pi^\mp$ events in different bins of m_{+-} (estimator of the π^0 energy) fit with double Gaussians. The quoted widths are those of the core Gaussians.

- **ΔE** : Dependent on the π^0 energy, the ΔE resolution for TM events varies strongly across the DP. Due to the three-body kinematics, the $\pi^+\pi^-$ invariant mass, m_{+-} , is a good estimator of this dependency. Figure 7.2 shows the ΔE distributions for different bins of m_{+-} . The function corresponds to a fit with a double Gaussian. We account for this effect by applying linearly m_{+-} -dependent cuts on ΔE :

$$\Delta E_{\max}(m_{+-}) = c_{\max} - \frac{c_{\max} - \bar{c}}{m_{+-}^{\max}} \cdot m_{+-} , \quad (7.1)$$

$$\Delta E_{\min}(m_{+-}) = c_{\min} - \frac{c_{\min} + \bar{c}}{m_{+-}^{\max}} \cdot m_{+-} , \quad (7.2)$$

where we use $\bar{c} = 0.045$ GeV, $c_{\min} = -0.140$ GeV, $c_{\max} = 0.080$ GeV and $m_{+-}^{\max} = 25$ GeV/ c^2 . Since variable cuts complicate the treatment of ΔE in the maximum likelihood (ML) fit, we use the redefined quantity

$$\begin{aligned} \Delta E \longrightarrow \Delta E' &= \frac{(\Delta E - \Delta E_{\max}) + (\Delta E - \Delta E_{\min})}{\Delta E_{\max} + \Delta E_{\min}} \\ &= \frac{2 \Delta E m_{+-}^{\max} - (c_{\max} + c_{\min})(m_{+-}^{\max} - m_{+-})}{2 \bar{c} m_{+-} + (c_{\max} - c_{\min})(m_{+-}^{\max} - m_{+-})} , \end{aligned} \quad (7.3)$$

with a validity range after cut of $\Delta E' \in [-1, 1]$.

See right hand plot in Fig. 3.1 for the signal and continuum distributions of $\Delta E'$. Since it is a linear transformation, the quasi-linear behavior of the continuum background is not altered.

- **Δt** : we require $|\Delta t| < 20$ ps and $\sigma_{\Delta t} < 2.5$ ps.

- **MVA:** Since we explicitly exploit the DP information in the ML fit, the ρ mass and helicity cannot be used in the MVA anymore. We find the combination of the four variables, L_0 , L_2 , $\cos\theta_{B,z}$, $\cos\theta_{T_B,z}$, leads to close-to optimal results, while maintaining simplicity. The NN output is required to exceed 0.3 on a scale from -1 to $+1$.

The selection efficiencies relative to the previous cut for signal $B^0 \rightarrow (\rho\pi)^0$ MC of all charges, and for non-resonant $B^0 \rightarrow \pi^+\pi^-\pi^0$ are given in Table 7.1.

Cuts	Relative efficiencies for all signal			
	$\epsilon_{\rho^+\pi^-}^{\text{MC}}$	$\epsilon_{\rho^-\pi^+}^{\text{MC}}$	$\epsilon_{\rho^0\pi^0}^{\text{MC}}$	$\epsilon_{\pi^+\pi^-\pi^0}^{\text{MC}}$
Preselection	0.6723	0.6677	0.5904	0.5731
Track Quality	0.9997	0.9996	0.9988	0.9993
$-1 < \Delta E' < 1$	0.7482	0.7487	0.7880	0.7771
$5.2 < m_{\text{ES}} < 5.288$	0.9843	0.9843	0.9862	0.9888
$m_{+-} > 0.52$	0.9992	0.9992	0.9747	0.9909
$ \Delta t < 20 \text{ ps}$	0.9921	0.9920	0.9874	0.9928
$\sigma(\Delta t) < 2.5 \text{ ps}$	0.9655	0.9658	0.9555	0.9662
Photon Quality	0.8886	0.8873	0.9675	0.9469
$0.11 < m(\pi^0) < 0.16$	0.9771	0.9766	0.9860	0.9882
Electron, Muon Vetoes	0.9873	0.9876	0.9826	0.9893
Kaon Veto	0.9458	0.9421	0.9557	0.9527
Proton Veto	0.9904	0.9900	0.9942	0.9923
NN > 0.3	0.7566	0.7604	0.7652	0.7657
$m_{\text{ES}} > 5.272$ & DP cut	0.8195	0.8263	0.8209	0.3765
Total Efficiency	0.2359	0.2362	0.2357	0.1055

Table 7.1: *Selection efficiencies relative to the previous cut for signal $B^0 \rightarrow (\rho\pi)^0$ MC of all charges, and non-resonant $B^0 \rightarrow \pi^+\pi^-\pi^0$. Masses are given in units of GeV/c^2 .*

Events with multiple B candidates passing the full selection occur on average in 16% ($\rho^\pm\pi^\mp$), 9% ($\rho^0\pi^0$), 3% (non-resonant $\pi^+\pi^-\pi^0$) and 5% (continuum background)

of the cases (see Fig. 3.7). Most of these multi-candidate events have two B candidates. Due to the specific kinematics of multi-candidate events, they occur mostly in the corners of the Dalitz plot. To prevent biasing the PDFs of the discriminating variables that enter the likelihood fit, we apply the following independent criteria to select a single candidate:

- (A) if the multiple candidates have different π^0 's, we choose the one with a reconstructed $\gamma\gamma$ mass closest to the nominal π^0 mass;
- (B) use random choice for events without multiple π^0 's.

The SCF fractions are tagging category dependent: their value for each category is given in table 7.2.

Mode	Lepton	Kaon	f_{scf} NT1	NT2	NoTag
$\rho^+\pi^-$	13.15 ± 0.42	22.48 ± 0.30	17.49 ± 0.59	23.74 ± 0.47	24.83 ± 0.32
$\rho^-\pi^+$	14.90 ± 0.44	23.31 ± 0.30	19.76 ± 0.62	23.26 ± 0.46	25.72 ± 0.32
$\rho^0\pi^0$	7.48 ± 0.32	13.00 ± 0.25	9.89 ± 0.47	13.82 ± 0.40	14.42 ± 0.27

Table 7.2: *Misreconstructed event fractions in each tagging category.*

7.2 Backgrounds from B Decay

We follow a similar strategy as in the previous analyses, where we study the cross-feed from other B -decays using Monte Carlo simulation. A corrective PDF is introduced in the likelihood for classes of major contaminating modes. An extensive list of exclusive charmless $B\bar{B}$ modes has been studied to evaluate the systematics on the event yields and the CP parameters due to cross-feed from these modes. B -backgrounds are categorized into two-, three- and four-body final states. Individual

modes with expected contaminations of two or more events after selection are classified within six classes for charged B decays and eleven classes for neutral B decays. The classes group modes with similar PDFs, and each class represents a corrective term in the likelihood. Their branching fractions, selection efficiencies and expected number of events, computed for an integrated on-resonance luminosity of 209 fb^{-1} , are given in table 7.3.

Charmed neutral B mesons can decay into the $\pi^+\pi^-\pi^0$ final state via the Q2B states $D^-\pi^+$ and $\bar{D}^0\pi^0$ for which the branching fractions (including their decays into $\pi\pi$) have been measured. Due to misidentified kaons or muons, background also includes the Cabibbo-enhanced $B^0 \rightarrow \bar{D}^0(\rightarrow K^+\pi^-)\pi^0$ decays, and $B^0 \rightarrow J/\psi(\rightarrow \mu^+\mu^-)\pi^0$. Whereas all charmed B^+ decays, and the other charmed B^0 decays, not reaching the $\pi^+\pi^-\pi^0$ final state, are treated in two dedicated classes in the B background model, we attribute individual classes to each of the three modes mentioned above.

Parameters for B -background Δt Models

Two processes can modify the nominal Δt distribution function in B -background decays:

- tracks are exchanged between the CP and tag side, and the Δt distribution function becomes narrower than for signal;
- In the presence of long-lived particles (like the K_s^0 or D 's), the Δt distribution becomes broader.

We use dedicated Δt lifetime and resolution parameters for B background to account for these effects.

Class	Id	Mode	BR [10^{-6}]	Efficiency (%)	N_{exp}
0	5013	$B^+ \rightarrow \rho^+ \rho_{[\text{long}]}^0$	15.0 ± 10.0	0.88 ± 0.02	29.4 ± 19.6
0	6000	$B^+ \rightarrow a_1^+(\rightarrow (\rho\pi)^+)\pi^0$	20.0 ± 15.0	0.37 ± 0.03	16.4 ± 12.2
0	6001	$B^+ \rightarrow a_1^0(\rightarrow \rho^+\pi^-\pi^+)\pi^+$	20.0 ± 15.0	0.34 ± 0.02	15.1 ± 11.3
0	42	$B^+ \rightarrow \eta'(\rightarrow \rho^0\gamma)K^+$	22.9 ± 1.4	0.04 ± 0.01	2.1 ± 0.1
1	5058	$B^+ \rightarrow \pi^+\rho^0$	9.2 ± 1.2	2.53 ± 0.04	52.0 ± 6.8
1	53	$B^+ \rightarrow \rho^0 K^+$	4.1 ± 0.9	0.38 ± 0.02	3.4 ± 0.8
1	57	$B^+ \rightarrow f_0(980)(\rightarrow \pi^+\pi^-)K^+$	9.9 ± 1.9	0.15 ± 0.01	3.4 ± 1.8
2	55	$B^+ \rightarrow \pi^+ K_S^0(\rightarrow \pi^+\pi^-)$	7.5 ± 0.5	0.43 ± 0.02	7.2 ± 0.5
3	5051	$B^+ \rightarrow \pi^0 \rho^+$	12.0 ± 1.9	1.77 ± 0.02	47.6 ± 7.5
3	5110	$B^+ \rightarrow \pi^+ K_S^0(\rightarrow \pi^0\pi^0)$	3.4 ± 0.2	1.16 ± 0.01	8.8 ± 0.5
4	1072	$B^+ \rightarrow \pi^+\pi^0$	5.2 ± 0.8	0.77 ± 0.03	9.0 ± 1.4
4	1071	$B^+ \rightarrow K^+\pi^0$	12.5 ± 1.1	0.21 ± 0.00	5.8 ± 0.5
5	1286	$B^+ \rightarrow (K^{(*)}(1430)\pi)^+ \rightarrow (K^+\pi\pi)^+$	29.0 ± 5.4	0.12 ± 0.02	7.8 ± 1.5
5	1299	$B^+ \rightarrow K^+\pi^-\pi_{[\text{nonres}]}^+$	13.5 ± 6.7	0.05 ± 0.01	1.5 ± 0.8
6	44	$B^0 \rightarrow \pi^- K^{*+}(\rightarrow K_S^0\pi^+)$	5.1 ± 1.4	0.17 ± 0.01	1.9 ± 0.5
7	1015	$B^0 \rightarrow \rho^+\rho_{[\text{long}]}^-$	30.0 ± 6.0	0.81 ± 0.01	54.3 ± 10.9
7	1056	$B^0 \rightarrow (a_1\pi)^0$	40.0 ± 15.0	0.36 ± 0.01	32.4 ± 12.1
8	69	$B^0 \rightarrow K^+\pi^-$	18.2 ± 0.8	0.15 ± 0.00	6.0 ± 0.3
9	1045	$B^0 \rightarrow \pi^- K^{*+}(\rightarrow K^+\pi^0)$	5.1 ± 1.4	2.17 ± 0.03	24.8 ± 6.8
9	1289	$B^0 \rightarrow K^{(*)}(1430)\pi \rightarrow K\pi\pi^0$	11.2 ± 2.2	2.18 ± 0.03	54.5 ± 10.7
10	5111	$B^0 \rightarrow \gamma K^{*0}(892, 1430)(\rightarrow K^+\pi^-)$	27.4 ± 1.5	0.18 ± 0.02	10.6 ± 0.6
10	5048	$B^0 \rightarrow \pi^0 K^{*0}(\rightarrow K^+\pi^-)$	0.5 ± 2.0	2.09 ± 0.03	2.3 ± 9.5
10	5041	$B^0 \rightarrow \eta'(\rightarrow \rho^0\gamma)\pi^0$	0.3 ± 0.5	3.76 ± 0.06	2.5 ± 4.2
11	1075	$B^0 \rightarrow \rho^- K^+$	9.0 ± 1.6	3.29 ± 0.02	66.2 ± 11.8
12	64	$B^0 \rightarrow K^+\pi^-\pi_{[\text{nonres}]}^0$	5.7 ± 2.7	1.13 ± 0.01	14.5 ± 6.9
13	5107	$B^0 \rightarrow \pi^0 K_S^0(\rightarrow \pi^+\pi^-)$	4.0 ± 0.5	0.66 ± 0.02	6.0 ± 0.7
14	5109	$B^0 \rightarrow D^-(\rightarrow \pi^-\pi^0)\pi^+$	7.5 ± 2.3	3.98 ± 0.06	32.1 ± 14.7
15	5113	$B^0 \rightarrow \bar{D}^0(\rightarrow K^+\pi^-)\pi^0$	11.0 ± 3.2	0.48 ± 0.02	11.7 ± 3.4
16	5213	$B^0 \rightarrow \bar{D}^0(\rightarrow \pi^+\pi^-)\pi^0$	0.4 ± 0.1	3.98 ± 0.06	3.6 ± 1.9
17	5112	$B^0 \rightarrow J/\psi(\rightarrow e^+e^-, \mu^+\mu^-)\pi^0$	2.6 ± 0.5	0.92 ± 0.03	5.3 ± 2.3
18	—	$B^0 \rightarrow X_c^0$	$-(0.80 \pm 0.06) \times 10^{-4}$		89.0 ± 6.7
19	—	$B^+ \rightarrow X_c^+$	$-(1.76 \pm 0.09) \times 10^{-4}$		196.9 ± 9.9

Table 7.3: *Classification of backgrounds from B decay.*

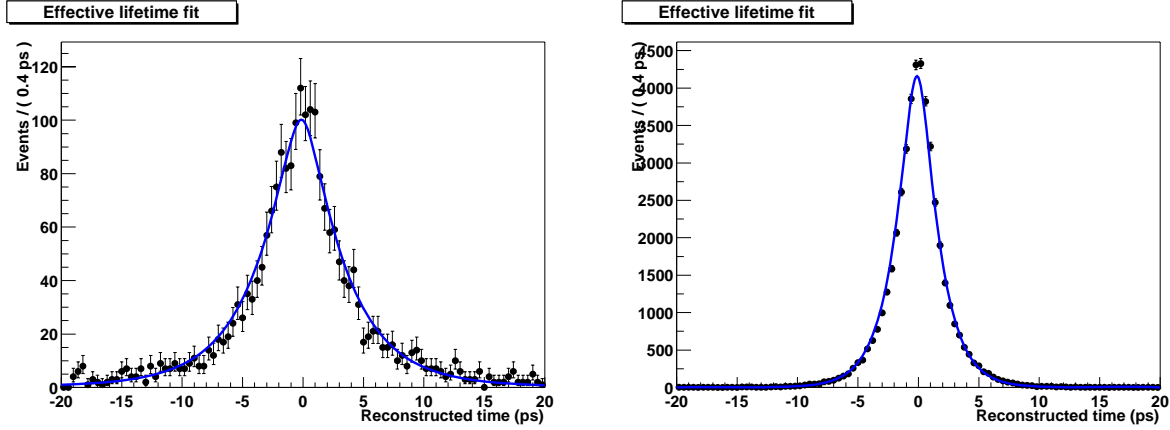


Figure 7.3: *Left: simulated $B^+ \rightarrow \pi^+ K_S^0 (\rightarrow \pi^+ \pi^-)$ events and the fit Δt model (see Eq. 7.24) in which the effective lifetime and the tail Gaussian width were let free to vary. Right: simulated $B^+ \rightarrow \pi^+ \rho^0$ events and the fit Δt model in which only the effective lifetime was let free to vary.*

Effective lifetimes for charged B decays

Figure 7.3 illustrates one of the two effects listed above that can modify the Δt distribution: the presence of a long-lived particle (here a K_S^0) in the decay. The Δt distribution becomes broader than the signal Δt distribution. To account for these effects, we introduce an effective lifetime, different from the nominal charged B lifetime, for the Δt distribution given in Eq. (7.24). In some cases the fit remains unsatisfactory and in that case the width of the tail Gaussian in the resolution function is individually adjusted. The other parameters in the resolution function are obtained from fits to **Breco** MC events [15]. The effective lifetimes and widths of the tail Gaussian are determined by a fit to B background MC events with relaxed ΔE and m_{ES} requirements to increase the available statistics. The results of two such fits are shown in Fig. 7.3. The per-class parameters used in the likelihood model are obtained from weighted averages of the contributing modes.

For charmed charged B background, we use the default **Breco** parameters.

Effective resolution functions for neutral B decays

Due to $B^0\bar{B}^0$ mixing, the B lifetime cannot be used anymore as effective resolution parameters for neutral B background. Instead, we determine individual Δt resolution parameters for each mode. We find that most neutral B background modes are correctly described by the default **Breco** parameters, except for the following modes:

- $B^0 \rightarrow \pi^0 K_S^0 (\rightarrow \pi^+ \pi^-)$, due to the presence of the K_S^0 . The Δt distribution is showed on the left part of Figure 7.4.
- decays containing a D meson: $B^0 \rightarrow D^-(\rightarrow \pi^-\pi^0)\pi^+$, and $B^0 \rightarrow \bar{D}^0(\rightarrow K^+\pi^-)\pi^0$. In particular, the first mode is important for validation purposes because of its large statistics (see Table 7.3). The Δt distribution of this mode is shown on the right part of Figure 7.4. The resolution function parameters for the two decays are extracted from Monte Carlo simulation.

For charm neutral B background, we use the default **Breco** parameters.

7.3 Building the Likelihood

The signal likelihood consists of the sum of a correctly reconstructed (TM) component and a mis-reconstructed (SCF) component. Tests with toy Monte Carlo show that with respect to the statistical sensitivity on α , 1 TM event has approximately the same weight as 2.5 SCF events. For an average SCF fraction of about 20%, the expected error on α is improved by approximately 4% when including the SCF events in the fit.

The probability density \mathcal{P}_i^c for a single event i in tagging category c is the sum

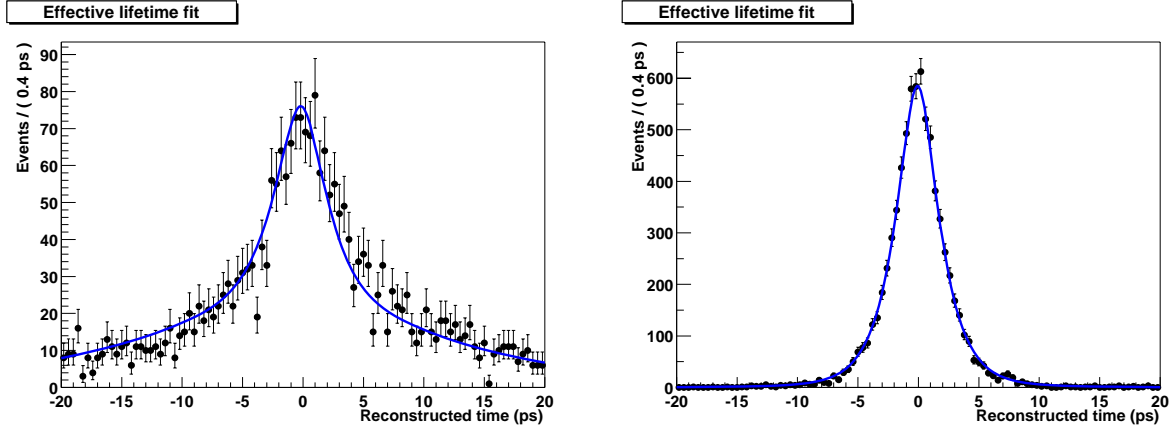


Figure 7.4: *Left:* overlay of the modified Δt model (using $S_{\text{tail}} = 12.871 \pm 0.42$ and $f_{\text{tail}} = 0.25 \pm 0.01$ to parameterize the resolution function) and the $B^0 \rightarrow \pi^0 K_s^0 (\rightarrow \pi^+ \pi^-)$ MC simulation data. *Right:* overlay of the modified dt model (using and the $B^0 \rightarrow D^- (\rightarrow \pi^- \pi^0) \pi^+$ MC simulation data.

of the probability densities of all components, namely,

$$\begin{aligned}
 \mathcal{P}_i^c \equiv & N_{3\pi} f_{3\pi}^c \left[(1 - \bar{f}_{\text{SCF}}^c) \mathcal{P}_{3\pi-\text{TM},i}^c + \bar{f}_{\text{SCF}}^c \mathcal{P}_{3\pi-\text{SCF},i}^c \right] \\
 & + N_{q\bar{q}}^c \frac{1}{2} (1 + q_{\text{tag},i} A_{q\bar{q},\text{tag}}) \mathcal{P}_{q\bar{q},i}^c \\
 & + \sum_{j=1}^{N_{\text{class}}^{B^+}} N_{B^+j} f_{B^+j}^c \frac{1}{2} (1 + q_{\text{tag},i} A_{B^+,\text{tag},j}) \mathcal{P}_{B^+,ij}^c \\
 & + \sum_{j=1}^{N_{\text{class}}^{B^0}} N_{B^0j} f_{B^0j}^c \mathcal{P}_{B^0,ij}^c,
 \end{aligned} \tag{7.4}$$

where,

- $N_{3\pi}$ is the total number of $\pi^+ \pi^- \pi^0$ signal events the data sample;
- $f_{3\pi}^c$ is the fraction of signal events that are tagged in category c ;
- \bar{f}_{SCF}^c is the fraction of misreconstructed signal events (SCF) in tagging category

c , averaged over the Dalitz plot (DP);

- $\mathcal{P}_{3\pi-\text{TM},i}^c$ and $\mathcal{P}_{3\pi-\text{SCF},i}^c$ are the products of PDFs of the discriminating variables used in tagging category c , for truth-matched (TM) and SCF events respectively;
- $N_{q\bar{q}}^c$ is the number of continuum events that are tagged in category c ;
- $q_{\text{tag},i}$ is the tag flavor of the event; we use $q_{\text{tag},i} = 1$ for B^0 -tag and $q_{\text{tag},i} = -1$ for \bar{B}^0 -tag;
- $A_{q\bar{q},\text{tag}}$ is the tag asymmetry, parameterizing a possible charge asymmetry in continuum events;
- $\mathcal{P}_{q\bar{q},i}^c$ is the continuum PDF for tagging category c ;
- $N_{\text{class}}^{B^+}$ ($N_{\text{class}}^{B^0}$) is the number of charged (neutral) B -related background classes considered (*cf.* Section 7.2);
- N_{B^+j} (N_{B^0j}) is the number of expected events in the charged (neutral) B -related background class j ;
- $f_{B^+j}^c$ ($f_{B^0j}^c$) is the fraction of charged (neutral) B -related background events of class j that are tagged in category c ;
- $A_{B^+, \text{tag}, j}$ describes the tag asymmetry in charged B -background of class j ; this parameterizes eventual charge asymmetry; note that the tag-charge correlation is absorbed in the tag flavor-dependent DP PDFs;
- $\mathcal{P}_{B^+, ij}^c$ is the B^+ -background PDF for tagging category c and class j ;

- $\mathcal{P}_{B^0,ij}^c$ is the B^0 -background PDF for tagging category c and class j ; the time-dependent PDF is non-trivial as neutral B background can exhibit direct and mixing-induced CPV;

The PDFs \mathcal{P}_X^c are the product of the PDFs of the five discriminating variables x_k , $k = 1, \dots, 5$:

$$\mathcal{P}_{X,i(j)}^c \equiv \prod_k P_{X,i(j)}^c(x_k) . \quad (7.5)$$

Finally, the extended likelihood over all tagging categories is again given by

$$\mathcal{L} \equiv \prod_{c=1}^5 e^{-\overline{N}^c} \prod_i^{N^c} \mathcal{P}_i^c , \quad (7.6)$$

where \overline{N}^c is the number of events expected in category c .

Here we give the details of how to construct the combined time and Dalitz plot PDFs. The connection of time and DP dependence leads to rather involved PDFs both conceptually and technically. They are discussed below for the signal and background components of the likelihood (7.4). The signal resonance model assumed in the DP and entering the time- and DP-dependent PDF (1.38) is discussed in Section 1.4.2.

- **Amplitude dependent normalization.**

When using Eq. (1.38) as a PDF in the likelihood fit, one has to normalize it, *i.e.*, one must replace [20],

$$|\mathcal{A}_{3\pi}^\pm(\Delta t)|^2 \longrightarrow \frac{1}{\langle |N|^2 \rangle} |\mathcal{A}_{3\pi}^\pm(\Delta t)|^2 \quad (7.7)$$

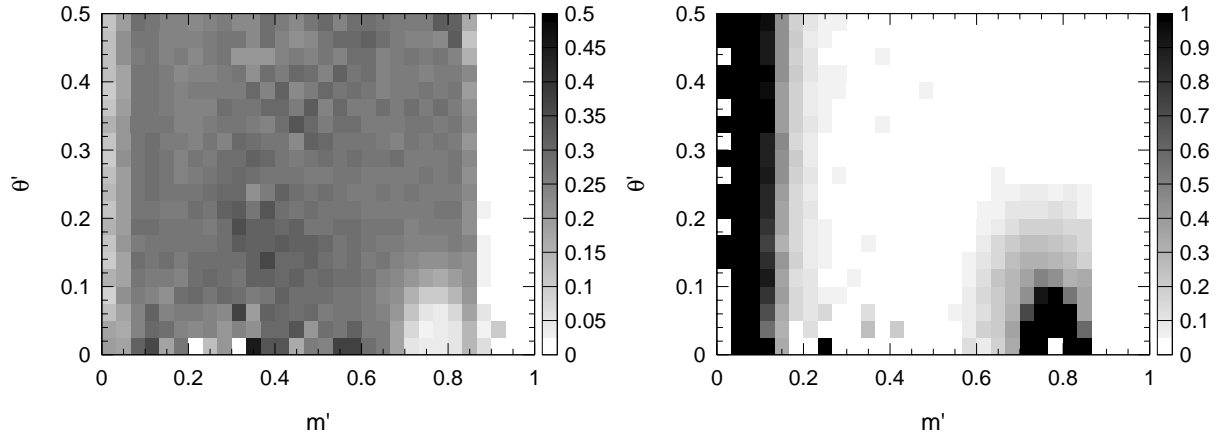


Figure 7.5: *Selection efficiency of $B^0 \rightarrow \pi^+\pi^-\pi^0$ events (left plot) and fraction of misreconstructed events (right plot), in square Dalitz plot. The symmetric property of the DP has been used for the square DPs to double the available statistics. The plots are made with a sample of 1.40 million signal MC events.*

where

$$\langle |N|^2 \rangle = |N|^2 + |\overline{N}|^2, \quad (7.8)$$

and

$$|N|^2 \equiv \langle |\mathcal{A}_{3\pi}|^2 \rangle = \int \int \int |\mathcal{A}_{3\pi}|^2 dm_{+0}^2 dm_{-0}^2 d\Delta t \quad (7.9)$$

and similarly for $|\overline{N}|^2 \equiv \langle |\overline{\mathcal{A}}_{3\pi}|^2 \rangle$.

- **DP-dependent selection efficiency and SCF fraction.**

Dalitz plot PDFs and DP-averaged quantities, like normalization or SCF fractions, require the knowledge of the DP-dependent relative selection efficiency $\epsilon = \epsilon(m', \theta')$. It is a decay-dynamics invariant quantity and is obtained from high statistics MC simulation. It is shown in the left plot of Fig. 7.5 for the square DP. One observes a rather flat efficiency over most regions of the Dalitz

plot, with an increase along rising m' (m_{+-}) values, due to the larger π^0 energies. Close to the extreme corners of the DP the efficiency drops, which is where two particles are back-to-back, while the third is (almost) at rest, and acceptance is necessarily low due to the minimum p_T (tracks) or E_γ (neutrals) requirements.

Moreover, the DP part in the likelihood component for TM and SCF signal (*cf.* Eq. (7.4)) must be expanded to account for a DP-dependent SCF fraction $f_{\text{SCF}} = f_{\text{SCF}}(m', \theta')$. For an event i , we have the PDF (*cf.* Eq. (7.5)).

$$P_{3\pi\text{-TM},i} = \epsilon_i (1 - f_{\text{SCF},i}) |\det J_i| \frac{|\mathcal{A}_{3\pi}^\pm(\Delta t)|^2}{\langle |N_{\text{TM}}|^2 \rangle}, \quad (7.10)$$

$$P_{3\pi\text{-SCF},i} = \epsilon_i f_{\text{SCF},i} |\det J_i| \frac{|\mathcal{A}_{3\pi}^\pm(\Delta t)|^2}{\langle |N_{\text{SCF}}|^2 \rangle}, \quad (7.11)$$

The normalization constants $\langle |N_{\text{TM}}|^2 \rangle$ and $\langle |N_{\text{SCF}}|^2 \rangle$ are those from Eq. (7.9), with the difference that now the phase space integration has to take into account the DP-dependent efficiencies and SCF fractions

$$|N_{\text{TM}}|^2 = \text{Re} \sum_{\kappa, \sigma} A^\kappa A^{\sigma*} \langle \epsilon (1 - f_{\text{SCF}}) |\det J| f^\kappa f^{\sigma*} \rangle, \quad (7.12)$$

$$|N_{\text{SCF}}|^2 = \text{Re} \sum_{\kappa, \sigma} A^\kappa A^{\sigma*} \langle \epsilon f_{\text{SCF}} |\det J| f^\kappa f^{\sigma*} \rangle, \quad (7.13)$$

and similarly for $|\overline{N}_{\text{TM}}|^2$ and $|\overline{N}_{\text{SCF}}|^2$. The indices κ, σ run over all resonances of the signal model. The expectation values occurring in Eqs. (7.12, 7.13) are model-dependent and are computed with high statistics MC integration over the

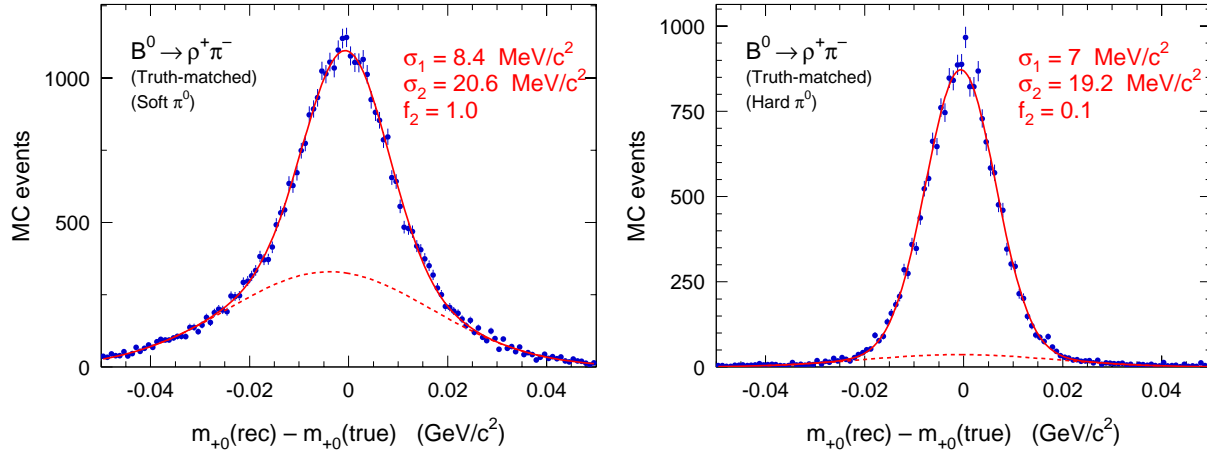


Figure 7.6: Resolution of the reconstructed p^+ mass in the MC for soft π^0 (left plot) and hard π^0 (right plot) in TM events. The parameters correspond to a double Gaussian fit, where “1” is the core Gaussian and “2” the tail Gaussian.

square DP:

$$\langle \epsilon (1 - f_{\text{SCF}}) | \det J | f^\kappa f^{\sigma*} \rangle = \frac{\int_0^1 \int_0^1 \epsilon (1 - f_{\text{SCF}}) | \det J | f^\kappa f^{\sigma*} dm' d\theta'}{\int_0^1 \int_0^1 \epsilon | \det J | f^\kappa f^{\sigma*} dm' d\theta'} , \quad (7.14)$$

and similarly for $\langle \epsilon | \det J | f^\kappa f^{\sigma*} \rangle$, where all quantities in the integrands are DP-dependent. Note that the integral (7.14) depends on the dynamics (form factors) assumed for the signal model. If parameters of this model are determined from a fit to data, the determination of Eq. (7.14) has to be iterative.

The DP-dependent SCF fractions obtained from MC simulation are plotted in Fig. 7.5 (right), for the square DP. The distribution pattern of the SCF fractions over the DP is a consequence of the same kinematic property that is responsible for the efficiency drop in the Dalitz corners. Combinatorial background is high (close to one) in the presence of soft neutrals or tracks. Misreconstructed signal events are almost absent in the center of the DP.

- **DP-averaged SCF fraction.**

Equation (7.4) invokes the Q2B-like phase space-averaged SCF fraction \bar{f}_{SCF} . As for the PDF normalization, it is decay dynamics-dependent, since it is obtained from an integral of the decay amplitude-squared over the Dalitz plot

$$\bar{f}_{\text{SCF}} = \frac{\sum_{\text{tag}} \int \int \int \epsilon f_{\text{SCF}} |\det J_i| |\mathcal{A}_{3\pi}^{\pm}(\Delta t)|^2 dm' d\theta' d\Delta t}{\sum_{\text{tag}} \int \int \int \epsilon |\det J_i| |\mathcal{A}_{3\pi}^{\pm}(\Delta t)|^2 dm' d\theta' d\Delta t} . \quad (7.15)$$

It has to be computed iteratively, and the associated systematic uncertainty is expected to be small.

- **TM resolution.**

The intrinsic width of the dominant $\rho(770)$ resonance expressed in terms of standard deviations of a double Gaussian fit function, gives approximately (the form factor $F_{\rho(770)}$ is expressed as a function of the linear mass here)

$$\sigma_{\text{core}}(F_{\rho(770)}) \approx 0.5 \Gamma_{\rho(770)} \approx 75 \text{ MeV}/c^2 , \quad (7.16)$$

$$\sigma_{\text{tail}}(F_{\rho(770)}) \approx 2.0 \Gamma_{\rho(770)} \approx 300 \text{ MeV}/c^2 . \quad (7.17)$$

It can be compared with the mass resolution for TM events plotted in Fig. 7.6 for soft π^0 's (left plot) and hard π^0 's (right plot). Recall that the soft π^0 region is where the TM efficiency is low and the SCF fraction is high. Even the worst tail-Gaussian resolution of $20.6 \text{ MeV}/c^2$ is more than a factor of three narrower than the core width of the double Gaussian fit to the $\rho(770)$ form factor. Toy MC fits have shown that the systematic bias from neglecting the resolution effects

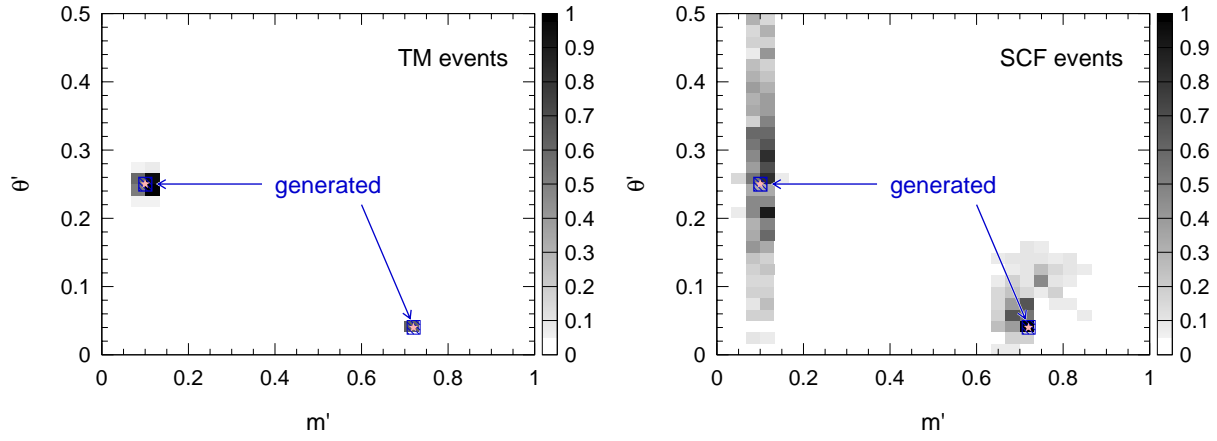


Figure 7.7: *Resolution for TM (left) and SCF events (right hand plot) for two chosen generated values in the square DP, indicated by the open stars (see text for the numerical values).*

in the fit model is below 0.1° for α . We therefore do not account for resolution effects in the TM model.

- **SCF resolution.**

Misreconstructed events are concentrated in the corners of the Dalitz plot and have a mass resolution that dramatically varies across the DP. Figure 7.7 shows the resolution function of TM (left) and SCF events (right) for two arbitrarily generated values. In contrast to TM events, the resolution effects cannot be ignored for SCF events. We therefore introduce a 2×2 -dimensional convolution function

$$R_{\text{SCF}}(m'_r, \theta'_r, m'_t, \theta'_t) , \quad (7.18)$$

which represents the probability to reconstruct at the coordinate (m'_r, θ'_r) an

event that has the true coordinate (m'_t, θ'_t) . It obeys the unitarity condition

$$\int_0^1 \int_0^1 R_{\text{SCF}}(m'_r, \theta'_r, m'_t, \theta'_t) dm'_r d\theta'_r = 1, \quad \forall (m'_t, \theta'_t) \in \text{SDP}. \quad (7.19)$$

The R_{SCF} function is obtained from MC simulation and implemented as four-dimensional smoothed histogram.

- **Signal parameterization of Δt and Dalitz plot:**

The reference distribution for the physical Dalitz plot (efficiency and resolution corrections have been discussed in the previous section) depends on the underlying resonance structure and is connected to Δt via the matrix element (1.38), which serves as the PDF.

Since the PDF deals with measured quantities, the physical time-dependent matrix element is extended to include mistag probabilities and convolved with the Δt resolution \mathcal{R}_{sig} . For an event with a tag-flavor q_{tag} , this leads to:

$$\begin{aligned} |\mathcal{A}_{3\pi}^\pm(\Delta t, \sigma_{\Delta t})|^2 &= \left[1 + q_{\text{tag}} \frac{\Delta D^c}{2} - q_{\text{tag}} \langle D \rangle^c \frac{|\mathcal{A}_{3\pi}|^2 - |\bar{\mathcal{A}}_{3\pi}|^2}{|\mathcal{A}_{3\pi}|^2 + |\bar{\mathcal{A}}_{3\pi}|^2} \cos(\Delta m_d \Delta t') \right. \\ &\quad \left. + q_{\text{tag}} \langle D \rangle^c \frac{2\text{Im} [\bar{\mathcal{A}}_{3\pi} \mathcal{A}_{3\pi}^*]}{|\mathcal{A}_{3\pi}|^2 + |\bar{\mathcal{A}}_{3\pi}|^2} \sin(\Delta m_d \Delta t') \right] \\ &\quad \left[\frac{e^{-|\Delta t'|/\tau_{B^0}}}{4\tau_{B^0}} \otimes \mathcal{R}_{\text{sig}}(\Delta t' - \Delta t, \sigma_{\Delta t}) \right], \end{aligned} \quad (7.20)$$

where $\langle D \rangle^c$ and ΔD^c are the tagging-category-specific average and difference of

the tagging dilutions given by

$$\begin{aligned}\langle D \rangle^c &= 1 - (\omega^c + \bar{\omega}^c) , \\ \Delta D^c &= -2(\omega^c - \bar{\omega}^c) ,\end{aligned}\tag{7.21}$$

with the (tagging category-dependent) mistag rates ω^c and $\bar{\omega}^c$ for B^0 and \bar{B}^0 tags, respectively.

The resolution model that incorporates the finite vertex resolution follows the standard recipe used in similar time-dependent analyses (*cf.* Ref. [15]). The resolution function is modeled using a triple Gaussian, which consists of a core and a tail Gaussian which have biases and widths scaled the event-by-event error $\sigma_{\Delta t}$, and a non-scaled, broad Gaussian to neutralize outlier events:

$$\begin{aligned}\mathcal{R}_{\text{sig}}(\Delta t, \sigma_{\Delta t}) &= (1 - f_{\text{tail}} - f_{\text{out}}) G(\Delta t, s_{\text{core}}^b \sigma_{\Delta t}, s_{\text{core}}^\sigma \sigma_{\Delta t}) \\ &\quad + f_{\text{tail}} G(\Delta t, s_{\text{tail}}^b \sigma_{\Delta t}, s_{\text{tail}}^\sigma \sigma_{\Delta t}) + f_{\text{out}} G(\Delta t, s_{\text{out}}^b, \sigma_{\text{tail}})\end{aligned}\tag{7.22}$$

where $G(x, x_0, \sigma)$ is a Gaussian with bias x_0 and standard deviation σ . We use the biases and relevant scale factors measured in **BReco** events [15].

- **B -background parameterization.**

The DP- and Δt -dependent PDFs factorize for the charged B -background modes, but not for the neutral B background due to $B^0\bar{B}^0$ mixing.

The **charged B -background** contribution to the likelihood (7.4) invokes the parameter $A_{B^+, \text{tag}}$, multiplied by the tag flavor q_{tag} of the event. In the presence

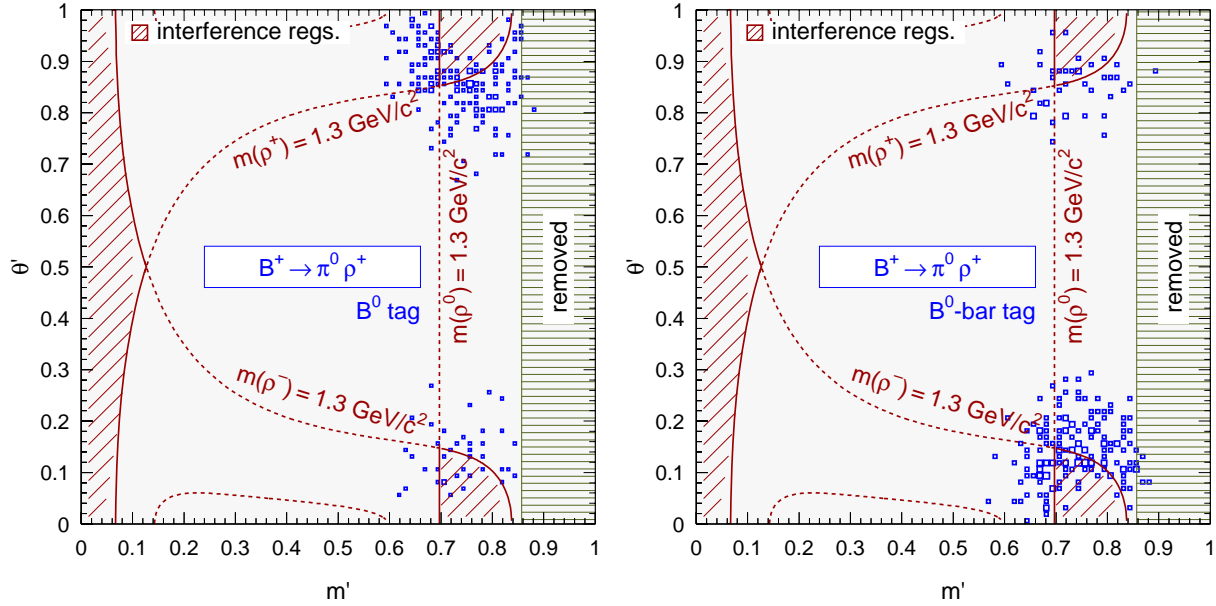


Figure 7.8: Square DPs for the decay $B^\pm \rightarrow \rho^\pm \pi^0$ where the other B is tagged as B^0 (left) and as \bar{B}^0 (right).

of significant tag-“charge” correlation (denoting an effective tag-versus-Dalitz coordinate correlation), $A_{B^+, \text{tag}}$ parameterizes possible direct CPV in these events. It is primarily introduced for systematic studies and is set to zero for the nominal fit. We also use distinct square DP PDFs for each reconstructed B flavor tag, and a tag-averaged PDF for untagged events. This parameterizes the tag-“charge” correlation, denoted A_π in the Q2B analysis. See Fig. 7.8 for the decay $B^+ \rightarrow \pi^0 \rho^+$, which exhibits strong tag-“charge” correlation. The DP-dependent PDF (from which the time dependence factorizes) reads

$$\begin{aligned}
 P_{B^+}^c(\text{DP}) &= (1 + q_{\text{tag},i} A_{B^+, \text{tag},j}) (1 - \omega^c) P_{B^+}^c(\text{DP}, q_{\text{tag}}) \\
 &+ (1 - q_{\text{tag},i} A_{B^+, \text{tag},j}) \omega^c P_{B^+}^c(\text{DP}, -q_{\text{tag}}), \quad (7.23)
 \end{aligned}$$

where ω^c are the tagging-category-specific mistag probabilities defined in Eqs. (7.21).

We use the **BReco** values [15], while the tagging efficiencies are obtained from Monte Carlo simulation. The PDFs $P_{B^+}^c(\text{DP}, \pm q_{\text{tag}})$ are obtained from MC simulation requiring the true B flavor. We parametrize with smoothed histograms. Since the tag-“charge” correlation is implemented in the DP PDF, the Δt PDF for B^+ background class j is simply given by the exponential decay rate

$$P_{B^+}(\Delta t) = e^{|\Delta t|/\tau_j} \otimes \mathcal{R}_{\text{sig}}(\Delta t' - \Delta t, \sigma_{\Delta t}) , \quad (7.24)$$

where τ_j is an effective lifetime, which is mostly equal to τ_{B^+} . The resolution function \mathcal{R} is similar to the one used for the signal (see (Eq. 7.22)). In cases where secondary vertices occur, *e.g.*, in D or K_S^0 decays, the effective lifetime and/or resolution can be significantly altered. We determine these parameters individually for each B -background class j from Monte Carlo simulation.

Neutral B -background contributions in Eq. (7.4) are parameterized using tag-dependent PDFs as done for the charged B -background modes. In the case of CP eigenstates, correlation between the tag and the Dalitz coordinate are of detector/reconstruction origin and expected to be small. Non- CP eigenstates, such as $a_1^\pm \pi^\mp$, may exhibit tag-“charge” correlation. Moreover, both types of decays can have direct and mixing-induced CP violation. A third class of decays involves charged kaons and does not exhibit mixing-induced CP violation, but usually a strong tag-“charge” correlation, because it consists of B -flavor eigenstates.

Since neutral B s oscillate, using effective lifetimes as part of the resolution model,

as done for charged B background, is not permitted. We therefore apply individual resolution parameters. And the following combined Δt and DP PDF for an event with tag q_{tag} is built:

$$\begin{aligned}
P_{B^0,j}^c(\Delta t, \sigma_{\Delta t}, \text{DP}) &= (|A_{B^0,j}|^2 + |\bar{A}_{B^0,j}|^2) \cdot \frac{e^{-|\Delta t|/\tau_j}}{4\tau_j} \\
&\times \left[1 + q_{\text{tag}} \frac{\Delta D_j^c}{2} + q_{\text{tag}} \langle D \rangle_j^c (S_j + \Delta S_j) \sin(\Delta m_d \Delta t') \right. \\
&\quad \left. - q_{\text{tag}} \langle D \rangle_j^c \left(C_j + \frac{|A_{B^0,j}|^2 - |\bar{A}_{B^0,j}|^2}{|A_{B^0,j}|^2 + |\bar{A}_{B^0,j}|^2} \Delta C_j \right) \cos(\Delta m_d \Delta t') \right] \\
&\quad \otimes \mathcal{R}_{\text{sig}}(\Delta t' - \Delta t, \sigma_{\Delta t}) , \tag{7.25}
\end{aligned}$$

where the $\langle D \rangle_j^c$ and ΔD_j^c are the tag dilutions in category c and B -background class j (*cf.* Eq. (7.21)), and are obtained from MC simulation.

It is used to introduce possible “charge” asymmetry and “charge”-dependent mixing-induced CPV into the PDF model. The parameters C_j , S_j and ΔS_j in class j are unknown in general and set to zero in the nominal model. They are varied for the purpose of systematic studies. The situation is different for the tag-”charge” correlation parameter ΔC_j . For most of the modes, tag-charge correlation in the Dalitz plot can be relatively reliably taken from the MC simulation, via the coefficient in front of the ΔC_j , where the amplitude moduli-squared are simply the normalized DP distributions in B^0 and \bar{B}^0 decays. The DP PDFs are obtained from smoothed histograms of MC-simulated events.

Note that the physical parameters in the time-dependent PDF are diluted by the (mostly) incomplete reconstruction of the B -background events.

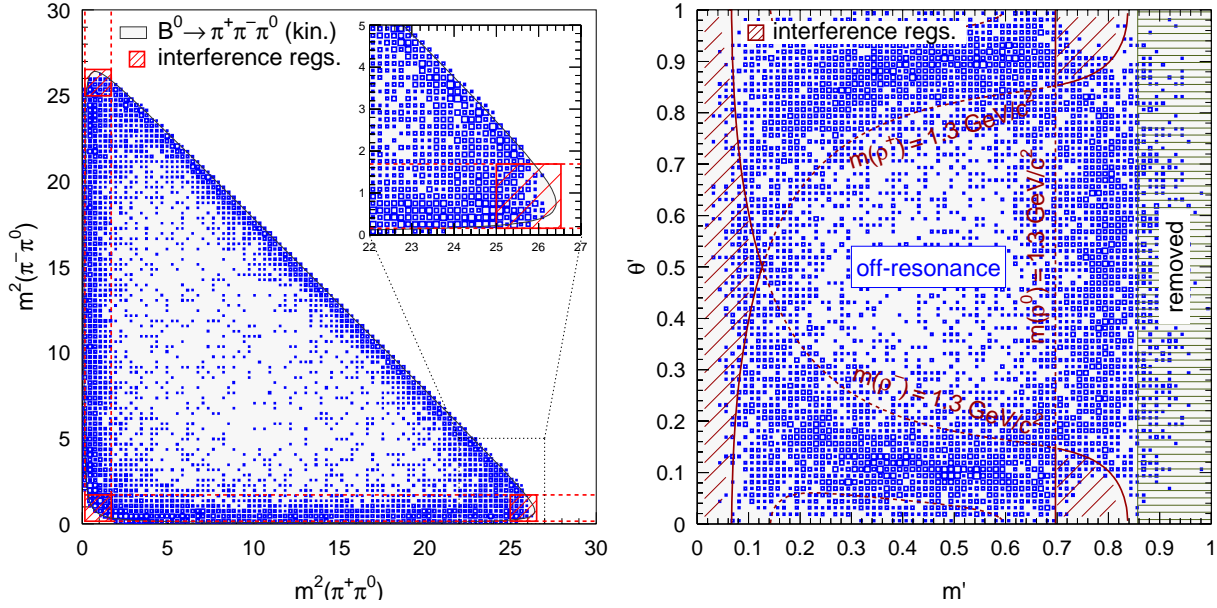


Figure 7.9: *Dalitz plot (left) and square DP (right) distributions for off-resonance events.*

- **Continuum parameterization.**

The **Dalitz plot** treatment of continuum events is similar to the one used for charged B background. In particular, the DP and Δt PDFs factorize. The continuum contribution to the likelihood (7.4) invokes the parameter $A_{q\bar{q}, \text{tag}}$, multiplied by the tag flavor q_{tag} of the event. It parameterizes possible charge asymmetry in these events and is determined by the fit to data. We also use distinct square DP PDFs for each reconstructed B flavor tag, and a tag-averaged PDF for untagged events.

It is the particularity of the approach adopted in this analysis that the square DP PDF for continuum events is obtained from off-resonance data using signal

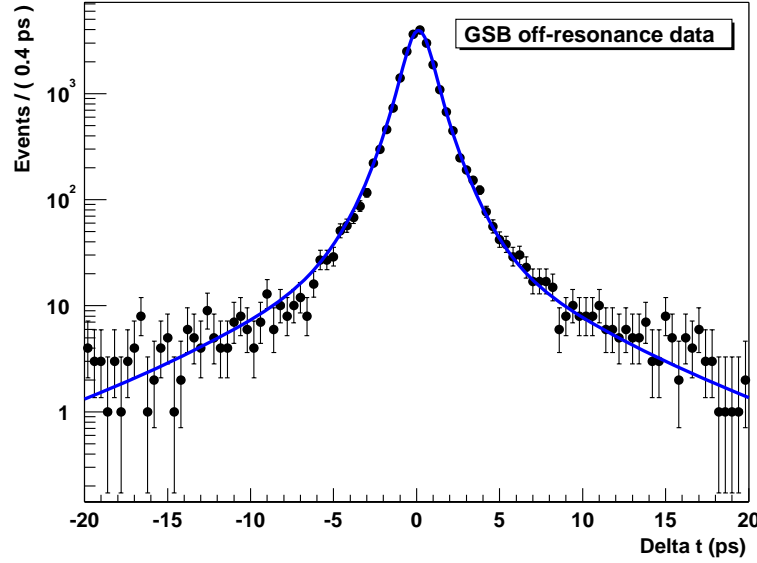


Figure 7.10: *Distribution of Δt for 22,145 GSB off-resonance events. The solid line shows the fit projection of the PDF model (7.27).*

region (SR) *and* grand sidebands (GSB), where the GSB corresponds to

$$m_{\text{ES}} > 5.200 \text{ GeV}/c^2 \quad \text{and} \quad -0.4 < \Delta E < 0.4 \text{ GeV} . \quad (7.26)$$

Since the empirical shape parameters of the PDFs are not determined simultaneously with the signal parameters by the fit, we have to worry about the validity of the GSB-to-SR extrapolation. We will come back to this point in Section 7.5. Since continuum events are the dominant background, we must also ensure a high fidelity of the empirical shape parameterization. This has been the main motivation for the development of the square DP (C.22), since continuum events cluster at low invariant masses (compared to m_B), and thus populate the kinematic borders of the DP (see Fig. 7.9).

The continuum Δt PDF is parameterized as the sum of three Gaussian distribu-

tions with a common mean (which has the unit of a time), two relative fractions, and three distinct widths (without units) that scale the Δt event-by-event error, $\sigma_{\Delta t}$, yielding six free parameters:

$$\begin{aligned}
 P_{q\bar{q},i}(\Delta t, \sigma_{\Delta t}) &= (1 - f_{\text{tail}} - f_{\text{out}}) \cdot G(\Delta t, \mu, s_{\text{core}}\sigma_{\Delta t}) \\
 &+ f_{\text{tail}} \cdot G(\Delta t, \mu, s_{\text{tail}}\sigma_{\Delta t}) \\
 &+ f_{\text{out}} \cdot G(\Delta t, \mu, s_{\text{out}}\sigma_{\Delta t}) \quad .
 \end{aligned} \tag{7.27}$$

The model is motivated by the observation [37] that the mean of Δt is independent of $\sigma_{\Delta t}$, and that the Δt RMS depends linearly on $\sigma_{\Delta t}$. Figure 7.10 shows off-resonance data and the fit result using the model (7.27).

7.4 Fit Results

The result of the fit to the data set as of the summer of 2004 is given in Table 7.4. The Q2B parameters extracted from Us and Is are given in Table 7.5. The projections of each individual variable are shown in Figure 7.11.

Floating the B^0 lifetime floating gives $\tau_B = (1.549 \pm 0.080)$ ps, and floating Δm_d gives $\Delta m_d = (0.57 \pm 0.11)$ ps⁻¹. Both are in good agreement with the PDG values. Leaving the B -background overall scale factor free gives $(0.986 \pm 0.099)\%$ and in good agreement with the expected value of 1.

Scans on α and $\hat{\delta}$

In a second step, the fitted Us and Is can be used to separately constraint the two angles α and $\hat{\delta} \equiv \arg[A^{-+}A^{+-*}]$. In both cases, the procedure is the following: the physical range of the angle ($[0^\circ; 180^\circ]$ for α due to the fit symmetry for α and $\alpha + 180^\circ$;

Parameter	Description	Value
$N_{\rho\pi}$	Number of $B \rightarrow \rho\pi$ events	1184 ± 58
aRes(1450)	Amplitude of $\rho(1450)$	0.87 ± 0.15
aResPh(1450)	Phase of $\rho(1450)(^\circ)$	199 ± 14
$f(\Delta t)_1$	1st Gaussian fraction of continuum Δt distribution	0.115 ± 0.019
$f(\Delta t)_2$	2nd Gaussian fraction of continuum Δt distribution	0.0280 ± 0.0038
$\mu(\Delta t)_1$	Mean of continuum Δt distribution (ps)	0.0264 ± 0.0064
$\sigma(\Delta t)_1$	1st Gaussian sigma of continuum Δt distribution	1.073 ± 0.017
$\sigma(\Delta t)_2$	2nd Gaussian sigma of continuum Δt distribution	2.60 ± 0.25
$\sigma(\Delta t)_3$	3rd Gaussian sigma of continuum Δt distribution	10.39 ± 0.84
$N_{\text{cont}}^{\text{Lepton}}$	Number of continuum events in Lepton category	25.1 ± 7.5
$N_{\text{cont}}^{\text{KPIorK}}$	Number of continuum events in KPIorK category	910 ± 33
$N_{\text{cont}}^{\text{KorPI}}$	Number of continuum events in KorPI category	2481 ± 53
$N_{\text{cont}}^{\text{Inclusive}}$	Number of continuum events in Inclusive category	2450 ± 52
$N_{\text{cont}}^{\text{Untagged}}$	Number of continuum events in Untagged category	9225 ± 99
I_-	Coefficient of $ f(\rho^-) ^2 \sin(\Delta m_d \Delta t)$	-0.19 ± 0.11
I_+	Coefficient of $ f(\rho^+) ^2 \sin(\Delta m_d \Delta t)$	0.06 ± 0.11
U_0^+	Coefficient of $ f(\rho^0) ^2$	0.159 ± 0.046
U_-^-	Coefficient of $ f(\rho^-) ^2 \cos(\Delta m_d \Delta t)$	0.22 ± 0.16
U_-^+	Coefficient of $ f(\rho^-) ^2$	1.19 ± 0.12
U_+^-	Coefficient of $ f(\rho^+) ^2 \cos(\Delta m_d \Delta t)$	0.50 ± 0.17
$U_{+-}^{-,\text{Im}}$	Coefficient of $\text{Im}[f(\rho^+)f(\rho^-)^*] \cos(\Delta m_d \Delta t)$	0.25 ± 1.4
$U_{+-}^{-,\text{Re}}$	Coefficient of $\text{Re}[f(\rho^+)f(\rho^-)^*] \cos(\Delta m_d \Delta t)$	2.0 ± 1.2
$U_{+-}^{+,\text{Im}}$	Coefficient of $\text{Im}[f(\rho^+)f(\rho^-)^*]$	0.16 ± 0.70
$U_{+-}^{+,\text{Re}}$	Coefficient of $\text{Re}[f(\rho^+)f(\rho^-)^*]$	-0.26 ± 0.65
I_{+-}^{Im}	Coefficient of $\text{Im}[f(\rho^+)f(\rho^-)^*] \sin(\Delta m_d \Delta t)$	-5.2 ± 1.9
I_{+-}^{Re}	Coefficient of $\text{Re}[f(\rho^+)f(\rho^-)^*] \sin(\Delta m_d \Delta t)$	-0.3 ± 2.0
$U_{+0}^{+,\text{Im}}$	Coefficient of $\text{Im}[f(\rho^+)f(\rho^0)^*]$	0.25 ± 0.35
$U_{+0}^{+,\text{Re}}$	Coefficient of $\text{Re}[f(\rho^+)f(\rho^0)^*]$	-0.34 ± 0.39
$U_{-0}^{+,\text{Im}}$	Coefficient of $\text{Im}[f(\rho^-)f(\rho^0)^*]$	0.34 ± 0.43
$U_{-0}^{+,\text{Re}}$	Coefficient of $\text{Re}[f(\rho^-)f(\rho^0)^*]$	-0.98 ± 0.44

Table 7.4: Result after convergence of Run1-4 data fit. The arbitrary parameter U_+^+ is fixed to 1.

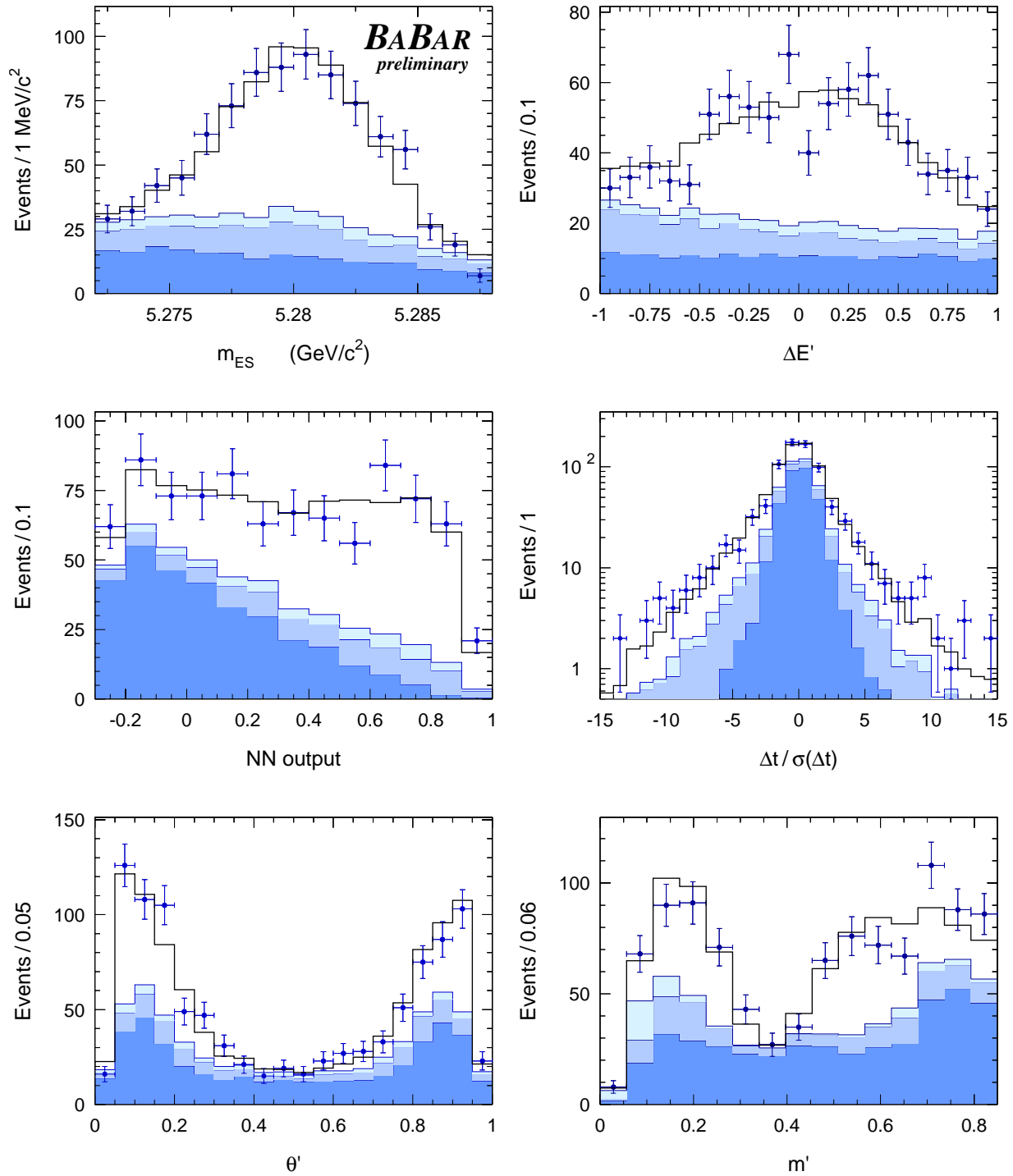


Figure 7.11: Distributions of the fit variables for samples enhanced in $\rho\pi$ signal using likelihood ratio cuts. The error bars represent data and the histograms with shading from light to dark are signal, B -backgrounds and continuum contributions.

Parameter	Description	Value
A_{CP}	Charge asymmetry in $B^0 \rightarrow \rho^\pm \pi^\mp$	-0.088 ± 0.049
C	Average of cosine coefficients in $B^0 \rightarrow \rho^+ \pi^-$ and $\rho^- \pi^+$	0.34 ± 0.11
ΔC	Half of difference betw. cos coeff. in $B^0 \rightarrow \rho^+ \pi^-$ and $\rho^- \pi^+$	0.15 ± 0.11
S	Average of sine coefficients in $B^0 \rightarrow \rho^+ \pi^-$ and $\rho^- \pi^+$	-0.10 ± 0.14
ΔS	Half of difference betw. sin coeff. in $B^0 \rightarrow \rho^+ \pi^-$ and $\rho^- \pi^+$	0.22 ± 0.15

Table 7.5: $Q2B$ parameters extracted from Us and Is coefficients from Run1-4 data fit.

$[-180^\circ; 180^\circ]$ for $\hat{\delta}$) is covered by a set of K discrete values whose compatibility with data is tested one by one with a constrained fit.

For the α -scan', Ts and Ps are floated; with $\alpha = \{\alpha_k\}_{k=1,\dots,K}$ as additional input, the values of Us and Is (UI^{scan}) are computed according to Equations 1.40 and the minimized chi-square is the following:

$$\chi_{\alpha \text{ scan}}^2 \equiv \sum_{i,j} [UI_i^{\text{data}} - UI_i^{\text{scan}}] (C^{\text{data}})^{-1} [UI_j^{\text{data}} - UI_j^{\text{scan}}] \quad (7.28)$$

where the sum is over the Us and Is parameters free in the data fit (UI^{data}). Accordingly, C^{data} is the covariance matrix computed by the fit to the data. The normalization condition $U_+^+ = 1$ is used as an additional constraint.

For each value of k between 1 and K , the fit provides a minimum chi-square $\chi_{\min}^2(k)$. Then one takes the minimum of these values χ_{\min}^2 and computes the χ^2 -difference: $\Delta\chi_{\min}^2(k) = \chi_{\min}^2(k) - \chi_{\min}^2$. The confidence level is finally obtained by computing the probability that this value is exceeded for a χ^2 -distribution with one degree of freedom.

The left plot in Figure 7.12 shows the α -scan, performed with an extended

correlation matrix, taking into account both statistical and systematic correlations – see Section 7.5 for details on systematics. It gives $\alpha = (113_{-17}^{+27} \pm 6)^\circ$ with the errors computed at a confidence level of 32%.

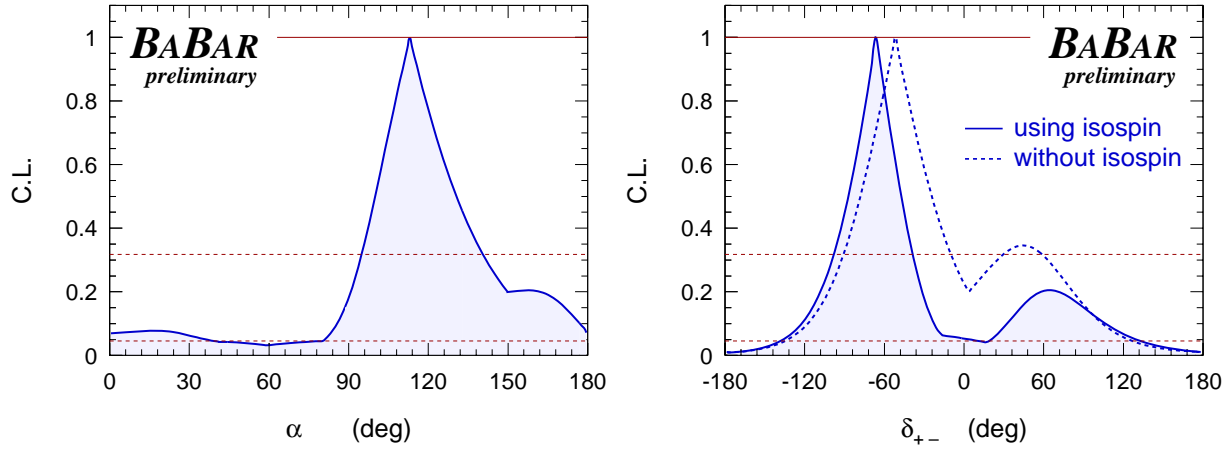


Figure 7.12: Confidence level functions for δ_{+-} (right) and α (left), including both statistics and systematic covariance matrices. Indicated by the dashed horizontal lines are the C.L. values corresponding to 1σ and 2σ , respectively.

For the $\hat{\delta}$ -scan, the procedure is very similar; the constraint is now that $\hat{\delta}$ must be equal to the discrete scan value at each step. In order to use all the information available, all fitted parameters are included in the chi-square and one uses the relation $\hat{\delta} = \arg(A^{+-*}A^{-+})$. The chi-square function is

$$\chi_{\hat{\delta} \text{ scan}}^2 \equiv \sum_{i,j} [UI_i^{\text{data}} - UI_i^{\text{scan}}] (C^{\text{data}})^{-1} [UI_j^{\text{data}} - UI_j^{\text{scan}}] + \left(\frac{\hat{\delta}^{\text{discrete}} - \hat{\delta}^{\text{scan}}}{\epsilon} \right)^2 \quad (7.29)$$

where ϵ is chosen to be small compared to the bin size of the scan.

The right plot in Figure 7.12 shows two $\hat{\delta}$ -scans using the fit results and taking into account both statistical and systematic uncertainties. The most constraining one is clearly given by the solid line which includes an additional SU(2)-based

relationship between the penguin contributions $P^{00} = -(P^{+-} + P^{-+})/2$. It gives $\delta_{+-} = (-67_{-31}^{+28} \pm 7)^\circ$, where the first errors are statistical and the second one systematic. Only a marginal constraint on δ_{+-} is obtained for C.L. < 0.05 .

7.5 Study of the Systematic Uncertainties

Since no attempt is made to re-measure the branching fractions in this analysis, the study of the systematic uncertainties concentrates on the CP measurement. The systematic effects are summarized in Table 7.6 for the U and I coefficients.

Vertex Resolution Function, Tagging and Signal Reconstruction

- **Δm_d and τ_{B^0} :** the systematic errors are obtained by varying incoherently the values of the B^0 oscillation frequency $\Delta m_d = (0.502 \pm 0.007) \text{ ps}^{-1}$ and the B lifetime $\tau_{B^0} = (1.536 \pm 0.014) \text{ ps}$ [53] within their experimental uncertainties.
- **Δt resolution function:** the parameters of the signal Δt resolution function are obtained from fits to fully reconstructed B decays. We determine the associated systematics by varying incoherently each parameter of the resolution model (scale factors, biases, fractions of tails, etc) by one standard deviation. Since the incoherent variation neglects the (mostly anti-) correlations that are present between the fit parameters, it is a conservative procedure.
- **Tagging:** the tagging efficiencies, mistag rates and mistag biases are obtained from fits to fully reconstructed B decays to flavor eigenstates. We determine the associated systematics by varying incoherently each parameter by one standard deviation of its experimental error.

	I_-	I_+	U_0^+	U_-^-	U_-^+	I_{+-}^{Im}	I_{+-}^{Re}	$U_{+0}^{+, \text{Im}}$
Δm_d	0.003	0.001	0.000	0.004	0.000	0.009	0.041	0.001
Δt signal model	0.004	0.003	0.001	0.005	0.000	0.043	0.028	0.003
Signal tagging fractions	0.000	0.001	0.001	0.000	0.000	0.015	0.010	0.002
Misreconstructed signal	0.002	0.001	0.001	0.001	0.000	0.082	0.015	0.003
Mistag probabilities	0.003	0.002	0.001	0.010	0.001	0.061	0.040	0.003
$N_{\text{Background}}$	0.002	0.002	0.007	0.004	0.003	0.089	0.036	0.006
B -bkg CP parameters	0.011	0.013	0.001	0.028	0.015	0.075	0.163	0.009
τ_B background modes	0.000	0.000	0.000	0.000	0.000	0.004	0.002	0.000
Signal m_{ES} and ΔE PDF	0.003	0.001	0.000	0.010	0.013	0.056	0.054	0.012
B -bkg tagging fractions	0.001	0.001	0.001	0.002	0.001	0.109	0.065	0.006
ρ mass and width	0.001	0.002	0.003	0.002	0.001	0.038	0.072	0.014
ρ' mass and width	0.001	0.004	0.001	0.001	0.002	0.061	0.230	0.026
Continuum PDF	0.004	0.003	0.003	0.002	0.012	0.009	0.071	0.016
Float class 10	-0.000	0.002	-0.040	-0.000	0.000	0.097	0.070	-0.010
Fixing 10 $\rho^0\pi^0$ parameters	0.003	0.003	0.025	0.019	0.007	0.024	-0.004	-0.110
ρ'' phase $+8^\circ$	0.001	-0.000	-0.009	-0.009	-0.003	0.018	-0.023	0.122
ρ'' amplitude $+30\%$	0.001	-0.002	-0.004	0.009	0.002	0.624	-0.212	-0.029
Non-resonant $+1\sigma$	-0.003	-0.001	0.005	-0.002	-0.001	-0.037	0.085	-0.005
Fit Bias	0.015	0.014	0.006	0.022	0.015	0.221	0.240	0.051
Sum	0.021	0.021	0.050	0.046	0.029	0.704	0.467	0.179

	U_+^-	$U_{+-}^{-, \text{Im}}$	$U_{+-}^{-, \text{Re}}$	$U_{+-}^{+, \text{Im}}$	$U_{+-}^{+, \text{Re}}$	$U_{+0}^{+, \text{Re}}$	$U_{-0}^{+, \text{Im}}$	$U_{-0}^{+, \text{Re}}$
Δm_d	0.001	-0.002	0.005	0.001	0.001	0.000	0.000	-0.001
Δt signal model	0.003	0.018	0.042	0.002	0.003	0.005	0.003	0.008
Signal tagging fractions	0.002	0.012	0.005	0.005	0.006	0.002	0.004	0.003
Misreconstructed signal	0.000	0.007	0.029	0.005	0.006	0.002	0.004	0.003
Mistag probabilities	0.010	0.040	0.018	0.007	0.009	0.006	0.003	0.006
$N_{\text{Background}}$	0.010	0.021	0.024	0.029	0.017	0.014	0.007	0.012
B -bkg CP parameters	0.033	0.020	0.053	0.041	0.024	0.037	0.037	0.036
τ_B background modes	0.000	0.003	0.005	0.001	0.001	0.001	0.001	0.001
Signal m_{ES} and ΔE PDF	0.010	0.037	0.022	0.012	0.042	0.028	0.048	0.013
B -bkg tagging fractions	0.004	0.114	0.041	0.042	0.023	0.007	0.007	0.005
ρ mass and width	0.002	0.036	0.047	0.018	0.014	0.030	0.008	0.043
ρ' mass and width	0.004	0.094	0.056	0.052	0.052	0.045	0.021	0.064
Continuum PDF	0.004	0.026	0.029	0.005	0.018	0.051	0.005	0.028
Float class 10	-0.002	-0.008	-0.012	-0.031	0.029	-0.031	-0.011	0.002
Fixing 10 $\rho^0\pi^0$ parameters	0.039	0.042	-0.022	-0.019	0.010	0.069	0.102	0.000
ρ'' phase $+8^\circ$	-0.011	-0.122	-0.054	0.018	0.064	0.045	0.078	0.113
ρ'' amplitude $+30\%$	0.002	-0.029	-0.106	0.053	0.098	0.064	0.070	0.076
Non-resonant $+1\sigma$	-0.016	-0.122	-0.065	0.008	0.048	-0.012	-0.001	0.035
Fit Bias	0.020	0.177	0.161	0.078	0.076	0.048	0.055	0.047
Sum	0.061	0.303	0.244	0.135	0.171	0.149	0.170	0.175

Table 7.6: *Summary of systematic uncertainties on the U_s and I_s coefficients.*

- **Fraction of misreconstructed events:** misreconstructed events mainly arise due to combinatorial background in the presence of soft photons or tracks at the formation of a signal candidate. The DP-averaged fraction of misreconstructed events has been verified for the Q2B analysis [37] with control samples of fully reconstructed $B \rightarrow D\rho$ events. It was found to be in good agreement with the Monte Carlo prediction:

$$f_{\text{SCF}}(\text{data-fitted})/f_{\text{SCF}}(\text{MC-counted}) = 1.04 \pm 0.05 \quad (7.30)$$

B-background

- **Branching fractions:** The expected event yields are varied incoherently for each B background class according to the expectation in Table 7.3.
- **CP parameters:** For each class of B -background, the relevant parameters describing CP violation are varied separately, taking into account measured values and their errors where available. In cases where no measurements are available, we vary the parameters by ± 0.3 .
- **PDFs:** We vary the effective lifetime for charged B decays by the errors obtained from Monte Carlo simulation.
- **Tagging parameters:** The tagging fractions for the background classes are obtained using MC simulation. For each class, the tagging fractions are varied incoherently by one standard deviation of the statistical uncertainties to obtain the associated systematic uncertainties.

Resonance Model

- **Mass and width of ρ and ρ' :** The mass and the width of $\rho(770)$ are varied by 2 MeV. The mass of the ρ' is varied by 15 MeV, and the width of the ρ' is varied by 50 MeV.
- **Contributions of ρ'' :** The contribution of the resonance $\rho(1700)$ to the dipion mass spectrum is varied by $\pm 30\%$. Its phase relative to the $\rho(770)$ is varied by 8° , which is two times the error we obtain when allowing this parameter to float in the fit.

Fit Model

- **Parameters for $\rho^0\pi^0$:** In the nominal fit we set the ten U and I coefficients that are related to the cosine and sine terms in the time dependence of the $\rho^0\pi^0$ contribution to zero. To estimate the systematic error of this assumption, we use high statistics toy Monte Carlo and an estimated $\rho^0\pi^0$ branching fraction of 1.9×10^{-6} to compare fits where these ten coefficients are fixed (to zero) and allowed to float freely.
- **Continuum parametrization using sideband:** The PDFs describing the $q\bar{q}$ continuum in the Dalitz plot are obtained from m_{ES} sidebands of the on-resonance data, corrected for residual contributions from B decays. To estimate the systematic effect of the extrapolation from the m_{ES} sideband into the signal region, we use high-statistics offpeak data with loose cuts on NN and ΔE . For the m_{ES} sideband and the signal region, we compare the DP variables and find no significant differences but only statistical fluctuations. These fluctuations are

parameterised, and the DP reweighted accordingly. We re-fit with this new DP shape to obtain the systematic uncertainties.

- **Non-resonant contribution:** A search for the non-resonant decay is performed in the center of the Dalitz plot. No significant signal is observed. We increase the non-resonant contribution by the observed statistical uncertainty and evaluate the associated error using Monte Carlo.

Fitting Incomplete Set of U 's and I 's

To assess the dependence of the results on whether all 27 parameters are free in the fit, or only the 16 most significant ones, we generate toy MC events using U 's and I 's that are consistent with the Q2B observable set and with a true value of $\alpha = 94^\circ$. At the maximum CL we find a difference of about 2° . The observed shift depends strongly on the amount of $\rho^0\pi^0$ in the sample. We use a $B^0 \rightarrow \rho^0\pi^0$ branching fraction of 10^{-6} in the estimation.

Correlation Matrix

The full correlation matrix for the systematic uncertainties considered above is shown in Tab. 7.7.

	I_-	I_+	U_0^+	U_-^-	U_-^+	U_{+-}^-	U_{+-}^{Im}	U_{+-}^{Re}	U_{+-}^{Im}	U_{+-}^{Re}	I_{+-}^{Im}	I_{+-}^{Re}	U_{+0}^{Im}	U_{+0}^{Re}	U_{-0}^{Im}
I_-	1.00														
I_+	0.33	1.00													
U_0^+	0.01	-0.06	1.00												
U_-^-	-0.08	0.03	0.00	1.00											
U_-^+	-0.22	0.05	0.02	0.24	1.00										
U_+^-	-0.10	0.01	0.03	0.41	0.22	1.00									
U_{+-}^{Im}	0.00	0.03	0.04	-0.01	0.03	0.03	1.00								
U_{+-}^{Re}	-0.03	0.10	0.08	0.13	0.14	0.12	0.06	1.00							
U_{+-}^{Im}	-0.01	-0.14	0.20	-0.04	-0.22	-0.04	-0.24	-0.15	1.00						
U_{+-}^{Re}	0.04	0.08	-0.22	0.10	0.08	0.02	-0.18	-0.14	0.10	1.00					
I_{+-}^{Im}	0.16	0.13	-0.24	-0.06	-0.09	-0.11	0.17	-0.14	-0.18	-0.00	1.00				
I_{+-}^{Re}	-0.02	0.13	-0.11	0.19	0.29	0.14	0.18	0.20	-0.33	-0.12	0.15	1.00			
U_{+0}^{Im}	-0.01	0.05	0.08	0.03	0.08	0.01	-0.04	0.02	0.05	0.06	-0.06	-0.03	1.00		
U_{+0}^{Re}	0.14	-0.12	0.16	-0.18	-0.43	-0.16	-0.15	-0.23	0.34	0.05	-0.06	-0.42	-0.01	1.00	
U_{-0}^{Im}	-0.09	-0.02	0.07	0.15	0.29	0.11	-0.08	0.01	-0.01	0.16	-0.11	-0.02	0.07	-0.09	1.00
U_{-0}^{Re}	0.07	-0.13	-0.06	-0.14	-0.31	-0.14	-0.25	-0.35	0.39	0.23	-0.01	-0.52	-0.01	0.49	-0.03

Table 7.7: Correlation matrix of systematic uncertainties for the U s and I s. Note that all elements above the diagonal are omitted for readability.

7.6 Conclusions

We have presented the preliminary measurement of CP -violating asymmetries in $B^0 \rightarrow \pi^+\pi^-\pi^0$ decays dominated by the ρ resonance. The results are obtained from a data sample of 213 million $\Upsilon(4S) \rightarrow B\bar{B}$ decays. We extend the previous quasi-two-body approach to a full time-dependent Dalitz plot analysis. From the measurement of the coefficients of 16 form factor bilinears, we determine the three CP -violating and two CP -conserving quasi-two-body parameters. We find evidence of direct CP violation at the level of 2.9σ . We measure the direct CP -violation parameters $\mathcal{A}_{\rho\pi} = -0.088 \pm 0.049 \pm 0.013$ and $C = 0.34 \pm 0.11 \pm 0.05$, where the first errors are statistical and the second systematic. For the mixing-induced CP -violation parameter, we find $S = -0.10 \pm 0.14 \pm 0.04$. For the dilution and strong phase shift parameters, we obtain $\Delta C = 0.15 \pm 0.11 \pm 0.03$ and $\Delta S = 0.22 \pm 0.15 \pm 0.03$ respectively.

Taking advantage of the interference between the ρ resonances in the Dalitz plot, we derive constraints on the relative strong phase between B^0 decays to $\rho^+\pi^-$ and $\rho^-\pi^+$, and on the angle α of the Unitarity Triangle. For the angle α we measure $(113_{-17}^{+27} \pm 6)^\circ$, while only a weak constraint is achieved at more than two standard deviations. Finally, for the relative strong phase δ_{+-} between the $B^0 \rightarrow \rho^-\pi^+$ and $B^0 \rightarrow \rho^+\pi^-$ transitions we find $(-67_{-31}^{+28} \pm 7)^\circ$, with a similarly weak constraint at two standard deviations and beyond. These measurements are consistent with the expectations from the CKM fit.

Appendix A

The theory of Standard Model

A.1 The Standard Model

According to the Standard Model of particle physics, matter is made up of six leptons and six quarks. These particles interact by exchanging bosons associated with the three fundamental forces: the strong force, the electromagnetic force and the weak force. We believe that these interaction can be understood as consequences of gauge symmetries.

Electromagnetic interaction

Quantum electrodynamics (QED) is the theory of electromagnetic interactions, which is a simple gauge theory. The theory can be formulated with a postulate of the invariance of the wave function under local phase rotation. The quantum mechanical equations of motion always involve derivatives of the wave function. In order for the derivatives to be also invariant under a local phase rotation, a vector field must be introduced. This vector field is called *gauge field*, and is referred to as the photon field in QED. Thus by using local gauge invariance as a dynamical principle, we have arrived at the conclusions that the electromagnetic field is necessary, and that the form

of interaction between the gauge field and matter prescribed by the gauge covariant derivative. Note that a mass term of the gauge field in the Lagrangian violates the gauge invariance. Therefore, that the photon is massless is a direct consequence of gauge invariance.

Strong interaction:

In the original work of Yang and Mills in 1954 [2], the non-Abelian gauge group was taken to be the $SU(2)$ group of *isotopic spin* rotations, and the vector fields were interpreted as the fields of strongly-interacting vector mesons of isotopic spin unity. Their proposal immediately encountered the obstacle that these vector mesons would have zero mass, like photons. Their ideas, however, proved fundamental. The modern version of the strong interactions, quantum chromodynamics (QCD), is another non-Abelian gauge field theory, based on a local color gauge group $SU(3)_c$. Similarly to QED, the theory can start with the postulate of $SU(3)$ invariance. The composite spinor is the color triplet quarks. Again gauge fields have to be introduced, and the $SU(3)_c$ gauge boson is the massless *gluon*.

Unlike in QED, the term in the Lagrangian that describes the interacting gauge field involves not only the bilinear terms of the gauge field but the trilinear and quadrilinear terms as well. These additional terms create three- and four-gauge-boson vertices, which is the consequence of the *non-Abelian* structure of the gauge group. The theory has a distinctive feature of *asymptotic freedom*. Asymptotic freedom implies that the interaction gets large at large distances which accounts for the fact that no free quark has been observed. Recently, there has been tremendous interest to understand quark confinement in the context of string theory where the confinement is achieved

by connecting quarks with strings in the extra dimensions, but this is outside the scope of this dissertation.

Weak interaction:

The weak interactions get their name from their intensity. Weak interactions at low energies are well described by an effective Lagrangian given by a sum of products of vector and axial vector charged currents. In 1973 the first discovery of neutrino events of the type $\bar{\nu}_\mu e^- \rightarrow \bar{\nu}_\mu e^-$ showed that there is a weak neutral current in addition to the charged weak current. Note here that unlike the charged current, the neutral current is not pure vector and axial vector current and has right-handed components. The complete theory to describe the weak interaction is achieved with its unification with the electromagnetic interaction.

Spontaneous symmetry breaking and electroweak theory:

Scalar fields ϕ play a fundamental role in the unified theories of the weak, strong, and electromagnetic interactions. Although mathematically simpler than spinor fields that describe fermions and vector fields that describe gauge bosons, the scalar field can experience *spontaneous symmetry breaking*. Some basic features of such fields can be found in the simplest theory of a one-component real scalar ϕ with the Lagrangian

$$\mathcal{L}_\phi = \frac{1}{2} (\partial_\mu \phi)^2 - \frac{m^2}{2} \phi^2 - \frac{\lambda}{4} \phi^4 \quad (\text{A.1})$$

where m is the mass of the scalar field and λ is the coupling constant. If the coupling $\lambda \ll 1$ and for small ϕ , we can ignore the interaction term in A.1. Thus the field satisfies the Klein-Gordon equation. The general solution of such equations can be expressed as a superposition of plane waves, corresponding to the propagation of

particles of a certain mass and momentum. It's clear that the field $\phi(x)$ will oscillate about the point $\phi = 0$ which is the minimum of the potential-energy density of the field ϕ . Now let's examine the same Lagrangian but with an opposite sign in front of the mass term.

$$\mathcal{L}_\phi = \frac{1}{2} (\partial_\mu \phi)^2 + \frac{\mu^2}{2} \phi^2 - \frac{\lambda}{4} \phi^4 \quad (\text{A.2})$$

Instead of oscillations about $\phi = 0$, the solution gives modes that grow exponentially near $\phi = 0$ due to the negative mass at $\phi = 0$. It suggests that the real minimum actually occurs at some other place, i.e. $\phi_c = \pm \mu/\sqrt{\lambda}$. Thus, even if the field ϕ is initially at zero, it soon undergoes a transition to a stable state with $\phi = \phi_c$ and this phenomenon is called spontaneous symmetry breaking.

The theory that correctly describes the experimental facts about the weak interaction was introduced by Glashow, Weinberg and Salam. It is a spontaneously broken gauge theory and this model gives a unified description of weak and electromagnetic interactions. The theory is based on the gauge group $\text{SU}(2) \times \text{U}(1)$. To break the $\text{SU}(2)$ symmetry spontaneously, we introduce the scalar Higgs field in the spinor representation of $\text{SU}(2)$, and this theory will lead to a system with no massless gauge bosons. When the $\text{U}(1)$ symmetry is imposed and the scalar field is assigned a charge $+1/2$ under this $\text{U}(1)$ symmetry, the complete gauge transformation is

$$\phi = \begin{pmatrix} \phi^+ \\ \phi^0 \end{pmatrix}, \quad \phi \rightarrow e^{i\alpha^a \tau^a} e^{i\beta/2} \phi. \quad (\text{A.3})$$

If the Higgs field ϕ acquires a vacuum expectation value of the form

$$\langle\phi\rangle = \frac{1}{\sqrt{2}} \begin{pmatrix} 0 \\ v \end{pmatrix}, \quad (\text{A.4})$$

the theory will now contain one massless gauge boson, corresponding the gauge transformation with $\alpha^1 = \alpha^2 = 0, \alpha^3 = \beta$ which leaves $\langle\phi\rangle$ invariant. The remaining three gauge bosons will acquire masses from this *Higgs mechanism*.

The masses of the gauge bosons can be worked out when the Lagrangian is evaluated at the scalar field vacuum expectation value. It is not possible to introduce the ordinary mass terms of the fermions into the Lagrangian because the left- and right-handed components of the various fermion fields have different gauge quantum numbers and such simple mass terms violate gauge invariance. However, the fermion mass terms can be introduced by invoking again the mechanism of spontaneous symmetry breaking. For the leptons, we can write the gauge-invariant coupling linking e_L , e_R and ϕ as the following:

$$\Delta\mathcal{L}_e = -\lambda_e \bar{E}_L \cdot \phi e_R + h.c. \quad (\text{A.5})$$

This is the *Yukawa coupling*. Indices L and R denote the left- and right-handed parts of the quark fields. Here the SU(2) indices of the doublets E_L and ϕ are contracted. The parameter λ_e is a new dimensionless coupling constant. If we replace ϕ in this expression by its vacuum expectation value in equation A.4, we obtain

$$\Delta\mathcal{L}_e = -\frac{1}{\sqrt{2}}\lambda_e v \bar{e}_L e_R + h.c. + \dots, \quad m_e = \frac{1}{\sqrt{2}}\lambda_e v \quad (\text{A.6})$$

Note that the way to construct the lepton mass automatically assures that the neutrinos are massless. There are strong indications that neutrinos do have tiny but non-zero masses. But for the purpose of the dissertation, we can safely ignore the masses of neutrinos. On the other hand, all the quarks are massive. The mass term of the quark fields can be written in the similar way but we have to consider that all the quarks are massive particles:

$$\Delta\mathcal{L}_q = -\lambda_d\bar{Q}_L \cdot \phi d_R - \lambda_u\epsilon^{ab}\bar{Q}_{La}\phi_b^\dagger u_R + h.c. \quad (\text{A.7})$$

Again substituting the vacuum expectations value of ϕ from equation A.4, these terms become

$$\Delta\mathcal{L}_q = -\frac{1}{\sqrt{2}}\lambda_d v \bar{d}_L d_R - \frac{1}{\sqrt{2}}\lambda_u v \bar{u}_L u_R + h.c. + \dots, \quad m_{u,d} = \frac{1}{\sqrt{2}}\lambda_{u,d}v \quad (\text{A.8})$$

A.2 Discrete symmetry transformation

Symmetries play an important role in physics. For example, invariance of physics under time or space translations leads to the conservation of energy and momentum, invariance under space rotation gives conservation of angular momentum. In addition to continuous Lorentz transformations, there are two other spacetime operations that are potential symmetries of the Lagrangian: *parity* and *time reversal*. They are discrete transformations and cannot be achieved by a series of infinitesimal transformations from the identity. There is another discrete operation: *charge conjugation*, which is not

a space-time transformation. Parity, denoted by P , sends $(t, \mathbf{x}) \rightarrow (t, -\mathbf{x})$, reversing the handedness of space but leaves spin and time unchanged. Time reversal, denoted by T , does the opposite, sending $(t, \mathbf{x}) \rightarrow (-t, \mathbf{x})$. Charge conjugation, denoted by C , interchanges particles and antiparticles without changing their spin orientation.

Although any relativistic field theory must obey Lorentz invariance, it need not be invariant under P , T and C . In 1956, T.D. Lee and C.N. Yang [3] investigated the validity of the parity conservation in elementary particle interactions and concluded that in the realm of weak interactions parity conservation was “only an extrapolated hypothesis unsupported by experimental evidence.” Subsequent experiments have unequivocally supported the idea that weak interactions in general do not conserve parity. Although parity conservation was found to be violated in weak interactions, the joint transformation CP remained an unbroken symmetry until 1964 when the first evidence for CP violation was found in the neutral kaon system [4]. As we shall soon see the Standard Model introduced in the previous section can account for CP violation, and also explain why the CP violating effect is so much weaker than the weak interactions, there is no convincing evidence that the origin of CP is indeed in the Standard Model. The work presented in this dissertation constitute part of the effort to explore the origin of CP violation.

Discrete symmetries in the Standard Model

If we ignore the Higgs scalar field and mass terms of the quarks, leptons and gauge bosons, the Lagrangian of the theory of quarks and leptons is entirely specified

by gauge invariance and renormalizability. We have

$$\mathcal{L} = -\frac{1}{4} \sum_i (F_{i\mu\nu}^\alpha)^2 + \sum_J \bar{\psi}_J (i\gamma^\mu D_\mu) \psi_J \quad (\text{A.9})$$

where the index i runs over the three factors of the gauge group and the index J runs over the various multiplets of chiral fermions. The couplings of the QCD gauge bosons are invariant to P , C and T separately. However, the couplings of SU(2) gauge bosons violate P and C maximally. Remember that SU(2) gauge bosons only couple to left-handed fermions and right-handed antifermions. P and C converts a particle that couples to SU(2) gauge bosons to one that does not. The combined operation CP interchanges left-handed particles with right-handed antiparticles, therefore, is a symmetry of A.9. Now let's put in the Higgs sector which will be responsible for the spontaneous breaking of SU(2)×U(1). The simplest but renormalizable model with one Higgs scalar field is

$$\mathcal{L}_\phi = (D_\mu \phi)^2 + \mu^2 \phi^\dagger \phi - \lambda (\phi^\dagger \phi)^2. \quad (\text{A.10})$$

This Lagrangian respects P , C and T .

Finally, we add the terms that couple the Higgs field to the quarks and leptons. Let's assume again here that the neutrinos are massless and generalize the A.5 to include more generations. When additional generations of leptons are introduced to the theory, there can be additional terms that mix generations,

$$\Delta \mathcal{L}_l = - \sum_{i,j} \lambda_l^{ij} \bar{E}_L^i \cdot \phi e_R^j + h.c. \quad (\text{A.11})$$

where λ_l^{ij} are general, and not necessarily symmetric or Hermitian. In order to diagonalize the coupling matrix λ_l , recall the general theorem that for any matrix m , it is always possible to choose unitary matrices A and B such that AmB is real and diagonal. After choosing unitary matrices U_l and W_l we can diagonalize the matrix λ_l to the real matrix U_l , $\lambda_l = U_l D_l W_l^\dagger$. Using the freedom to redefine the lepton field, $e'_L = U_l^\dagger e_L$, $\nu'_L = U_l^\dagger \nu_L$ and $e'_R = W_l^\dagger e_R$, we can easily see that in the matrix representation the Yukawa coupling is completely diagonal.

$$\begin{aligned}
\Delta\mathcal{L}_l &= -(\bar{E}_L \cdot \phi)\lambda e_R + h.c. \\
&= -(\bar{E}'_L \cdot \phi)U_l^\dagger(U_l D_l W_l^\dagger)W e'_R + h.c. \\
&= -\sum_i D^{ii} \bar{E}'^i_L \cdot \phi e'^i_R + h.c.
\end{aligned} \tag{A.12}$$

Notice our special choice of the redefined lepton field, where the left-handed fields of electrons and neutrinos are rotated by the the same matrix U_l . The mixing matrix U_l cancels out in both the neutral current $\bar{e}_L \gamma^\mu e_L \rightarrow \bar{e}'_L U_l^\dagger \gamma_\mu U_l e'_L = \bar{e}'_L \gamma^\mu e'_L$, and the charged current $\bar{\nu}_L \gamma^\mu e_L \rightarrow \bar{\nu}'_L U_l^\dagger \gamma_\mu U_l e'_L = \bar{\nu}'_L \gamma^\mu e'_L$. Therefore, the mixing matrices U_l and W_l disappear from the theory and the mass eigenstates of the leptons coincide with their flavor eigenstate. There is no way to produce CP violation in the lepton sector in the current framework.

The situation is a bit more complicated when quarks are involved. As in equation A.7, two independent couplings have to be introduced in order to generate mass for both up- and down-type quarks. The gauge invariant and renormalizable interactions

of the scalar doublets ϕ with the quarks take the form

$$\Delta\mathcal{L}_q = - \sum_{ij} \lambda_u^{ij} \bar{Q}_L^i \cdot \phi d_R^j + \sum_{ij} \lambda_d^{ij} \bar{Q}_L^i \cdot \phi^\dagger u_R^j + h.c., \quad (\text{A.13})$$

where λ_u^{ij} and λ_d^{ij} are unknown constants. The vacuum expectation values of ϕ then produce quark mass terms similar to equation A.8. Again, the matrices λ_u and λ_d are not constrained in any way unless there is additional symmetry imposed on the Lagrangian. Using the same trick to diagonalize the Higgs coupling in the lepton sector, we define matrices U 's and W 's such that $\lambda_u = U_u D_u W_u^\dagger$ and $\lambda_d = U_d D_d W_d^\dagger$ and matrices D 's are real and diagonal. After redefining the right handed quark fields by their corresponding W 's, i.e. $d'_R = W_d^\dagger d_R$ and $u'_R = W_u^\dagger u_R$, we find immediately that the matrices W 's are eliminated from the Higgs coupling A.13. Although the right handed quark fields also couple to the neutral gauge fields, different families of quarks share the same coupling to these gauge fields. Thus, the mixing induced by W 's commute with the corresponding covariant derivatives and we have

$$\begin{aligned} \sum_i \bar{u}_R^i (i\gamma_\mu D^\mu) u_R^i &= \sum_{i,j,k} \bar{u}_R^j W_u^{\dagger ji} (i\gamma_\mu D^\mu) W_u^{ik} u_R^k \\ &= \sum_{j,k} \bar{u}_R^j (i\gamma_\mu D^\mu) \left(\sum_i W_u^{\dagger ji} W_u^{ik} \right) u_R^k = \sum_{j,k} \bar{u}_R^j (i\gamma_\mu D^\mu) \delta_{j,k} u_R^k \\ &= \sum_i \bar{u}_R^i (i\gamma_\mu D^\mu) u_R^i \end{aligned} \quad (\text{A.14})$$

Similarly, W_d also drops out from the neutral coupling. Finally, both M 's disappear from the theory. We can also make an analogous transformation on the left-handed quark fields, i.e. $d'_L = U_d^\dagger d_L$ and $u'_L = U_u^\dagger u_L$. In the new mixed basis of quark fields,

U 's cancel in A.13. By the same logic as A.14, U 's drop out from the neutral gauge coupling with left-handed quarks fields. However, in this new basis for quark fields which diagonalizes the Higgs coupling, the flavor changing weak current takes the form

$$J_W^{\mu+} = \frac{1}{\sqrt{2}} \bar{u}_L^i \gamma^\mu d_L^i = \frac{1}{\sqrt{2}} \bar{u}_L^i \gamma^\mu (U_u^\dagger U_d)^{ij} d_L'^j = \frac{1}{\sqrt{2}} \bar{u}_L^i \gamma^\mu V^{ij} d_L'^j \quad (\text{A.15})$$

where the quark mixing matrix V is a unitary matrix. In general, CP violation could happen if the matrix V is complex but in certain cases the matrix can be made real by rotation of individual quark fields. It's instructive to understand what happens when there are only two generations of quarks, i.e. u, d, c, s . Remember that we have achieved the diagonalization of the Higgs coupling by introducing mixing matrices between generations, so we don't have the freedom to further mix quarks of different generations when we try to make the element of the mixing matrix real. But we are still allowed to introduce arbitrary phases for each individual quark field in the new mass basis. There are four quark fields in two generations. A generic 2×2 unitary matrix contains four parameters, one rotation angle and three phases. We can try to remove those phases by redefining three quark fields as $q_L^i \rightarrow \exp(i\theta^i)q_L^i$. A fourth such rotation for the fourth quark field has no effect as only the phase difference between quark fields matters. Therefore, a mixing matrix with two generations of quarks can always be made real and no CP violation is allowed in such theory. The only remaining free parameter in the mixing matrix is then the mixing angle θ_c , which is called the *Cabibbo angle* [5]. In reality, there are three families of fermions, and the quark mixing matrix contains 6 phases in addition to three rotation angles. This mixing matrix is called the Cabibbbo-Kobayashi-Maskawa (CKM) matrix [6]. Using

the above trick on the CKM matrix, one can remove only five of the six phases. It is possible that the quark coupling to the W gauge boson contains an irreducible complex coupling constant from the CKM matrix. Parametrizing V , as done by Kobayashi and Maskawa [6], we have

$$V = \begin{pmatrix} V_{ud} & V_{us} & V_{ub} \\ V_{cd} & V_{cs} & V_{cb} \\ V_{td} & V_{ts} & V_{tb} \end{pmatrix} = \begin{pmatrix} c_1 & -s_1 c_3 & -s_1 s_3 \\ s_1 c_2 & c_1 c_2 c_3 - s_2 s_3 e^{i\delta} & c_1 c_2 c_3 + s_2 c_3 e^{i\delta} \\ s_1 s_2 & c_1 s_2 c_3 + c_2 s_3 e^{i\delta} & c_1 s_2 s_3 - c_2 c_3 e^{i\delta} \end{pmatrix} \quad (\text{A.16})$$

where $c_i(s_i) = \cos \theta_i(\sin \theta_i)$, $i = 1, 2, 3$. If the phase δ does not vanish, CP is not a conserved symmetry in the weak interaction. Since CP violation requires both the weak interaction and the presence of a third generation of fermions, its effect is expected to be quite small in the Standard Model.

Appendix B

Isospin analysis of $B \rightarrow \pi\pi$

In order to understand how α can be extracted from decays involving $b \rightarrow u\bar{u}d$ transitions, we briefly investigate the simplest case of $B^0 \rightarrow \pi^+\pi^-$. $B^0 \rightarrow \pi^+\pi^-$ is a CP eigenstate with eigenvalue $+1$. If only a single weak decay amplitude contributes, that is if penguin contributions are negligible, then $\lambda(B \rightarrow \pi\pi)$ is a pure phase and $Im\lambda = \sin 2\alpha$. There is strong experimental evidence that penguins are significant in $B \rightarrow \pi\pi$, most notably the large branching fraction of $B^0 \rightarrow K^+\pi^-$ [17]. In the presence of penguin contributions, the phase of $\lambda_{\pi\pi}$ is modified by the relative strong phase $\delta_{\pi\pi} \equiv \arg(PT^*)$ between the penguin and the tree amplitudes. We can define the effective angle α_{eff} that incorporates the phase shift

$$\lambda_{\pi\pi} = e^{2i\alpha} \frac{1 - re^{-i(\alpha-\delta)}}{1 - re^{+i(\alpha+\delta)}} \equiv |\lambda_{\pi\pi}| e^{2i\alpha_{\text{eff}}} \quad (\text{B.1})$$

where r is modulus of the penguin over tree ratio. We see that the imaginary part of the $\lambda_{\pi\pi}$ does not directly probe α in the presence of gluonic penguins. The tool to separate the tree and penguin contributions is an isospin analysis [19]. In the basis of isospin I and the projection of isospin I_3 , isospin doublets $|B^0\rangle$ and $|B^+\rangle$ can be

denoted as:

$$|B^+\rangle = |\frac{1}{2}, +\frac{1}{2}\rangle, \quad |B^0\rangle = |\frac{1}{2}, -\frac{1}{2}\rangle \quad (\text{B.2})$$

And the relevant final states are

$$\begin{aligned} \langle \pi^+ \pi^0 | &= \sqrt{\frac{1}{2}} (\langle \pi_1^+ \pi_2^0 | + \langle \pi_1^0 \pi_2^+ |) = \langle 2, 1 | \\ \langle \pi^+ \pi^- | &= \sqrt{\frac{1}{3}} \langle 2, 0 | + \sqrt{\frac{2}{3}} \langle 0, 0 | \\ \langle \pi^0 \pi^0 | &= \sqrt{\frac{2}{3}} \langle 2, 0 | - \sqrt{\frac{1}{3}} \langle 0, 0 | \end{aligned} \quad (\text{B.3})$$

Note that because of Bose statistics, the $J = 0$ two-pion state produced in B decay has no $I = 1$ contribution. Isospin amplitudes $I_{\Delta I, I_f}$ can be labeled by the ΔI value of the b -quark decay and by the I_f of the final state, which includes the spectator quark. The key observation is that a gluon is pure $I = 0$, so that the dominant gluonic $b \rightarrow d$ penguins are pure $\Delta I = 1/2$. On the other hand, the tree-level $b \rightarrow u\bar{u}d$ decays have both $\Delta I = 3/2$ and $\Delta I = 1/2$ components. Thus, if the $\Delta I = 3/2$ piece can be isolated, then the tree contribution, which contains the weak phase to be measured, is thereby also isolated. The isospin decomposition for $B \rightarrow \pi\pi$ is given by

$$A^{+0} \equiv A(B^+ \rightarrow \pi^+ \pi^0) = \frac{\sqrt{3}}{2} A_{3/2,2} \quad (\text{B.4})$$

$$A^{+-} \equiv A(B^0 \rightarrow \pi^+ \pi^-) = \frac{1}{\sqrt{12}} A_{3/2,2} - \sqrt{\frac{1}{6}} A_{1/2,0} \quad (\text{B.5})$$

$$A^{00} \equiv A(B^0 \rightarrow \pi^0 \pi^0) = \frac{1}{\sqrt{3}} A_{3/2,2} + \sqrt{\frac{1}{6}} A_{1/2,0} \quad (\text{B.6})$$

Thus the three two-pion decay amplitudes depend only on two isospin amplitudes, hence there is one relationship,

$$\frac{1}{\sqrt{2}}A^{+-} + A^{00} = A^{+0} \quad (\text{B.7})$$

between them. They form a triangle on the complex plane. The amplitude for the CP -conjugate processes is obtained from the A amplitudes by simply changing the sign of the CKM phases; the strong phases remain the same. These amplitudes also form a triangle:

$$\frac{1}{\sqrt{2}}\bar{A}^{+-} + \bar{A}^{00} = \bar{A}^{+0} \quad (\text{B.8})$$

The measurements of the total rates and time-independent CP asymmetries in both B^\pm and B^0 decays determine the shapes of the two isospin triangles. The key observation is that, since the penguin diagram is purely $\Delta I = 1/2$, the A^{+0} amplitude receives contribution from only tree diagram. This means that $A^{+0} = e^{2i\alpha}A^{-0}$. This relation fixes the relative orientation of the two triangles up to an eight-fold discrete ambiguity. As a consequence, the complex ratio, $\kappa = e^{2i\alpha}\bar{A}^{+-}/A^{+-}$ is determined up to a eight-fold ambiguity. The CP asymmetry in $B^0 \rightarrow \pi^+\pi^-$ is given by

$$\text{Im}\lambda_{\pi^+\pi^-} = \text{Im} \left[e^{-2i\alpha}\kappa \right].$$

The quantity κ gives the penguin effect on the relationship between the angle α and the measured asymmetry. The angle α can in principle be extracted cleanly, even in the presence of penguins.

Appendix C

Dalitz plot

C.1 Introduction

We recall here the basic properties of the Dalitz plot as far as it is needed to motivate the various choices we have made. More detailed information is found, *e.g.*, in Ref. [22].

We consider the decay of a spin-zero B^0 with four-momentum p_B into the three daughters $\pi^+(p_+)$, $\pi^-(p_-)$, and $\pi^0(p_0)$, with corresponding four-momenta. The original number of 12 unknowns in the B^0 rest frame is reduced to 2, taking advantage of the known masses of the four particles involved (4), energy and momentum conservation (4) and the fact that two spatial angles are irrelevant (no direction is preferred) (2). Using the invariant-masses-squared as independent (Mandelstamm) variables

$$s_{+0} = (p_+ + p_0)^2, \quad s_{-0} = (p_- + p_0)^2, \quad (\text{C.1})$$

the invariant mass of the positive and negative pion, $s_{+-} = (p_+ + p_-)^2$, is obtained

from energy and momentum conservation:

$$s_{+-} = m_{B^0}^2 + 2m_{\pi^+}^2 + m_{\pi^0}^2 - s_{+0} - s_{-0} . \quad (\text{C.2})$$

The differential B^0 decay width with respect to the variables defined in Eq. (C.1) (*i.e.*, the *Dalitz plot*) reads

$$d\Gamma(B^0 \rightarrow \pi^+ \pi^- \pi^0) = \frac{1}{(2\pi)^3} \frac{|\mathcal{A}_{3\pi}|^2}{8m_{B^0}^3} ds_{+0} ds_{-0} , \quad (\text{C.3})$$

where $\mathcal{A}_{3\pi}$ is the Lorentz-invariant amplitude of the three-body decay. Note that a trivial integration over the spatial angles has been performed prior to Eq. (C.3). We now choose the notation $\{\text{DP}\}$ for the Dalitz plot coordinates $\{s_{+0}, s_{-0}\}$, and, correspondingly, $\{d\text{DP}\}$ for the Dalitz element $\{ds_{+0} ds_{-0}\}$. The symmetric boundaries of the Dalitz plot are obtained when, *e.g.*, for a $\rho^+ \rightarrow \pi^+ \pi^0$ resonance, \mathbf{p}_+ is parallel (minimum mass-squared) or anti-parallel (maximum mass-squared) to \mathbf{p}_0 . As a function of s_{+0} , the kinematic boundaries $s_{-0}[\text{max}]$ and $s_{-0}[\text{min}]$ are given by

$$s_{-0}[\text{max/min}](s_{+0}) = (E_-^* + E_0^*)^2 - \left(\sqrt{E_-^{*2} - m_{\pi^+}^2} \mp \sqrt{E_0^{*2} - m_{\pi^0}^2} \right)^2 , \quad (\text{C.4})$$

where

$$E_+^* = \frac{s_{+0} - m_{\pi^0}^2 + m_{\pi^+}^2}{2\sqrt{s_{+0}}} , \quad (\text{C.5})$$

$$E_0^* = \frac{s_{+0} - m_{\pi^+}^2 + m_{\pi^0}^2}{2\sqrt{s_{+0}}} , \quad (\text{C.6})$$

$$E_-^* = \frac{m_{B^0}^2 - s_{+0} - m_{\pi^+}^2}{2\sqrt{s_{+0}}} , \quad (\text{C.7})$$

are the energies in the ρ^+ rest frame. Numerically, the minimum and maximum masses squared are $s_{-0}[\text{max}] = (m_{B^0} - m_{\pi^+})^2 \simeq 26.418 (\text{GeV}/c^2)^2$ and $s_{-0}[\text{min}] = (m_{\pi^+} + m_{\pi^0})^2 \simeq 0.075 (\text{GeV}/c^2)^2$. Due to angular momentum conservation, the spin-one ρ resonance is polarized in a helicity-zero state. We therefore need to compute the cosine of the angle between the negative B^0 momentum in the ρ^+ rest frame (which is the flight direction of the ρ^+ resonance in the B^0 rest frame, and the negative flight direction of the π^+ in the B^0 rest frame) and the momentum \mathbf{p}_0^* of the π^0 in the ρ^+ rest frame. It is given by

$$\cos \theta_+ = \frac{2E_+^* E_-^* + 2m_{\pi^+}^2 - s_{+-}}{2|\mathbf{p}_+^*||\mathbf{p}_-^*|}, \quad (\text{C.8})$$

and an expansion as a function of the Dalitz variables s_{+0} , s_{-0} , leads to

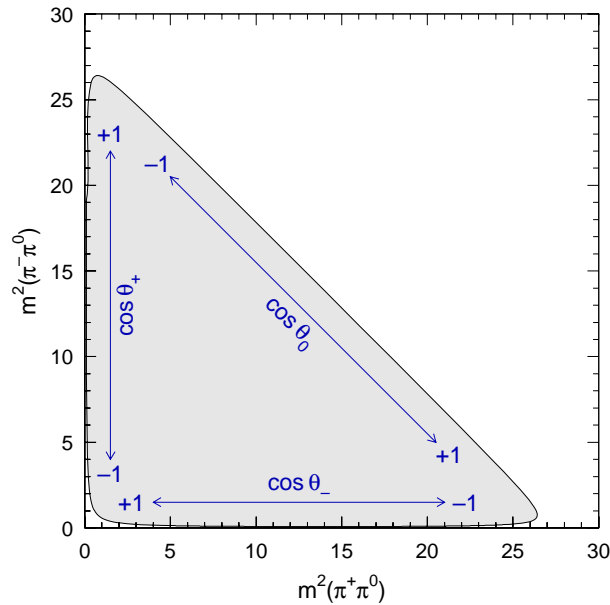


Figure C.1: *Convention adopted for the helicity angles. For vanishing relative strong phases it leads to destructive interference at all points in the Dalitz plot where at least two of the three mass combinations are equal. See text for a geometrical definition.*

$$\begin{aligned}
\cos \theta_+ &= [s_{+0}(s_{-0} - s_{+-}) - (m_{B^0}^2 - m_{\pi^+}^2)(m_{\pi^0}^2 - m_{\pi^+}^2)] \\
&\times \left[m_{\pi^+}^4 + (s_{+0} - m_{\pi^0}^2)^2 - 2m_{\pi^+}^2(s_{+0} + m_{\pi^0}^2) \right]^{-1/2} \\
&\times \left[m_{B^0}^4 + (s_{+0} - m_{\pi^+}^2)^2 - 2m_{B^0}^2(s_{+0} + m_{\pi^+}^2) \right]^{-1/2}, \quad (\text{C.9})
\end{aligned}$$

where s_{+-} is obtained from Eq. (C.2). Exchanging $s_{+0} \leftrightarrow s_{-0}$ in Eq. (C.9) yields the negative cosine of the helicity angle of the ρ^- , $-\cos \theta_-$, and replacing $s_{+0} \rightarrow s_{+-}$ together with $m_{\pi^0} \leftrightarrow m_{\pi^+}$ gives $-\cos \theta_0$ for the ρ^0 . Figure C.1 illustrates the convention we have adopted for the helicity angles:

- $\cos \theta_+(\rho^+)$ is defined as the angle between the π^0 in the ρ^+ rest frame and the ρ^+ flight direction in the B^0 rest frame.
- $\cos \theta_-(\rho^-)$ is defined as the angle between the π^- in the ρ^- rest frame and the ρ^- flight direction in the B^0 rest frame.
- $\cos \theta_0(\rho^0)$ is defined as the angle between the π^+ in the ρ^0 rest frame and the ρ^0 flight direction in the B^0 rest frame.

For vanishing relative strong phases, each resonance overlap comes with a relative minus sign so that maximal destructive interference is observed at all points with equal masses squared.

The amplitude $\mathcal{A}_{3\pi}$ contains all the underlying dynamics of the $B^0 \rightarrow \pi^+\pi^-\pi^0$ decay. In general, it is the coherent sum of one non-resonant term (\mathcal{A}_{NR}), which is (assumed to be) constant in the Dalitz plane, and multiple resonant amplitudes i ,

with different spins J , arbitrary real fractions and phase shifts, a_i , ϕ_i , and charge combinations $\{+0, -0, +- \}$:

$$\mathcal{A}_{3\pi}(\text{DP}) = a_{\text{NR}} e^{i\phi_{\text{NR}}} \mathcal{A}_{\text{NR}} + \sum_{\kappa\sigma \in \{+0, -0, +- \}} \sum_i a_i^{\kappa\sigma} e^{i\phi_i^{\kappa\sigma} J} \mathcal{A}_i^{\kappa\sigma}(\text{DP}) . \quad (\text{C.10})$$

Each resonant amplitude i can be written as a product of five terms

$${}^J\mathcal{A}_i^{\kappa\sigma}(\text{DP}) = {}^JF_{B,i} \cdot {}^JF_i(s_{\kappa\sigma}) \cdot {}^JK^{\kappa\sigma}(\text{DP}) \cdot {}^JF_{R,i}(s_{\kappa\sigma}) \cdot A_i^{\kappa\sigma} \quad (\text{C.11})$$

$$\equiv f_{\kappa\sigma}^{(i)}(\text{DP}) \cdot A_i^{\kappa\sigma} , \quad (\text{C.12})$$

where ${}^JF_{B,i}$ is a an irrelevant constant form factor for the B^0 decay, ${}^JF_i(s_{\kappa\sigma}) \equiv {}^JF(s_{\kappa\sigma})/{}^JF(m_i^2)$ is the ratio of Blatt-Weisskopf penetration form factors (see below), ${}^JK(\text{DP})$ is a kinematic function (see below), and ${}^JF_{R,i}(\text{DP})$ is a relativistic Breit-Wigner function given by

$${}^JF_{R,i}(s_{\kappa\sigma}) = \frac{1}{s_{\kappa\sigma} - m_i^2 + im_i {}^J\Gamma_i(s_{\kappa\sigma})} . \quad (\text{C.13})$$

The s -dependent (“running”) width is defined as

$${}^J\Gamma_i(s_{\kappa\sigma}) = \Gamma_i^0 \frac{m_i}{\sqrt{s_{\kappa\sigma}}} \left(\frac{k_\pi(s_{\kappa\sigma})}{k_\pi(m_i^2)} \right)^{2J+1} \frac{{}^JF(Rk_\pi(s_{\kappa\sigma}))}{{}^JF(Rk_\pi(m_i^2))} , \quad (\text{C.14})$$

where m_i is the mass of the resonance i , $\Gamma_i^0 = \Gamma_i(m_i^2)$ its width, and where

$$k_\pi(s_{\kappa\sigma}) = \frac{\sqrt{s_{\kappa\sigma}}}{2} \left(1 - \frac{(m_a + m_b)^2}{s_{\kappa\sigma}} \right)^{1/2} \left(1 - \frac{(m_a - m_b)^2}{s_{\kappa\sigma}} \right)^{1/2} , \quad (\text{C.15})$$

is the momentum of the resonance decay particles in the resonance frame. The functions ${}^J F(Rk_\pi(s_{\kappa\sigma}))$ are the nuclear *Blatt-Weisskopf penetration factors* [24]¹.

The kinematic function in Eq. (C.11) depends on the spin of the resonance. For a B decay into a vector resonance $\{\kappa\sigma\}$ and a bachelor track $\{c\}$, it is given by

$$\begin{aligned} {}^1 K^{\kappa\sigma}(\text{DP}) &= (p_{B^0} + p_c)_\mu \sum_i \epsilon_i^\mu(p_{\kappa\sigma}) \epsilon_i^{\nu*}(p_{\kappa\sigma}) (p_\kappa - p_\sigma)_\nu \\ &= s_{\kappa\tau} - s_{\sigma\tau} + \frac{1}{s_{\kappa\sigma}} (m_{B^0}^2 - m_\tau^2) (m_\sigma^2 - m_\kappa^2) \\ &= -4|\mathbf{p}_\kappa||\mathbf{p}_\tau| \cos \theta_{\kappa\tau} , \end{aligned} \tag{C.17}$$

where all four-momenta p_i are given in the resonance frame and $\theta_{\kappa\tau}$ is the helicity angle, and where we have used the relation

$$\sum_i \epsilon_i^\mu(p) \epsilon_i^{\nu*}(p) = -g^{\mu\nu} + \frac{p^\mu p^\nu}{p^2} , \tag{C.18}$$

for the sum over the polarization four-vectors. The last two lines of Eq. (C.17) reproduce the convention for the cosines of the helicity angles defined in Eq. (C.8) and

¹They are semi-classical and motivated by the potential $\hbar L(L+1)/(2mr^2)$ occurring in Schrödinger's Equation, expressed in spherical coordinates, for the scattering of a particle with orbital angular momentum $L > 0$ in a central field. The repulsive potential is equivalent to a rotation energy and can thus be denoted a *centrifugal barrier*. For growing L , or decreasing radial distance r , the centrifugal barrier increases, which entails decreasing transition probability. One can empirically determine a radial distance, called *interaction radius*, R , of the resonance, which separates an outside region (with respect to the centrifugal barrier), with little interaction, from an inside region where the interaction between the particles is strong [25]. The transmission coefficients of the centrifugal barrier are the Blatt-Weisskopf factors. They are derived using spherical Bessel and Hankel functions and read for the lowest orbital momenta (spins):

$${}^0 F = 1 , \quad {}^1 F(x) = \frac{1}{1+x^2} , \quad {}^2 F(x) = \frac{1}{9+3x^2+x^4} . \tag{C.16}$$

We choose $R = 1.5 \text{ GeV}^{-1} \simeq 0.3 \text{ fm}$ in the following for all resonances.

Fig. C.1. Note that the occurrence of $\cos \theta_{\kappa\tau}$ in the propagator substantially enhances the interference between the different ρ bands in the Dalitz plot, and thus increases the sensitivity of this analysis [20]. Equivalently, one obtains for scalar and tensor resonances the kinematic functions

$${}^0K^{\kappa\sigma} = 1, \quad (\text{C.19})$$

$${}^2K^{\kappa\sigma}(\text{DP}) = \frac{8}{3} |\mathbf{p}_\kappa|^2 |\mathbf{p}_\tau|^2 (3 \cos^2 \theta_{\kappa\tau} - 1). \quad (\text{C.20})$$

The likelihood fit will determine a global signal yield, which multiplies the coherent amplitude sum (C.10).

To quantify the sub-yields of the different contributors to the model, we define the fraction η_i for the amplitude i by

$$\eta_i \equiv \frac{\langle |a_i^{\kappa\sigma} e^{i\phi_i^{\kappa\sigma}} \mathcal{A}_i^{\kappa\sigma}(\text{DP})|^2 \rangle}{\langle |\mathcal{A}_{3\pi}(\text{DP})|^2 \rangle}, \quad (\text{C.21})$$

where the expectation values are obtained from high-statistics Monte Carlo integration of the Dalitz plot (C.3). Because of interference, the sum $\sum_i \eta$ of the fractions for all components will in general not be one.

C.2 The Square Dalitz Plot

Due to the low final state masses, $m_\rho \ll m_{B^0}$, signal events populate the kinematic boundaries of the Dalitz plot. It turns out that due to combinatorics, the dominant $e^-e^- \rightarrow q\bar{q}$ ($q = u, d, s, c$) continuum background also accumulates at the boundaries so that the representation Eq. (C.3) turns out to be inadequate when one

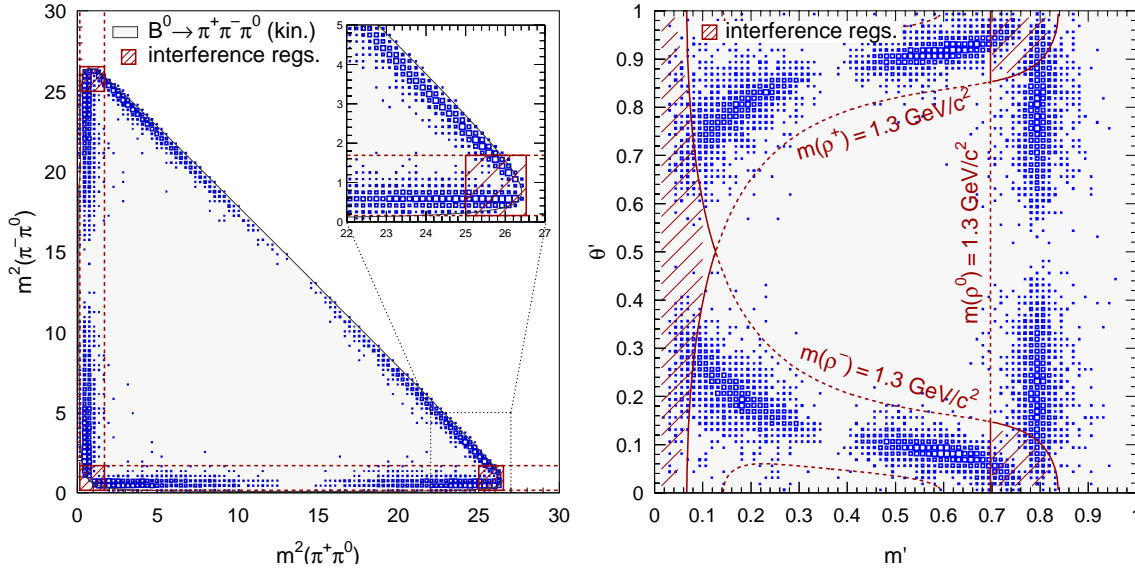


Figure C.2: *Nominal (left) and square (right) $B^0 \rightarrow \pi^+ \pi^- \pi^0$ Dalitz plots obtained from toy Monte Carlo without detector simulation. The generating amplitudes are $T^{+-} = T^{-+} = T^{00} = 1$ and $P^{+-} = P^{-+} = P^{00} = 0$. The hatched areas indicate the main overlap regions between the different ρ bands, which are removed in the quasi-two-body analyses. The destructive interference at equal ρ masses appears clearly. The contour lines correspond to the cuts $0.4 < m_{\rho^{+-,0}} < 1.3 \text{ GeV}/c^2$.*

wants to use empirical reference shapes in a likelihood fit. We therefore apply the concept of a square Dalitz plot (denoted *square DP* or *SDP* in the following) [26] and transform

$$ds_{+0} ds_{-0} \longrightarrow |\det J| dm' d\theta', \quad (\text{C.22})$$

where

$$m' \equiv \frac{1}{\pi} \arccos \left(2 \frac{m_{+-} - m_{+-}[\min]}{m_{+-}[\max] - m_{+-}[\min]} - 1 \right), \quad \text{and} \quad \theta' \equiv \frac{1}{\pi} \theta_{+-}, \quad (\text{C.23})$$

where m_{+-} is the invariant mass between the charged tracks, $m_{+-}[\max] = m_{B^0} - m_{\pi^0}$ and $m_{+-}[\min] = 2m_{\pi^+}$ are the boundaries of m_{+-} , θ_{+-} is the angle between the positive track and the negative B momentum in the $\{+-\}$ rest frame, and J is the

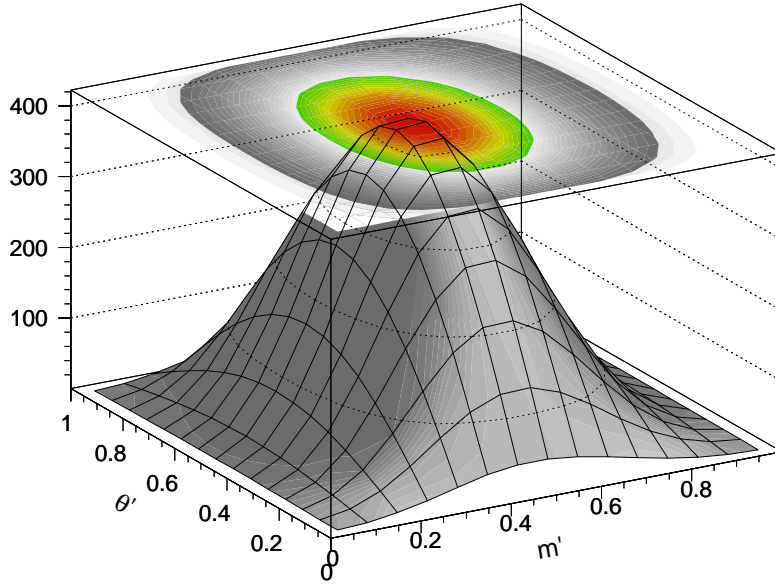


Figure C.3: *Jacobian determinant (C.24) of the transformation (C.22). The plot shows the distribution one would obtain in the square Dalitz plot for a uniform (non-resonant) prior in the nominal Dalitz plot.*

Jacobian of the transformation. The new variables have validity ranges between 0 and 1. The determinant of the Jacobian is given by

$$|\det J| = 4 |\mathbf{p}_+^*| |\mathbf{p}_0^*| m_{+-} \cdot \frac{\partial m_{+-}}{\partial m'} \cdot \frac{\partial \cos \theta_{+-}}{\partial \theta'} , \quad (\text{C.24})$$

where $|\mathbf{p}_+^*| = \sqrt{E_+^* - m_{\pi^+}^2}$ and $|\mathbf{p}_0^*| = \sqrt{E_0^* - m_{\pi^0}^2}$, and where the energies E_+^* and E_0^* are in the $\{+-\}$ rest frame. The partial derivatives in Eq. (C.24) read

$$\frac{\partial m_{+-}}{\partial m'} = -\frac{\pi}{2} \sin(\pi m') (m_{+-}[\text{max}] - m_{+-}[\text{min}]) \quad \text{and} \quad \frac{\partial \cos \theta_{+-}}{\partial \theta'} = -\pi \sin(\theta' \pi) . \quad (\text{C.25})$$

Figure C.2 shows the original and the transformed Dalitz plots for toy Monte Carlo $B^0 \rightarrow \pi^+ \pi^- \pi^0$ events generated according to Eqs. (1.35) and (1.36). The hatched areas

indicate the main overlap regions between the different ρ bands, which are removed in the quasi-two-body analyses. The plots illustrate the homogenization of the Dalitz plot obtained after the transformation (C.22). The determinant of the Jacobian (C.24) is shown in Fig. C.3. It is the distribution one would obtain in the square Dalitz plot for a uniform (non-resonant) prior in the nominal Dalitz plot (DP).

Note that the transformation (C.22) is not symmetric over the Dalitz plot, the ρ^+/ρ^- overlap region is treated with priority since it corresponds to the most problematic zone where the π^0 energy is small and combinatorial background is enhanced.

C.3 The Signal Model for $B^0 \rightarrow \pi^+\pi^-\pi^0$

We have introduced the kinematic properties together with a simple Breit-Wigner model of the pion form factor in the previous Section. We will use this formalism to describe the concrete signal parameterization adopted in the analysis. It is denoted *nominal signal model* in the following.

C.3.1 Vector Form Factor

The dominant contribution to the $B^0 \rightarrow \pi^+\pi^-\pi^0$ amplitude stems from vector resonances, namely the $\rho(770)$ and its radial excitations. A large number of parameterizations can be found in the literature, most of which are capable to describe precise data from $e^-e^- \rightarrow \pi^+\pi^-$ annihilation or $\tau^+ \rightarrow \bar{\nu}_\tau \pi^+\pi^0$ decays. We consider two models in this analysis. Both represent analytical functions with a branch cut along the real axis beginning at threshold ($4m_{\pi^+}^2$ for a neutral resonance and $(m_{\pi^+} + m_{\pi^0})^2$ for a charged resonance). Note that we will apply the empirical Blatt-Weisskopf penetration factor correction of the s -dependent width given in Eq. (C.14) for systematic

studies, since we merely deal with low spin resonances.

- We denote by **RBW** the relativistic Breit-Wigner ansatz for a resonance R introduced for the vector form factor,

$$^1F_R^{\text{RBW}}(s) = \frac{1}{s - m_R^2 + i m_R \Gamma_R(s)} , \quad (\text{C.26})$$

where the s -dependendent width $\Gamma_R(s)$ is given in Eq. (C.14) for $J = 1$, and ignoring the ratio of the Blatt-Weisskopf factors.

- We denote by **GS** the main approach used in the analysis. It is the Gounaris-Sakurai (GS) parameterization [27] of the p -wave scattering amplitude for a broad resonance R , decaying to the final state pions $\pi_1\pi_2$:

$$^1F_R^{\text{GS}}(s) = \frac{1 + d \cdot \Gamma_R/m_R}{s - m_R^2 - f(s) + i m_R \Gamma_R(s)} , \quad (\text{C.27})$$

where

$$f(s) = \Gamma_R \frac{m_R^2}{k_\pi^3(m_R^2)} \left[k_\pi^2(s) (h(s) - h(m_R^2)) + (m_R^2 - s) k_\pi^2(m_R^2) \frac{dh}{ds} \Big|_{s=m_R^2} \right] , \quad (\text{C.28})$$

and where $k_\pi(s)$ is the pion momentum in the R rest frame (C.15). The s -dependence is as in the RBW model. The function $h(s)$ is defined as

$$h(s) = \frac{2}{\pi} \frac{k_\pi(s)}{\sqrt{s}} \ln \left(\frac{\sqrt{s} + 2k_\pi(s)}{2m_\pi} \right) , \quad (\text{C.29})$$

with

$$dh/ds|_{m_R^2} = h(m_R^2) [(8k_\pi^2(m_R^2))^{-1} - (2m_R^2)^{-1}] + (2\pi m_R^2)^{-1} . \quad (\text{C.30})$$

The normalization condition at ${}^1F_{R,i}^{\text{GS}}(0)$ fixes the parameter $d = f(0)/(\Gamma_R m_R)$.

It is found to be [27]

$$d = \frac{3}{\pi} \frac{m_\pi^2}{k_\pi^2(m_R^2)} \ln \left(\frac{m_R + 2k_\pi(m_R^2)}{2m_\pi} \right) + \frac{m_R}{2\pi k_\pi(m_R^2)} - \frac{m_\pi^2 m_R}{\pi k_\pi^3(m_R^2)} . \quad (\text{C.31})$$

As imposed by unitarity, the GS parameterization satisfies the relation

$$\tan \delta_1^1(s) = \frac{\text{Im} {}^1F_R^{\text{GS}}(s)}{\text{Re} {}^1F_R^{\text{GS}}(s)} , \quad (\text{C.32})$$

where $\delta_1^1(s)$ is the phase shift of $l = 1$, $I = 1$ $\pi\pi$ scattering form factor.

C.3.2 Scalar Form Factor

As pointed out by many authors (see, *e.g.*, Refs [28, 29, 30]), the experimental smallness of the ratio

$$R \equiv \frac{\mathcal{B}(B^+ \rightarrow \rho^0 \pi^+)}{\mathcal{B}(B^0 \rightarrow \rho^\pm \pi^\mp)} = 2.38_{-0.40}^{+0.49} , \quad (\text{C.33})$$

compared with the naive expectation from form factor arguments, could be due to significant scalar contributions to the decay $B^\pm \rightarrow \rho^0 \pi^\pm$, which due to experimental cuts must be either broad - or in the close vicinity of the ρ resonance. Though scalar contributions are expected to be significantly smaller in $B^0 \rightarrow \pi^+ \pi^- \pi^0$ than they are

in $B^\pm \rightarrow \rho^0 \pi^\pm$ (about a factor of up to hundred [29, 30]), we must consider a possible contribution in the signal amplitude. Their relative fractions will be treated as free and unbound parameters in the fit. Note that scalar contributions are potentially harmful since they violate the isospin relation (1.37), if not properly taken into account.

For the resonances of the scalar, isoscalar f family, $f_0(980)$, $f_0(1370)$..., a simple Breit-Wigner shape parameterization is inappropriate because of the opening of the $K\bar{K}$ threshold (and the $\eta\eta$ threshold, which is however neglected here). We therefore use a coupled-channel Breit-Wigner (CCBW) propagator, following the parameterization of the WA76 and E791 Collaborations [50, 51],

$${}^0F_{f_0}^{\text{CCBW}}(s_{+-}) = \frac{1}{s_{+-} - m_{f_0}^2 + i m_{f_0} (\Gamma_\pi(s_{+-}) + \Gamma_K(s_{+-}))}, \quad (\text{C.34})$$

and using s -dependent widths according to Eq. (C.14),

$$\Gamma_\pi(s_{+-}) = \Gamma_{f_0,\pi} \frac{m_{f_0}}{\sqrt{s_{+-}}} \frac{k_\pi(s_{+-})}{k_\pi(m_{f_0}^2)}, \quad (\text{C.35})$$

$$\Gamma_K(s_{+-}) = \Gamma_{f_0,K} \frac{m_{f_0}}{\sqrt{s_{+-}}} \frac{k_{K^+}(s_{+-}) + k_{K^0}(s_{+-})}{k_\pi(m_{f_0}^2)}, \quad (\text{C.36})$$

where the $k_{\pi/K}(s)$ function is defined in Eq. (C.15). The E791 Collaboration determines the model parameters in fits to $D_s^+ \rightarrow \pi^+ \pi^- \pi^+$ decays [51]. They find $m_{f_0(980)} = (977 \pm 4) \text{ MeV}/c^2$, and $g_\pi = 0.09 \pm 0.01$ and $g_K = 0.02 \pm 0.05$, where it has been absorbed into a constant $g_\pi = \Gamma_{f_0,\pi} m_{f_0} / (s_{+-} - \sqrt{m_{f_0}^2/4 - m_{\pi^+}^2})$ (and correspondingly for $\pi \leftrightarrow K$). With these values, the alteration of the form factor via (C.36), introduced by the opening of the $K\bar{K}$ branch, is hardly distinguishable from the $\pi^+ \pi^-$ -

only form factor, both for modulus and phase in the Argand diagram. More massive scalar f resonances can be parameterized with the nominal Breit-Wigner propagator (C.13) using the RBW model.

C.3.3 Higher Resonances

Higher vector resonances are known to contribute to the $\pi\pi$ final state in e^-e^- annihilation and τ decays (see, *e.g.*, [44, 45]). They are introduced into the model via the coherent amplitude sum (C.10). As an example, the $e^-e^- \rightarrow \pi^+\pi^-$ form factor can be written as ([45, 46])

$$F_\pi(s) \propto F_{\rho(770)}(s) \left(\frac{1 + a_{\rho\omega} e^{i\phi_{\rho\omega}} F_{\omega(782)}(s)}{1 + a_{\rho\omega}} \right) + a_{\rho'} e^{i\phi_{\rho'}} F_{\rho(1450)}(s) + a_{\rho''} e^{i\phi_{\rho''}} F_{\rho(1700)}(s) , \quad (\text{C.37})$$

where the F functions can be GS form factors (C.27) that must be normalized to $F(0) = 1$ due to charge conservation.

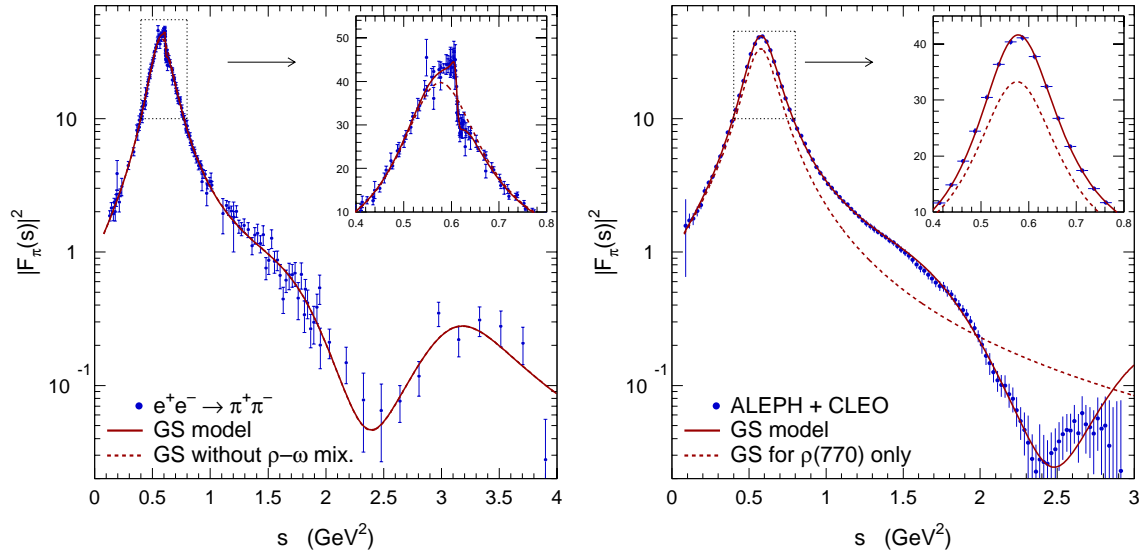


Figure C.4: Pion form factor from $e^+e^- \rightarrow \pi^+\pi^-$ annihilation (left) and $\tau^+ \rightarrow \bar{\nu}_\tau \pi^+ \pi^0$ decays (right).

Figure C.4 shows on the left hand side a fit of the model (C.37) to newest $e^-e^- \rightarrow \pi^+\pi^-$ annihilation data, where the most precise measurements are provided by the CMD2 Collaboration [47]. In these fits, the relative phases between the ρ resonances have been set to π - as expected from simple radial excitation. The complete fit results are given in Table 1.1. Agreement is observed between the model and the data points. The shoulder originates from the significant $\rho(1450)$ contribution. The additional peak at large masses corresponds to the $\rho(1700)$, measured by the DM2 Collaboration [48]. The sharp cut around $780 \text{ MeV}/c^2$ is due to but the interference between the $\rho(770)$ and the $\omega(782) \rightarrow \pi^+\pi^-$ amplitude. The right hand plot in Figure C.4 shows a fit of the same model (but without the isoscalar $\omega(783)$ amplitude) to the charged ρ^+ measured in τ decays [49]. Again, agreement is observed. Also shown is the form factor (C.37) when setting $a_{\rho'} = a_{\rho''} = 0$.

C.3.4 Killer modes

Small contributions are expected from the following phenomena.

The σ resonance

Not only the apparently small ratio (C.33), but also indirect observation in fits to the $D^+ \rightarrow \pi^+\pi^-\pi^+$ Dalitz plot, performed by the E791 Collaboration [52], point towards the existence of a light broad scalar and isoscalar resonance denoted σ (or $f_0(400-1200)$ [12]). E791 performs two DP fits, one without and another one with a free varying $\sigma\pi^+$ contribution. Both fits also determine a non-resonant amplitude. While the first fit finds a non-resonant amplitude fraction of 0.39 ± 0.10 (no $\sigma\pi^+$ allowed), the second fit reduces it to 0.08 ± 0.07 while it yields a $\sigma\pi^+$ fraction of 0.46 ± 0.09 , and a greatly improved χ^2 . The parameters of this “ $\sigma(500)$ ” state are determined to

be $m_{\sigma(500)} = (478_{-23}^{+24} \pm 17) \text{ MeV}/c^2$ and $\Gamma_{\sigma(500)} = (324_{-40}^{+42} \pm 21) \text{ MeV}/c^2$. Theoretical tree-level calculations within factorization [29] suggest a σ contribution to the decay $B^+ \rightarrow \pi^+\pi^-\pi^+$ of the order of $2\text{-}4 \cdot 10^{-6}$, and a $B^+ \rightarrow \rho^0\pi^+$ branching fraction of the order of $3.5\text{-}4.0 \cdot 10^{-6}$, depending on the width of the σ resonance and the form factor model used. The combined branching fraction $B^+ \rightarrow (\rho^0 + \sigma)\pi^+$ is predicted to be $6\text{-}11 \cdot 10^{-6}$, in agreement with *BABAR*'s recent $B^+ \rightarrow \rho^0\pi^+$ measurement. However, one has to consider that a (possible) σ contribution would not be efficiency corrected in the measurement, so that an inclusive $(\rho + \sigma)$ measurement would have lower efficiency.

The σ contribution is expected to be significantly smaller in neutral B decays². The same authors [29] predict the $B^0 \rightarrow \rho^0\pi^0$ branching fraction to be of the order of $0.5\text{-}1.0 \cdot 10^{-6}$, and a 10-20 times smaller σ contribution to the decay $B^0 \rightarrow \pi^+\pi^-\pi^0$. Similar results are obtained in Ref. [30].

Heavy B mesons

Again triggered by the small ratio (C.33), the authors of Ref. [28] (see also Ref. [30]) advocate that, in addition to the broad σ resonance, off-shell heavy-meson resonances like the axial-vector B^* (or a scalar B_0) could enhance the $B^+ \rightarrow \rho^0\pi^+$ branching fraction. Since the B^* is almost mass-degenerate with the B^0 meson, it is argued that tails of the resonance could give rise to sizable effects in B^0 decays into light final states. Moreover, this may be enhanced since it is expected that the strong coupling between a B , a B^* and a pion may be large. The decay picture is as follows: for the B^* intermediate state, there is a strong emission of a pion, followed by the

²In the charged decay $B^+ \rightarrow (\sigma \rightarrow \pi^-\pi^+)\pi^+$, the amplitudes from the exchange of the π^+ add coherently due to the presence of two identical pions in the final state. This leads to the enhancement of the branching fraction with respect to the neutral decay $B^0 \rightarrow (\sigma \rightarrow \pi^+\pi^-)\pi^0$ [29].

weak decay of a virtual B^* into a pion pair; for the ρ intermediate state there is a weak decay of $B \rightarrow \rho\pi$ followed by the strong decay $\rho \rightarrow \pi\pi$ [28].

In disagreement with the results of Ref. [28] it is pointed out in Ref. [30] that taking into account the off-shellness of the intermediate resonances, reduces significantly their contribution to $B^0 \rightarrow \rho^0\pi^0$. The numerical analysis of Ref. [30], performed within QCD factorization, leads to the small $\mathcal{B}(B^0 \rightarrow \rho^0\pi^0) = 0.03 \cdot 10^{-6}$ when taking into account the off-shellness of the B^* meson, and to the ten times larger $\mathcal{B}(B^0 \rightarrow \rho^0\pi^0) = 0.39 \cdot 10^{-6}$ when neglecting the off-shell suppression.

Bibliography

- [1] A.D. Sakharov, JETP Letters, vol.5, pp32-5 (1967)
- [2] C.N. Yang and R.L.Mills, Phys. Rev. **96** 191 (1954)
- [3] T.D. Lee and C.N. Yang, Phys. Rev. **104** 254 (1956)
- [4] J.H. Christenson, J.W. Cronin, V.L. Fitch and R. Turlay, Phys. Rev. Lett. **13** 138 (1964)
- [5] N. Cabibbo Phys. Rev. Lett. **10** 531 (1963)
- [6] M. Kobayashi and T. Maskawa, Prog. Theor. Phys. **49**, 652(1973)
- [7] C.L. Bennett et al., ApJS, **148**, 1(2003)
- [8] L. Wolfenstein Phys. Rev. Lett. **51**, 1945 (1983)
- [9] C. Jarlskog, Phys. Rev. Lett. **55**, 1039 (1985)
- [10] The Super-Kamiokande Collaboration, Phys. Rev. Lett. **86**, 5651(2001)
- [11] The SNO Collaboration, Phys. Rev. Lett. **89**, 011301(2002)
- [12] Particle Data Group (K. Hagiwara *et al.*), Phys. Rev. **D66**, 010001 (2002/2003)

- [13] *BABAR* Collaboration, B. Aubert *et al.*, Phys. Rev. Lett. **88**, 221802 (2002).
- [14] *BABAR* Collaboration, B. Aubert *et al.*, Phys. Rev. Lett. **87**, 201803 (2001).
- [15] *BABAR* Collaboration, B. Aubert *et al.*, Phys. Rev. Lett. **89**, 201802 (2002).
- [16] *BABAR* Collaboration, B. Aubert *et al.*, hep-ex/0408127 (2004).
- [17] *BABAR* Collaboration, B. Aubert *et al.*, Phys. Rev. Lett. **89**, 281802 (2002).
- [18] M. Beneke, G. Buchalla, M. Neubert, C.T. Sachrajda Phys. Rev. Lett. **83**, 1914 (1999).
- [19] H.J. Lipkin, Y. Nir, H.R. Quinn and A.E. Snyder, Phys. Rev. D **44**, 1454 (1991)
- [20] H.R. Quinn and A.E. Snyder, Phys. Rev. D **48**, 2139 (1993)
- [21] Helen R. Quinn and Joao P. Silva, Phys. Rev. D **62**, 054002 (2000)
- [22] CLEO Collaboration (S. Kopp *et al.*) Phys. Rev. D **63**, 092001 (2001)
- [23] ARGUS Collaboration, H. Albrecht *et al.*, Z. Phys. **C48**, 543 (1990).
- [24] J. Blatt and V. Weisskopf, “*Theoretical Nuclear Physics*”, John Wiley & Sons, New York, 1956
- [25] F. von Hippel and C. Quigg, Phys. Rev. **D5**, 624 (1972)
- [26] W.M. Dunwoodie, “*Suggestion for the Parameterization of Dalitz Plot Efficiency*”, http://www.slac.stanford.edu/~wmd/bbkinematics/dalitz_efficiency.note (2002)
- [27] G.J. Gounaris and J.J. Sakurai, Phys. Rev. Lett. **21** 244, (1968)

- [28] A. Deandrea, R. Gatto, M. Ladisa, G. Nardulli, P. Santorelli, Phys. Rev. D **62**, 036001 (2000)
- [29] S. Gardner and U.G. Meissner, Phys. Rev. D **65**, 094004 (2002);
U.G. Meissner, Talk at International Workshop on Heavy Quarks and Leptons,
Vietri sul Mare, Salerno, Italy, May 2002, hep-ph/0206125
- [30] J. Tandean and S. Gardner, Phys. Rev. D **66**, 034019 (2002)
- [31] R. Enomoto and M. Tanabashi, Phys. Lett. B **386**, 413(1996).
- [32] S. Gardner, H.B. O'Connell and A.W. Thomas, Phys. Rev. Lett. **80**, 1834(1998).
- [33] X.H. Gao, O. Leitner and A.W. Thomas, Phys. Rev. D **63**, 056012(2001).
- [34] M. Bauer *et al.*, Z. Phys. C **34**, 103(1987).
- [35] A. Deandrea *et al.*, Phys. Rev. D **62**, 036001(2000).
- [36] S. Gardner *et al.*, Phys. Rev. D **65**, 094004(2002).
- [37] BABAR Collaboration, B. Aubert *et al.*, Phys. Rev. Lett. **91**, 201802 (2003)
- [38] CLEO Collaboration, C.P. Jessop *et al.*, Phys. Rev. Lett. **85**, 2881(2000).
- [39] Belle Collaboration, A. Gordon *et al.*, Phys. Lett. B **542**, 183(2002).
- [40] BABAR Collaboration, B. Aubert *et al.*, Phys. Rev. Lett. **91**, 051801(2003).
- [41] E791 Collaboration, Phys. Rev. Lett. **86**, 770(2001).
- [42] O. Leitner, X. Guo, A. Thomas, Eur. Phys. Jour. C **31** 215(2003).

- [43] ALEPH, DELPHI, L3 and OPAL Collaborations, the LEP working group for Higgs boson searches, CERN-ER/98-046
- [44] L.M. Barkov *et al.* (OLYA, CMD Collaboration), Nucl. Phys. **B256** (1985) 365.
- [45] ALEPH Collaboration, (R. Barate *et al.*), Z. Phys. **C76** 15, (1997)
- [46] J.H. Kühn and A. Santamaria, Z. Phys. **C48** 445, (1990)
- [47] CMD-2 Collaboration, (R.R. Akhmetshin *et al.*), Phys. Lett. **B527** (2002) 161
- [48] DM2 Collaboration, (D. Bisello *et al.*), Phys. Lett. **B220** 321, (1989)
- [49] ALEPH Collaboration, ALEPH 2002-030 CONF 2002-019, (July 2002)
- [50] WA76 Collaboration (T.A. Armstrong *et al.*). Z. Phys. **C51**, 351 (1991)
- [51] E791 Collaboration (E.M. Aitala *et al.*). Phys. Rev. Lett. **86**, 765 (2001)
- [52] E791 Collaboration (E.M. Aitala *et al.*). Phys. Rev. Lett. **86**, 770 (2001)
- [53] The Heavy Flavor Averaging Group (HFAG),
<http://www.slac.stanford.edu/xorg/hfag/>
- [54] A. Gaidot *et al.*, “ $B\bar{B}$ Tagging Studies”, BABAR-Note-461, Oct. 1998
- [55] P. Gay, B. Michel, J. Proriot, and O. Deschamps, “*Tagging Higgs Bosons in Hadronic LEP-2 Events with Neural Networks.*”, In Pisa 1995, New computing techniques in physics research, 725 (1995)